

Modelling the Dynamic Behaviour of Broadband LEDs for Optical Communication

vorgelegt von
Dipl.-Ing.
Manuel Schüppert

an der Fakultät IV - Elektrotechnik und Informatik
der Technischen Universität Berlin
zur Erlangung des akademischen Grades

Doktor der Ingenieurwissenschaften
- Dr.-Ing. -

genehmigte Dissertation

Promotionsausschuss:

Vorsitzender: Prof. Dr.-Ing. Ronald Freund
Gutachter: Prof. Dr.-Ing. Dr. h. c. Klaus Petermann
Gutachter: Prof. Dr.-Ing. Christian-Alexander Bunge
Gutachter: Prof. Dr.-Ing. Sebastian Randel

Tag der wissenschaftlichen Aussprache: 28. März 2022

Berlin 2022

Abstract

Light-emitting diodes (LEDs) are an attractive alternative to lasers for the use as transmitters in optical short-range communications. They are cost-effective and robust against environmental conditions such as varying ambient temperatures. However, in order to be able to maximize the data rate of an LED-based transmission system, detailed knowledge about the signal distortions caused by the electro-optical (E/O) conversion of the LED is required. When spectrally efficient modulation formats, such as multilevel pulse amplitude modulation (M -PAM), are used, nonlinear signal distortions have a particular importance. With the knowledge about these signal distortions, modulation formats or signal equalizers could be optimized for the LED-based communication channel.

In this thesis, a system-theoretic description of the LED is derived, which is based on a well accepted physical device model and which is capable of predicting linear and nonlinear signal distortions occurring in the E/O conversion of the LED. The verification is done using lab measurements of real LEDs. It is shown that second-order nonlinearities are dominant and that these nonlinearities are strongly dependent on the modulation frequency.

As an exemplary application, it is shown that based on the derived mathematical description of the LED, a system inverse may be derived which may be used for signal equalization and is capable of equalizing linear signal distortions as well as frequency dependent second-order nonlinear signal distortions caused by the LED. Accordingly, it is shown that the performance of an LED-based communication system may be significantly improved with such an equalizer, compared to equalization of linear signal distortions only.

Zusammenfassung

Leuchtdioden (LEDs) sind als Sender in der optischen Kurzstreckenkommunikation eine attraktive Alternative zu Lasern. Sie sind preisgünstig und robust gegenüber äußeren Einflüssen, wie zum Beispiel Änderungen der Umgebungstemperatur. Um die Datenrate einer LED-basierten Übertragungsstrecke maximieren zu können, ist jedoch ein genaues Verständnis der durch die elektro-optische (E/O) Wandlung der LED hervorgerufenen Signalverzerrungen vonnöten. Bei der Nutzung von spektral effizienten Modulationsverfahren, wie beispielsweise mehrstufiger Puls-Amplituden-Modulation (M -PAM), kommt hierbei den nichtlinearen Signalverzerrungen eine besondere Bedeutung zu. Mithilfe der Kenntnis dieser Signalverzerrungen können beispielsweise Modulationsverfahren oder Signalentzerrer für die LED-basierte Übertragungsstrecke optimiert werden.

In dieser Arbeit wird basierend auf einem anerkannten physikalischen Modell eine systemtheoretische Beschreibung der LED hergeleitet, welche die Vorhersage von linearen und nichtlinearen Signalverzerrungen der E/O-Wandlung der LED erlaubt. Die Verifikation erfolgt mit Hilfe von Messungen an realen LEDs. Es wird dabei gezeigt, dass Nichtlinearitäten zweiter Ordnung dominieren und dass diese wiederum stark abhängig sind von der Modulationsfrequenz.

Als exemplarische Anwendung dieser LED-Beschreibung wird abschließend gezeigt, dass mithilfe einer darauf basierenden Systeminversen ein an die LED-Übertragung angepasster Signalentzerrer definiert werden kann, welcher imstande ist, lineare Signalverzerrungen und frequenzabhängige nichtlineare Signalverzerrungen zweiter Ordnung zu kompensieren. Entsprechend wird gezeigt, dass damit die Performance der LED-basierten Datenübertragung gegenüber einer alleinigen Kompensation von linearen Signalverzerrungen signifikant verbessert werden kann.

Danksagung

Ich möchte mich an dieser Stelle bei allen Personen bedanken, die mich in der Zeit während diese Arbeit entstanden ist unterstützt haben.

Mein besonderer Dank gilt Herrn Prof. Petermann für die hervorragende Betreuung meiner Arbeit. Mit seinen Kenntnissen und Erfahrungen stand er mir stets zur Seite und konnte immer wieder wichtige Impulse für das erfolgreiche Vorankommen der Arbeit liefern. Weiterhin danke ich Herrn Prof. Bunge sowohl für die vielen wichtigen und spannenden Diskussionen, auf deren Basis diese Arbeit entstanden ist als auch für das Ermöglichen der praktischen Arbeiten im Labor. Außerdem danke ich Prof. Freund und Prof. Randel für Ihre Arbeit im Promotionsausschuss. Zuletzt danke ich natürlich meiner Familie und allen Freunden, die mich während dieser Zeit unterstützt haben.

Contents

1. Introduction	11
1.1. LED-Based Communication	12
1.2. Motivating a Nonlinear LED Device Model	14
1.3. Previous Work on LED Modelling	15
1.4. Outline of the Thesis	17
2. Light-Emitting Diodes: Theoretical Background & Modelling	19
2.1. Light Generation in a Semiconductor Junction	19
2.2. Electrical Properties	26
2.3. Radiative Recombination Rate & Emitted Optical Power	28
2.3.1. Low-level Excitation	29
2.3.2. High-level Excitation	30
2.4. Heterojunctions	31
2.4.1. Double Heterostructure	31
2.4.2. Multi Quantum Well	33
2.5. Nonradiative Carrier Loss Mechanisms	37
2.5.1. Shockley-Reed-Hall Recombination	37
2.5.2. Auger Recombination	38
2.5.3. Carrier Leakage in Heterojunctions	39
2.6. Quantum Efficiency	40
2.6.1. Internal Quantum Efficiency	40
2.6.2. External Quantum Efficiency	40
2.7. A Simplified Model of Communication LEDs	42
3. Verification of the Carrier Density Rate Equation Model	45
3.1. Static P-I	47
3.1.1. Carrier Density Rate Equation Model	47
3.1.2. Measurements	48
3.1.3. Summary	49
3.2. Frequency Response	50
3.2.1. Large-Signal Modulation at a Fixed Input Bias	50
3.2.2. Small-Signal Frequency Response at Varying Bias	57
3.2.3. The Bias-Dependence of the Radiative Recombination Coefficient	60
3.2.4. Summary	63
3.3. Higher-Order Harmonics due to Nonlinearities	64
3.3.1. Large-Signal Modulation	65
3.3.2. Summary	67
3.4. The Frequency Dependence of 2 nd -order Nonlinearities	68
3.4.1. Large-Signal Modulation	71
3.5. Summary	73

4. An Analytic Model of Dynamic Nonlinearities in Directly Modulated LEDs	75
4.1. Volterra-Series Representation of the LED	75
4.2. Frequency Domain Representation of the Nonlinear System	77
4.2.1. First-Order (linear) Part	77
4.2.2. Second-Order Part	78
4.2.3. Some Important Nonlinear Models	80
4.3. The Harmonic Balance Approach	82
4.4. A Harmonic Balance Model of Communication LEDs	83
5. Model Verification	93
5.1. Verification with the Numerical Simulation	94
5.1.1. Small-Signal Modulation	94
5.1.2. Large-Signal Modulation	95
5.2. Verification with Measurements	96
5.2.1. Small-Signal Modulation at varying Bias	97
5.2.2. Large-Signal Modulation	99
5.3. Summary	100
6. Applications in LED-based Communication	103
6.1. A Transmitter Model for Communication Systems	103
6.2. Equalization with an Inverse Volterra Series Approach	107
6.2.1. Exemplary Applications	111
7. Conclusion	117
A. The Potential Impact of Doping	119
A.1. Linear Frequency Response	120
A.2. Nonlinear Frequency Response	123
B. Acronyms	129
C. Bibliography	131

1. Introduction

Optical communication techniques are established in long- and medium-haul transmission systems for decades. Although lasers are the first choice when optical transmit signals of high spectral purity and power are demanded, there are some device-inherent drawbacks in some applications. One important aspect is the temperature-sensitivity of the laser emission; the lasing regime of stimulated emission is only possible above a certain threshold current I_{th} , which is dependent on the temperature T . For example, for double heterostructure (DH) laser diodes it is found that $I_{\text{th}} \propto \exp(T/T_0)$, where $T_0 = 110..160^\circ\text{C}$ [1]. Harsh environmental conditions with strongly varying ambient temperatures may therefore cause the lasing regime to be shifted to higher injection currents and, if cooling techniques are not feasible, the conditions for lasing may no more be fulfilled.

Further, for end-user applications eye-safety aspects play an important role. Eye-safety regulations limit the maximum allowable optical intensity. The coherent nature of the laser emission results in a highly collimated beam. Laser emission therefore exhibits high optical intensities (in units of optical power per area). As a result, eye-safety regulations apply more stringent to lasers than to light sources which exhibit non-collimated radiation patterns.

The emission wavelength of the optical transmitter is another important system design aspect. Apart from technical motivations, such as the use of attenuation minima of optical fibers, the use of visible light transmitters is also often preferred in consumer applications due to their inherently better possibilities for debugging without the use of additional technical equipment. It may be checked by simple inspection with the eye whether a visible light emitting transmitter is working or not. Even though low-cost vertical-cavity surface-emitting lasers (VCSELs) emitting at wavelengths above 800 nm are well established, the fabrication of such devices emitting in the visible light region is not always a trivial task. Especially a proper design of cavity mirrors based on distributed Bragg reflectors (DBRs) working in the visible light region turned out to be a technological challenge [2].

Apart from these technical aspects, cost-effectiveness plays an important role in the design of optical communication systems, especially when it comes to systems targeted for the end-user. Under these boundary conditions, light-emitting diodes (LEDs) constitute an attractive alternative to lasers for the use in next-generation optical short-range transmission systems. LEDs which emit at various wavelengths in the visible light region are commercially available for years and by numerous vendors. Furthermore, the today's extensive use of LEDs in other applications, such as energy efficient lighting or display technology, intensifies the research and development of new types of LEDs. Examples are novel high-speed LED designs (e.g. [3, 4]), or the use of illumination LEDs for communication purposes [5].

1. Introduction

1.1. LED-Based Communication

One example of a commercial system using LEDs is the *media oriented systems transport (MOST)* bus, which is used in automotive applications for years. The MOST bus uses red-emitting LEDs (center wavelength of 650 nm), polymer optical fibers (POFs), and offers data rates of currently up to 150 Mbit/s (“MOST150”) [6].

Another commercial application of LEDs is the so-called Toshiba-link (TOSLINK), which was developed by Toshiba in the early 1980s. TOSLINK also uses red-emitting LEDs and POFs and is used for transmission of digital audio data with bit rates of about 15 Mbit/s.

The development of these systems dates back many years, but research activities in the field of LED-based communication systems have gained increasing interest in the past few years, where two application scenarios for the LED are mostly investigated:

- Fiber-based transmission with a POF
- Indoor wireless optical transmission

A typical system setup for POF-based transmission is depicted in Fig. 1.1a. The light emitted from the LED is coupled into the POF, usually with the help of a small lens, since the standard step-index polymer optical fibers (SI-POFs) have a limited angle of acceptance of about 30° [7].

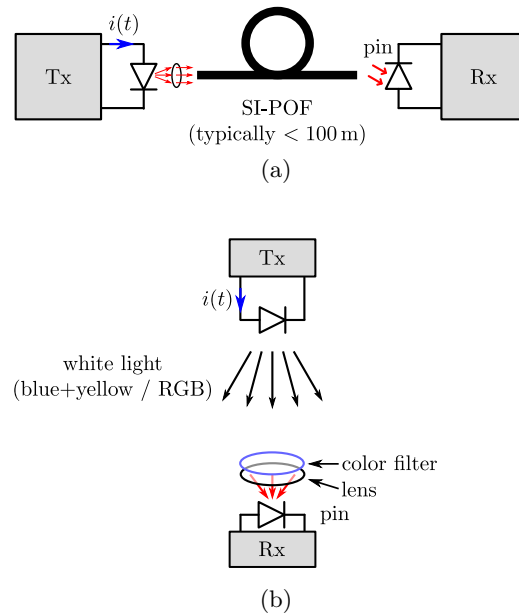


Figure 1.1.: Two application scenarios for LED-based optical transmission: a) Fiber-based with a polymer optical fiber (POF), b) Free-space transmission with an illumination LED.

In case of a SI-POF, the transmission is mainly limited by two factors: Modal dispersion of the fiber, which may be approximated with a bandwidth-length product of the fiber of about $4\text{MHz}\cdot\text{km}$ and fiber attenuation, which has a local minimum of about 140 dB/km at about $\lambda = 650\text{ nm}$ [8]. The receive signal is detected by a low-cost PIN-diode-based photo detector. Transmission lengths are typically below 100 m.

Intensive research was carried out in the past years on such systems, with a special focus on the feasibility of different modulation and equalization schemes to realize data rates beyond 1 GBit/s.

An early demonstration of 1-GBit/s transmission with an LED was presented in [9] where the LED was modulated with discrete multitone (DMT), which is a modulation that uses electrical subcarriers. Subcarrier modulation offers the advantage of being highly adaptive to the channel characteristics, but at the cost of a usually higher system complexity. The signal was transmitted over 50 m of SI-POF and signal processing was performed offline. A real-time transmission of Gigabit Ethernet over an LED-based optical channel was demonstrated in [10]. The transmission medium was 25 m of SI-POF and the signal was modulated with a 4-level pulse amplitude modulation (PAM) in combination with post equalization in the receiver using a feed-forward equalizer (FFE). Another successful approach of Gigabit Ethernet transmission over an LED-based optical channel was presented in [11], where the LED was modulated with simple on-off keying (OOK) and after 50 m of SI-POF the signal was post equalized with a decision feedback equalizer (DFE). The potential of so-called resonant-cavity light-emitting diodes (RC-LEDs), an LED type which employs an optical cavity, was demonstrated in [12], where 5 GBit/s were achieved with multilevel pulse amplitude modulation (*M*-PAM) in combination with a Volterra-series-based post equalization.

The second LED application scenario, wireless optical short-range transmission, is used for decades in the infrared (IR) range of the electromagnetic spectrum for applications like remote controls. But recently, the commercial success of illumination LEDs has brought attention to the idea of using such illumination LEDs simultaneously for illumination and communication purposes. The motivation for this is twofold: On the one hand, this offers the opportunity that a communication channel may be established without the need for additional hardware. Thereby potentially saving energy and costs. On the other hand, the optical range of the electromagnetic spectrum offers the opportunity to establish well-defined small communication cells, since optical frequencies are easily blocked by non-transparent obstacles. In contrast to radio frequency (RF) systems like Wi-Fi, this eases the spatial reuse of carrier frequencies. As a result, the topic has gained a lot attention in the last years and the concept of using white light illumination LEDs for communication is often referred to as visible light communication (VLC).

The topology of a VLC system is shown in Fig. 1.1b. Due to a wide angle of illumination, only a small fraction of the emitted light may be received by the photo detector. Proper choice of a focussing lens at the receiver (Rx) is therefore crucial for maximization of the received signal-to-noise ratio (SNR). White-light LEDs are actually di- or tri-chromatic sources¹. This brings technological challenges, but also additional opportunities, since a separation of the different colors may be achieved with an optical bandpass filter.

A real time implementation of a 100 MBit/s VLC link was presented in [13]. A commercially available LED was modulated with a DMT of 31 subcarriers. Prior to reception with a Si PIN diode, the yellow light produced by the phosphor was filtered

¹Two approaches for the generation of white light are common for LEDs: 1) A blue-emitting LED is covered by a phosphorous layer, which converts part of the emitted blue light into lower-energy yellow light. 2) A three-chip RGB LED is used. In both cases the resulting emission is perceived by the human eye as white light.

1. Introduction

out. In [14], a bitrate of 513 MBit/s was successfully demonstrated with a similar LED and an avalanche photodiode (APD). The feasibility of RGB LEDs for VLC was demonstrated in [15], where up to 806 MBit/s were achieved with DMT and a PIN-diode-based reception. Another approach to maximize data throughput was presented in [16], where all three colors of an RGB LED were modulated simultaneously to build up a wavelength division multiplexing (WDM) transmission. The transmit signals were modulated with multilevel carrierless amplitude and phase modulation (M^2 -CAP) and at the receiver side the signals were filtered with the corresponding color filters prior to reception with a PIN diode. An aggregate bitrate of 3.22 GBit/s was achieved. VLC is also part of current IEEE standardization activities on optical wireless communication (OWC) [17].

1.2. Motivating a Nonlinear LED Device Model

To optimize the design of a communication system, detailed knowledge of the underlying physical channel is required. An important design parameter of the system is the so-called spectral efficiency (SE) of the modulation format, which defines the data rate per occupied bandwidth, that is, in terms of transmitted bits per second per Hertz. An example of a modulation format with a low spectral efficiency is OOK, which uses two different amplitude levels for the transmission of information. In contrast, 8-PAM uses eight amplitude levels for data transmission, and as a result, the SE of 8-PAM is increased by a factor of $\log_2(8) = 3$ compared to OOK.

Modulation formats with a high spectral efficiency are the preferred choice for next-generation optical short-range transmission systems, since they reduce the bandwidth requirements for both electrical and optical components. However, due to the increased number of amplitude levels which must be correctly demodulated at the receiver side, the reduced bandwidth requirement offered by an increased spectral efficiency is paid by an increased susceptibility of the signal to nonlinear distortions.

In principle, all parts of a communication system (transmitter, transmission medium, receiver) may introduce nonlinear signal distortions. Nonlinear effects in optical fibers are introduced at high optical intensities (in terms of optical power per cross-sectional area). LEDs, however, emit with a wide opening angle (compared to the collimated nature of laser diode emission) and are typically used with large-core POFs. Therefore, fiber nonlinearities do hardly occur in a normal LED transmission scenario [7]. Nonlinearities of the receiver are usually negligible due to the low power level of the received signal.

As a result, the LED is the dominant source of nonlinear signal distortions, and deriving a nonlinear channel model, which is applicable to communication system characterizations is basically equivalent to finding a nonlinear model of the LED.

1.3. Previous Work on LED Modelling

Nonlinear signal distortions occurring in the electro-optical (E/O) conversion of LEDs are the subject of research activities for decades.

An early approach for a simple model of LED nonlinearities was given by Lee in [18]. The work was motivated by the previous observation that high-efficiency devices which employ a DH suffer from stronger harmonic distortions than the lower-efficiency counterparts based on a homojunction. In that publication, the impact of surface recombination under the assumption of a bias-dependent radiative carrier lifetime was modelled in terms of higher-order harmonics for a low-frequency LED current injection. The theory basically predicted a decreasing distortion with increasing bias current, and discrepancies to measurements were attributed to the potential impact of thermal heating at higher bias values. The derivation of 2nd-order harmonics was based on a Taylor series expansion, and hence, the impact of the modulation frequency was not considered. That is, only static nonlinearities were considered.

An early investigation of LED nonlinearities from a communication point of view was presented by Dawson in [19]. Therein, 2nd-order and 3rd-order harmonic distortions were measured for homojunction and DH devices for varying bias and modulation frequency and several interesting characteristics were found. The results confirmed that the DH device tends to suffer stronger distortions than the homojunction device. Another important result was that 3rd-order harmonic distortions were well (≈ 10 dB) below 2nd-order distortions. It was further observed for the DH device that, for a fixed modulation amplitude, nonlinear distortions decrease with increasing electrical bias. Finally, it was observed that the modulation frequency has a strong impact on the nonlinear distortion. For the investigated frequencies between 0.5 MHz and 6 MHz, the harmonic distortion levels differed by up to about 20 dB. The results revealed a complex nature of the frequency-dependent LED nonlinearities, but a mathematical description of the physical origins was not presented in [19].

In the past, some attempts to model the device were based on equivalent circuit models. For example, Tucker presented in 1981 an equivalent circuit model of a DH laser below threshold [20]. However, the scope of this model was to predict turn-on delays of directly modulated lasers, which were well below 10 ns. That is, such a model is not feasible for state-of-the-art communication LEDs, which offer modulation bandwidth of usually well below 100 MHz. Nonlinearities occurring for a harmonic excitation under forward bias were not addressed.

With a similar approach, a large-signal model of LEDs was published in 1981 by Descombes and Guggenbühl [21]. The model is based on bulk recombination in a single heterostructure (SH) or DH device, which is governed by drift and diffusion processes and hence spatially varying carrier densities. An adaptation to modern quantum well (QW) devices is therefore not possible in a direct manner. The model requires numerical simulation and the knowledge of numerous device parameters. Switching transients of an OOK signal were investigated, which does not allow for a generalized system-theoretic derivation of LED nonlinearities, and hence, cannot be applied to other modulation formats like *M*-PAM.

The state of knowledge concerning the modulation behaviour of LEDs was summarized in a more recent publication by Kamalakis et al. in [22]. Motivated by the potential use of advanced modulation formats in next-generation LED communication

1. Introduction

systems, detailed measurements of switching transients as well as small-signal frequency responses of a commercial IR LED were conducted. A comparison of the measurement results with existing models revealed strong discrepancies, even for the small-signal investigations, and the authors concluded that an accurate description of the LED's transfer characteristics must incorporate linear and non-linear properties of the device.

Motivated by these results, the same authors conducted detailed measurements of various commercially available LEDs in [23]. Therein, it was assumed that the LED may be represented by Volterra series, consisting of a linear part and a 2nd-order non-linear part. It was found that the E/O conversion of the LEDs introduces nonlinear distortions which are strongly dependent on the modulation frequency. The nature of this frequency dependence was complicated and a theoretical model which describes the observed behaviour was not given. Furthermore, the device behaviour in terms of the static P-versus-I curve, the linear frequency response and the nonlinear part of the frequency response differed between the investigated LED models. The authors emphasized that an accurate device model, which predicts such a behaviour is of great importance for the application of signal equalization, yet still lacking.

The lack of this knowledge has led to the application of various kinds of nonlinear LED models and it is not clear which of those accurately describe the LED behaviour, if any. A common simplified approach is to model the LED's static P-versus-I curve in terms of a polynomial. The coefficients of the polynomial may be estimated using a parameter fit of the measured static P-I, e.g. [24–26]. The attractiveness of this approach lies in its simplicity, but the results of [23] indicate that this is far from a realistic LED model.

With the aim of getting closer to a realistic nonlinear LED model, the above approach of the static nonlinear origin may be extended in various ways. A model may be built up of a static nonlinear process followed by a linear time-invariant (LTI) system block, which is also referred to as a Hammerstein model [27]. Another approach is a nonlinear model built up of an LTI block followed by a static nonlinear process, which is referred to as a Wiener model [28]. A further extension is the concatenation of the two models, building up a Wiener-Hammerstein model [29]. However, the measurement results obtained in [23] indicated that the LED is usually not accurately described by such simplified models. These models must therefore be seen as a compromise between model complexity and accuracy. More recently, a simplified carrier density rate equation model was used to derive a signal predistorter structure for applications in VLC [30].

The author of this thesis showed in [31, 32] with blind equalization techniques that powerful nonlinear channel models can drastically increase the bitrate of LED-based communication channels. And it is still an open question whether similar performances may be achieved with less complex nonlinear models or whether the system performance may even be increased by the use of “LED-optimized” nonlinear equalizers. These problems may only be properly addressed with the derivation of an accurate model of the nonlinear modulation characteristics of the LED.

This thesis aims to contribute to solve this problem by presenting a simplified nonlinear device model of commercial communication LEDs which emit in the visible light spectrum. This model shall only be dependent on device parameters which are either found in the literature or are easily extracted with lab measurements. The mathematical description shall be given in a well-known system-theoretic formulation to allow efficient computer-based system simulations.

1.4. Outline of the Thesis

The outline of the thesis is as follows. Chapter 2 gives an overview of the fundamentals of the LED technology with its most important electrical and optical characteristics when used as a directly modulated optical transmitter. Based on these discussions, a simplified device model is introduced at the end of Chapter 2, which aims to model the linear and nonlinear characteristics of the communication LED's E/O conversion with only a few device parameters.

This simplified physical model is then thoroughly verified in Chapter 3 with measurements of commercially available communication LEDs. Based on the successful verification of this model, a mathematical derivation is presented in Chapter 4 which describes the linear and nonlinear part of the E/O conversion in a fully analytic fashion. The accuracy of this closed-form mathematical expression for the LED's E/O conversion is then verified against both numerical simulations of the underlying physical model as well as lab measurements of the commercial devices.

The LED device model derived in this work is a powerful tool which may be used in the performance evaluation and optimization of LED-based communication systems. Potential applications are demonstrated in Chapter 6, where it is shown that a powerful equalizer structure may be derived from the analytic device model which also allows for a reduced-complexity implementation without performance degradation. The thesis is concluded in Chapter 7.

2. Light-Emitting Diodes: Theoretical Background & Modelling

2.1. Light Generation in a Semiconductor Junction

Light generation in LEDs is based on spontaneous emission, an interaction between carriers in a semiconductor and photons. Spontaneous emission describes the effect when an electron, which was brought into a higher energy state (=excited state) recombines with a hole into a state of lower energy by emission of a photon. This effect occurs without a stimulus, that is, it occurs spontaneously. When the energy level in the excited state is denoted E_1 and the energy level at the lower state is denoted E_0 , the energy of the emitted photon is

$$E_{\text{ph}} = E_1 - E_0 = h \cdot \nu, \quad (2.1)$$

where $h \approx 4.136 \cdot 10^{-15}$ eVs is the Planck constant and ν is the frequency of the emitted photon. That is, the energy difference $\Delta E = E_1 - E_0$ determines the optical emission frequency ν , as illustrated in Fig. 2.1. Energy levels are typically measured in units of electronvolt (eV), where $1 \text{ eV} = 1.6 \cdot 10^{-19}$ Joule.

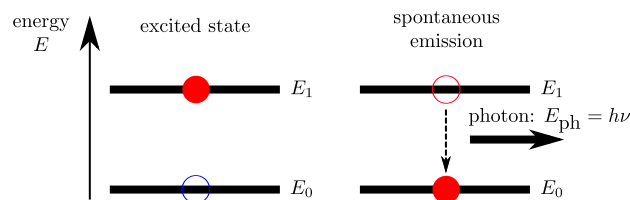


Figure 2.1.: Principle of spontaneous radiative emission.

In the following, the energy band diagram of a semiconductor material, as depicted in Fig. 2.2 (left) is considered. The semiconductor is characterized by a specific energy band gap E_g between the so-called valence band and the conduction band. The valence band is defined as the energy band which is fully populated with electrons at absolute zero ($T = 0 \text{ K}$). The conduction band represents the range of allowed energy states above the valence band. The energies of the conduction and valence band edge are denoted E_C and E_V , respectively.

In thermal equilibrium at a temperature T , the probability that a given energy state E is occupied by an electron is given by the Fermi-Dirac distribution [33]

$$f_e(E) = \frac{1}{1 + \exp\left(\frac{E - E_F}{kT}\right)}, \quad (2.2)$$

where $k = 8.617 \cdot 10^{-5}$ eV/K is the Boltzmann constant and E_F is the so-called Fermi

2. Light-Emitting Diodes: Theoretical Background & Modelling

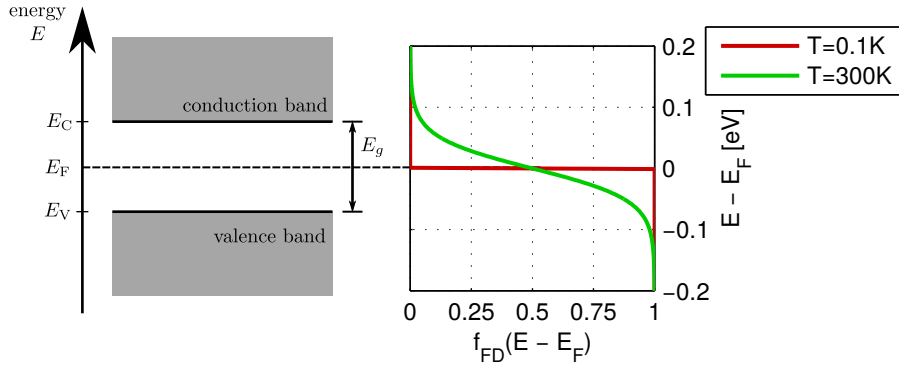


Figure 2.2.: Energy bands of an intrinsic semiconductor (left) and Fermi-Dirac distribution of electrons at different Temperatures (right).

level at which $f_e(E_F) = 0.5$. The probability distribution of holes is then given by [33]

$$f_h(E) = 1 - f_e(E). \quad (2.3)$$

At a finite temperature T , $f_e(E)$ changes continuously from 1 to 0 with increasing E . The Fermi-Dirac distribution of electrons is exemplarily sketched in Fig. 2.2 (right) for two different temperatures. For an intrinsic semiconductor the Fermi level lies very close to the middle of the band gap [1]. Table 2.1 exemplarily lists the bandgap energies of some semiconductors.

Table 2.1.: Bandgap energies of some commonly used semiconductors.

Material	Bandgap in eV
GaAs	1.42
InP	1.35
GaN	3.4

The carrier density distributions in the semiconductor versus energy E are obtained by applying some commonly used simplifications. The electron density in the conduction band versus energy E is given by the Fermi-Dirac distribution of Eq. (2.2) and the electron density of states (DOS) $\rho_e(E)$ according to [33]

$$n_E(E) = \rho_e(E) f_e(E). \quad (2.4)$$

Where the subscript E shall indicate a density in terms of electrons per unit volume and energy. The DOS is defined as the number of states per energy and per unit volume. Likewise, the hole density (per unit volume and energy) in the valence band versus energy E is given with the DOS of the holes $\rho_h(E)$ as

$$p_E(E) = \rho_h(E) f_h(E). \quad (2.5)$$

The carrier densities in terms of carriers per unit volume in the semiconductor's energy

2.1. Light Generation in a Semiconductor Junction

bands are then

$$n = \int_{E_C}^{\infty} n_E(E) dE, \quad (2.6)$$

$$p = \int_{-\infty}^{E_V} p_E(E) dE. \quad (2.7)$$

When an electron and a hole recombine radiatively by emission of a photon, conservation of momentum applies [1]. Since the momentum of a photon is orders of magnitude smaller than those of electrons and holes, radiative recombination is assumed to involve only electrons and holes of the same momentum $p_{\text{carrier}} = \hbar \cdot k$ [1, 34]. This is referred to as the k -selection rule.

Information on the momentum p_{carrier} of the carriers in the semiconductor lattice is obtained from the carrier's $E - k$ relationship. The $E - k$ relationship (also referred to as the dispersion relation) may be derived from the Schrödinger equation. The resulting $E - k$ relationships in the conduction and valence band of the semiconductor are generally of complicated nature. Near the band edges ($E \approx E_C, E_V$), however, a parabolic approximation is commonly assumed [1]. For the electrons in the conduction band, this results in

$$E(k) = \frac{\hbar^2 k^2}{2m_e^*} + E_C, \quad (2.8)$$

with the effective mass of electrons m_e^* and the reduced Planck constant $\hbar = h/2\pi$. The dispersion relation of holes in the valence band is obtained in a similar manner. Such parabolic dispersion relations are sketched in Fig. 2.3 for a direct bandgap semiconductor, which exhibits the extrema at the same k value. The k -selection rule forces “vertical” recombination, as sketched in Fig. 2.3.

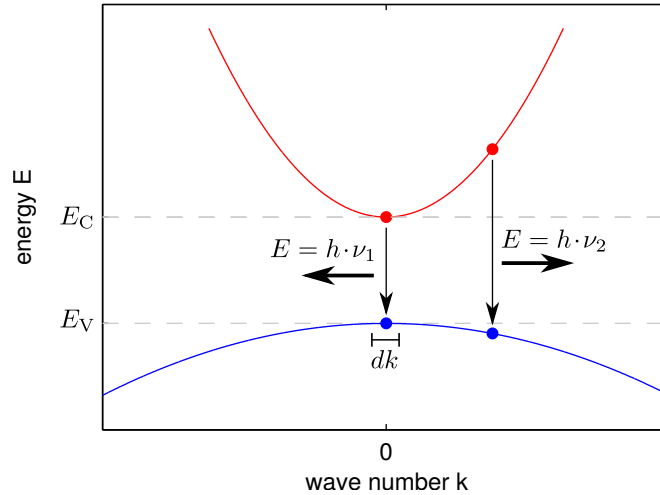


Figure 2.3.: Vertical recombination due to the k -selection rule in a direct bandgap semiconductor with parabolic dispersion relation.

2. Light-Emitting Diodes: Theoretical Background & Modelling

Under the assumption of a parabolic dispersion relation the densities of states $\rho_e(E)$ and $\rho_h(E)$ of electrons and holes in the bulk semiconductor are given as [33, 35]

$$\rho_e(E) = \frac{1}{2\pi^2} \left(\frac{2m_e^*}{\hbar^2} \right)^{\frac{3}{2}} \cdot \sqrt{E - E_C}, \quad \text{for } E > E_C \quad (2.9)$$

$$\rho_h(E) = \frac{1}{2\pi^2} \left(\frac{2m_h^*}{\hbar^2} \right)^{\frac{3}{2}} \cdot \sqrt{E_V - E}, \quad \text{for } E < E_V, \quad (2.10)$$

with the effective masses of electrons and holes m_e^*, m_h^* , the bottom of the conduction band E_C , and the top of the valence band E_V (cf. Fig. 2.2).

The resulting carrier density distributions versus energy E of electrons and holes in the intrinsic semiconductor in thermal equilibrium are then given with Eqs. (2.2) to (2.5) and Eqs. (2.9) and (2.10) as

$$n_E(E) \propto \sqrt{E - E_C} \cdot \frac{1}{1 + \exp\left(\frac{E - E_F}{kT}\right)}, \quad \text{for } E > E_C \quad (2.11)$$

$$p_E(E) \propto \sqrt{E_V - E} \cdot \left(1 - \frac{1}{1 + \exp\left(\frac{E - E_F}{kT}\right)} \right), \quad \text{for } E < E_V, \quad (2.12)$$

These carrier density distributions are sketched in Fig. 2.4 (left).

Equations (2.11) and (2.12) constitute distributions commonly found in the literature. The simplified LED device model which will be presented in this thesis, however, will be independent of the specific shape of $n_E(E)$ and $p_E(E)$; the model will rather make use of the integral carrier densities of Eqs. (2.6) and (2.7). But the distributions $n_E(E)$ and $p_E(E)$ are used to motivate some boundary conditions for the device model.

In an intrinsic semiconductor at a finite temperature, thermal excitation of electrons from the valence band into the conduction band occurs, which leaves an equal number of holes in the valence band. This process is counteracted by recombination of electrons back into the valence band. As a result, steady state net carrier densities of

$$n_0 = p_0 := n_i \quad (2.13)$$

are established, where n_i is referred to as the intrinsic carrier density [1].

The carrier densities in the energy bands of a semiconductor may be altered by the introduction of impurities into the semiconductor lattice, which is referred to as doping. The semiconductor can be either doped with donor atoms, resulting in an n -type semiconductor, or with acceptor atoms, which results in a p -type semiconductor. A donor atom is an element which has more valence electrons than the semiconductor material. As a result, the excess valence electrons are only weakly bounded, and hence a reduced energy is needed for them to be brought into the conduction band. Therefore, n -doping effectively shifts the Fermi level E_F towards E_C . The concentration of donors per unit volume is denoted N_D . The p -doping introduces acceptor atoms with a number of valence electrons less than the semiconductor. As a result, weakly bounded holes are introduced and E_F is shifted towards E_V . The concentration of acceptors per unit volume is denoted N_A .

2.1. Light Generation in a Semiconductor Junction

According to Eqs. (2.2) to (2.5), the shifted Fermi level in a doped semiconductor alters the carrier density distributions. The resulting carrier density distributions of a p -type and n -type semiconductor in thermal equilibrium are sketched in Fig. 2.4 (middle) and (right), along with their Fermi levels. In the presence of impurities the mass action law still applies, i.e. $np = n_i^2$ still holds.

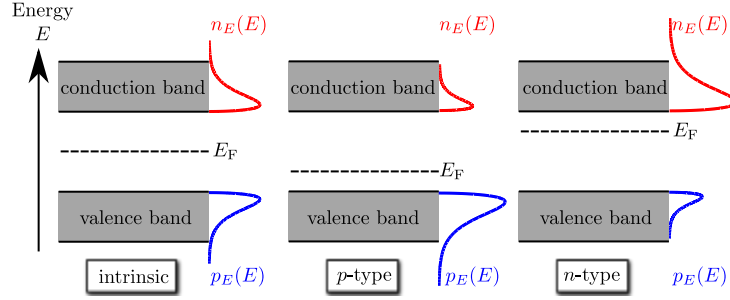


Figure 2.4.: Carrier distributions and Fermi levels in an undoped and doped semiconductor.

For doping scenarios where the respective Fermi levels stay within the bandgap (“non-degenerate semiconductors”), the approximation $E - E_F \gg kT$ may be applied. The Fermi-Dirac distribution of Eq. (2.2) may then be reduced to a *Boltzmann distribution* of the form

$$f_{e,\text{Boltzmann}}(E) \propto \exp\left(-\frac{E}{kT}\right). \quad (2.14)$$

The carrier densities p and n which result from the doping processes are dependent on E_F as well as the thermal energy kT . However, for mathematical derivations of the device behaviour, ionization of all dopants is usually assumed which leads to $n = N_D$ and $p = N_A$, respectively.

Based on such distinct carrier distributions in the energy bands, semiconductor junctions may be built, which constitute the basis for the light generation in LEDs.

When a p -type and an n -type semiconductor are joined to form a pn junction, the Fermi level under thermal equilibrium of this composite system must stay constant throughout the entire system, i.e. $E_F(p\text{-type}) = E_F(n\text{-type})$ [36]. Electrons will diffuse from the n -doped region to the p -doped region and holes will diffuse from the p -doped region to the n -doped region. These carriers recombine at the junction to form the so-called depletion region.

The diffusion process leaves ionized donors in the n -type and ionized acceptors in the p -type. These charges build up an electric potential of

$$U_D = \frac{kT}{q} \cdot \ln\left(\frac{N_A N_D}{n_i^2}\right), \quad (2.15)$$

with the elementary charge $q \approx 1.6 \cdot 10^{-19} C$ and intrinsic carrier density n_i . U_D is also referred to as the diffusion voltage. The diffusion voltage establishes an electric field, which, in turn, induces a drift current in opposite direction of the diffusion current. In thermal equilibrium, both currents cancel each other.

2. Light-Emitting Diodes: Theoretical Background & Modelling

In the band diagram of the pn junction, the electrical potential U_D translates to an energy offset of $\Delta E = q \cdot U_D$ between the energy bands of the p -type and n -type. As a result, the band-edges in the pn junction realign, as sketched in Fig. 2.5. The energy difference ΔE acts as a barrier which prevents further diffusion of electrons into the p -type region and of holes into the n -type region.

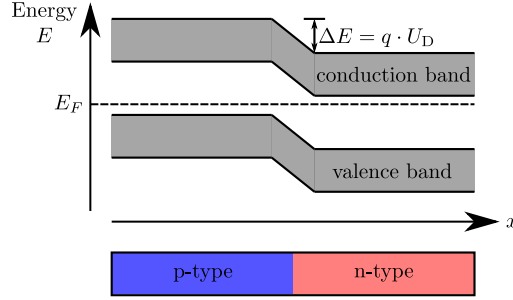


Figure 2.5.: Simplified energy band structure of an unbiased pn junction.

The carrier densities in the semiconductor junction may be controlled with the application of an external bias.

Under forward bias, electrons are injected into the n -type region and holes into the p -type. With this carrier injection, so-called *quasi Fermi levels* $E_{F,n}$ and $E_{F,p}$ for electrons and holes are introduced, where under forward bias $(E_{F,n} - E_{F,p}) > 0$. As a result, the potential barrier is lowered to $\Delta E(U_{\text{bias}}) = q \cdot (U_D - U_{\text{bias}})$, as sketched in Fig. 2.6 (left). This reduces the drift current, which counteracts the carrier diffusion. Diffusion of electrons into the p -type and of holes into the n -type is enabled.

The spatial distribution of these so-called minority carriers (electrons in the p -type and holes in the n -type) is governed by their diffusion constants, and hence the carrier mobilities. Assuming a common diffusion scenario with a fixed injection source at position $x = 0$, the carrier density concentrations $n(x)$ and $p(x)$ decay exponentially with x [1]. The spatial distributions of electrons in the p -type and holes in the n -type may then be described with their diffusion lengths L_n and L_p , respectively, which describe the mean distances the minority carriers diffuse before they recombine. In typical semiconductors, the diffusion length is in the order of several micrometers, e.g. $L_n \approx 15 \mu\text{m}$ in p -type gallium-arsenide (GaAs) [34].

The region near the pn junction exhibits the highest densities of both electrons and holes which may recombine radiatively. This region is referred to as the active region.

The generation of carriers inside the active region of volume V_{active} is determined by the electric current I and may be formulated in form of a carrier density generation rate G (in terms of carriers per unit volume and unit time) of

$$G = \frac{I}{q \cdot V_{\text{active}}}. \quad (2.16)$$

When a reverse bias is applied to the pn junction, as depicted in Fig. 2.6 (right), $(E_{F,n} - E_{F,p}) < 0$ holds and the energy barrier increases to $\Delta E(U_{\text{bias}}) = q \cdot (U_D + U_{\text{bias}})$. The increased potential reduces the diffusion of holes into the n -type and that of electrons into the p -type. As a result, a current flow through the active region and hence also radiative recombination are virtually suppressed.

2.1. Light Generation in a Semiconductor Junction

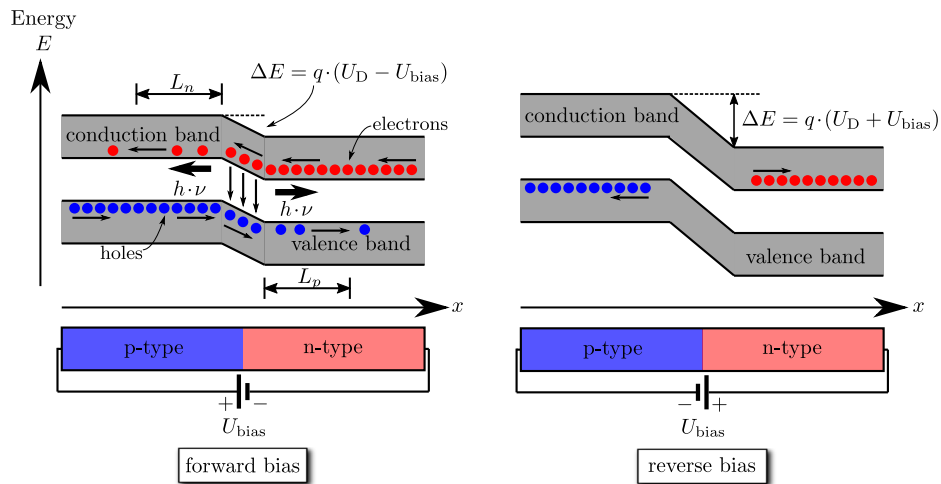


Figure 2.6.: Energy band structures of a biased pn junction.

Light generation in the LED therefore requires a strictly positive electric input current. To maximize the received SNR in a communication system, large-signal modulation is desired, with a modulation index $m \approx 1$, where (cf. Fig. 2.7)

$$m := \frac{I_0 - i_{\min}}{I_0}. \quad (2.17)$$

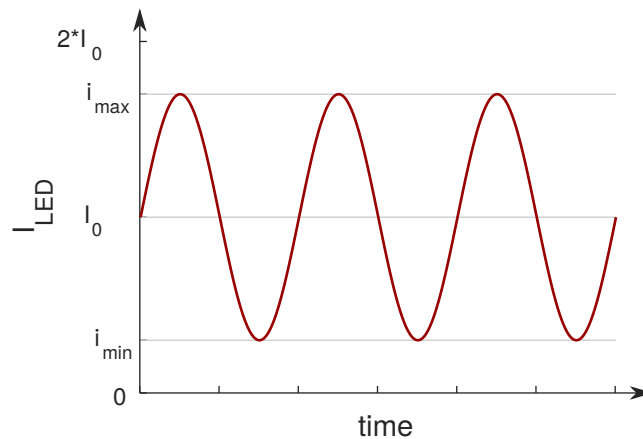


Figure 2.7.: On the definition of the modulation index m for the biased input current.

2.2. Electrical Properties

The current-voltage characteristics of the LED are usually derived for an abrupt pn junction under the simplifying assumptions of [37]

1. Low-level injection; that is, the injected minority carrier density is small compared to the majority carrier density
2. Boltzmann distribution of the carriers
3. Current flow in the quasi-neutral regions is purely due to diffusion
4. The quasi-neutral regions are infinitely long
5. No generation/recombination phenomena in the space-charge region

For the above assumptions, the electron and hole current densities versus x (cf. Fig. 2.5) may be calculated by considering the diffusion currents of the minority carriers in the quasi-neutral regions [37], that is, the electrons which diffuse into the p -type and the holes which diffuse into the n -type.

The resulting current I through the pn junction versus applied bias voltage U is then described by the well-known Shockley equation [34]

$$I(U) = I_S \left[\exp\left(\frac{qU}{kT}\right) - 1 \right]. \quad (2.18)$$

Under reverse bias ($U < 0$), the current saturates at

$$I_S = qA \left[\frac{D_p}{L_p} \cdot \frac{n_i^2}{N_D} + \frac{D_n}{L_n} \cdot \frac{n_i^2}{N_A} \right], \quad (2.19)$$

with the cross sectional area A of the pn junction, concentration of donors N_D and acceptors N_A , intrinsic carrier density n_i , diffusion constants of electrons and holes D_n, D_p , and diffusion lengths L_n, L_p .

To find an approximation for scenarios where the above simplifying assumptions are not (fully) satisfied, a modified Shockley equation of

$$I(U) = I_S \left[\exp\left(\frac{qU}{n_{\text{ideal}} \cdot kT}\right) - 1 \right] \quad (2.20)$$

is often used, where an ideality factor n_{ideal} is introduced. Typical values are $1.1 \leq n_{\text{ideal}} \leq 1.5$; however, values of up to $n_{\text{ideal}} = 7$ were found for some semiconductors [34].

The current-voltage characteristic of the pn junction under forward bias is derived by incorporating the definition of the diffusion voltage U_D . Equation (2.15) may be re-written as

$$\exp\left(\frac{qU_D}{kT}\right) = \frac{N_A N_D}{n_i^2}. \quad (2.21)$$

Putting Eq. (2.21) into (2.18) gives

$$\begin{aligned}
 I(U) &= qA \left[\frac{D_p}{L_p} \cdot \frac{n_i^2}{N_D} + \frac{D_n}{L_n} \cdot \frac{n_i^2}{N_A} \right] \cdot \left[\exp\left(\frac{qU}{kT}\right) - 1 \right] \\
 &= qA \frac{n_i^2}{N_A N_D} \left[\frac{D_p}{L_p} N_A + \frac{D_n}{L_n} N_D \right] \cdot \left[\exp\left(\frac{qU}{kT}\right) - 1 \right] \\
 &= qA \cdot \exp\left(-\frac{qU_D}{kT}\right) \cdot \left[\frac{D_p}{L_p} N_A + \frac{D_n}{L_n} N_D \right] \cdot \left[\exp\left(\frac{qU}{kT}\right) - 1 \right],
 \end{aligned}$$

and for $U \gg kT/q$

$$I(U > 0) = qA \left[\frac{D_p}{L_p} N_A + \frac{D_n}{L_n} N_D \right] \cdot \exp\left(\frac{q(U - U_D)}{kT}\right). \quad (2.22)$$

Equation (2.22) exhibits a threshold voltage of $U_{\text{th}} \approx U_D$ beyond which the current strongly increases with applied voltage U .

An exact calculation of the device current $I(U)$ given by Eq. (2.22) requires the knowledge of both the semiconductor's parameters D_p, D_n , as well as the knowledge of N_A, N_D, L_p , and L_n , which are defined by the fabrication process. Exemplary plots of the normalized current-voltage characteristic are shown in Fig. 2.8 for $E_{g,\text{Si}} = 1.12 \text{ eV}$ and $E_{g,\text{GaAs}} = 1.42 \text{ eV}$. It is observed that the device current increases strongly beyond U_{th} . A differential resistance of

$$r = \frac{dU}{dI} \quad (2.23)$$

may be defined for the LED. Assuming, for the sake of simplicity, a linear slope for the region beyond U_{th} , one may extract typical values of about $r < 0.5 \Omega$ [34].

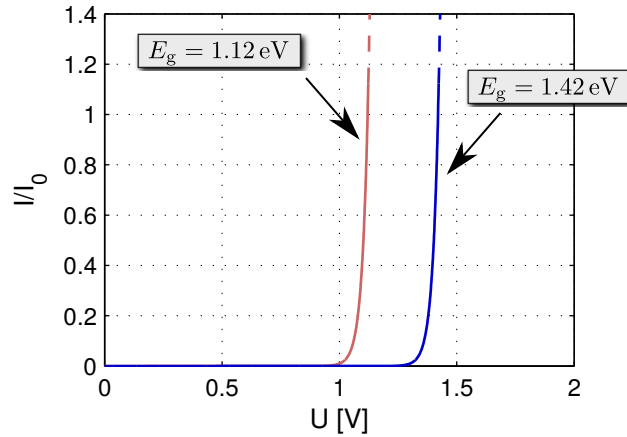


Figure 2.8.: Normalized current-voltage characteristic of a pn junction with different semiconductor bandgaps.

2.3. Radiative Recombination Rate & Emitted Optical Power

The carrier dynamics due to spontaneous emission, which define the transient characteristics of the LED's E/O conversion, are usually described on a phenomenological basis [36]. The generation of a photon by spontaneous emission requires both an electron and a hole to be available. The number of emitted photons per unit volume is therefore proportional to both the electron density n in the conduction band and to the hole density p in the valence band.

As a result, a radiative recombination rate (in terms of emitted photons per unit volume and unit time) may be described as [1, 34].

$$R_{\text{rad}} = B \cdot p \cdot n, \quad (2.24)$$

where the proportionality constant B is called the bimolecular recombination coefficient. Typical values for B of some direct bandgap semiconductors are summarized in Table.2.2.

Table 2.2.: Bandgap and bimolecular recombination coefficient B at $T = 300$ K of some semiconductors.

Material	Bandgap in eV	B in cm^3/s
GaAs	1.42	$2.0 \cdot 10^{-10}$
InP	1.35	$1.2 \cdot 10^{-10}$
GaN	3.4	$2.2 \cdot 10^{-10}$

The optical power generated per unit volume is given by the radiative recombination rate R_{rad} and the photon energy E_{ph} of Eq. (2.1) as

$$\frac{dP}{dV} = E_{\text{ph}} \cdot R_{\text{rad}} = h\nu \cdot R_{\text{rad}}. \quad (2.25)$$

Under the assumption of a uniform recombination rate across the entire active volume V_{active} , the optical power which is emitted from the active region is given as

$$P_{\text{int}} = V_{\text{active}} \cdot \frac{dP}{dV} = V_{\text{active}} \cdot E_{\text{ph}} \cdot R_{\text{rad}}. \quad (2.26)$$

The carrier densities n and p in Eq. (2.24) are assumed to be the sum of thermally generated equilibrium carrier densities n_0, p_0 and excess carrier densities $\Delta n, \Delta p$, i.e.

$$n = n_0 + \Delta n \quad (2.27)$$

$$p = p_0 + \Delta p. \quad (2.28)$$

In principle, the excess carrier densities may be generated by either absorption of light or by an injection current. The radiative recombination rate may then be re-written as

2.3. Radiative Recombination Rate & Emitted Optical Power

$$\begin{aligned} R_{\text{rad}} &= B \cdot [n_0 + \Delta n] \cdot [p_0 + \Delta p] \\ &= B \cdot [n_0 p_0 + n_0 \Delta p + \Delta n p_0 + \Delta p \Delta n], \end{aligned} \quad (2.29)$$

and with $\Delta n = \Delta p$

$$R_{\text{rad}} = B \cdot [n_0 p_0 + \Delta n(n_0 + p_0 + \Delta n)]. \quad (2.30)$$

Depending on the ratio between equilibrium carrier densities and the excess carrier densities, two excitation regimes may be defined.

2.3.1. Low-level Excitation

The regime of low-level excitation is defined for $\Delta n \ll (p_0 + n_0)$. Equation (2.30) then reduces to

$$\begin{aligned} R_{\text{rad}} &= B \cdot [n_0 p_0 + \Delta n(n_0 + p_0)] \\ &= R_0 + R_{\text{excess}}. \end{aligned} \quad (2.31)$$

That is, the radiative recombination rate is the sum of an equilibrium recombination rate $R_0 = B n_0 p_0$ and an excess recombination rate $R_{\text{excess}} = B \Delta n(n_0 + p_0)$. Likewise, a total generation rate may be defined for the active volume as

$$G_{\text{total}} = G_0 + G, \quad (2.32)$$

with an equilibrium generation rate G_0 and an excess generation rate G . For carrier injection by an electric current, G is given by Eq. (2.16) on page 24. The time-dependent carrier density in the active volume in the presence of both carrier generation and recombination is then described by the differential equation

$$\begin{aligned} \frac{dn}{dt} &= G_{\text{total}} - R_{\text{rad}} \\ &= (G_0 + G) - (R_0 + R_{\text{excess}}), \end{aligned} \quad (2.33)$$

and further with $G_0 = R_0$ (obtained from the conditions under thermal equilibrium [1])

$$\frac{d\Delta n}{dt} = G - B(n_0 + p_0)\Delta n. \quad (2.34)$$

Equation (2.34) is the carrier density rate equation for low-level excitation.

When the generation rate G is turned off at a specific moment ($t = 0$), one obtains

$$\frac{d\Delta n}{dt} = -B(n_0 + p_0)\Delta n. \quad (2.35)$$

From Eq. (2.35), a turnoff transient may be derived as [34]

$$\Delta n(t) = \Delta n_0 \cdot \exp[-B(n_0 + p_0) \cdot t], \quad (2.36)$$

with the initial carrier density $\Delta n_0 := \Delta n(t = 0)$.

2.3.2. High-level Excitation

The regime of high-level excitation is defined for $\Delta n \gg (p_0 + n_0)$. This situation is present for devices with an undoped or lightly doped active region. In that case, the equilibrium carrier densities n_0 and p_0 are negligible and Eq. (2.30) reduces to

$$\begin{aligned} R_{\text{rad}} &= B \cdot [n_0 p_0 + (\Delta n)^2] \\ &= B \cdot (\Delta n)^2. \end{aligned} \quad (2.37)$$

This results in a carrier density rate equation of

$$\frac{d\Delta n}{dt} = G - B(\Delta n)^2. \quad (2.38)$$

The turnoff transient of Eq. (2.38) may be derived as [34]

$$\Delta n(t) = \frac{1}{Bt + \frac{1}{\Delta n_0}}, \quad (2.39)$$

again with $\Delta n_0 := \Delta n(t = 0)$ being the carrier density at the instant when the carrier generation is turned off. This is sketched in Fig. 2.9, along with the low-level turnoff transient of Eq. (2.36). Comparing the luminescence decays of the two excitation regimes reveals a much steeper slope in the case of high-level excitation. This indicates that LEDs offer much broader frequency responses of the E/O conversion when driven in the high-level excitation regime. However, for the turnoff transients, at some point the level drops into the regime of low-level carrier densities, from which on the low-level approximation must be applied; this is indicated by the dashed continuation in Fig. 2.9.

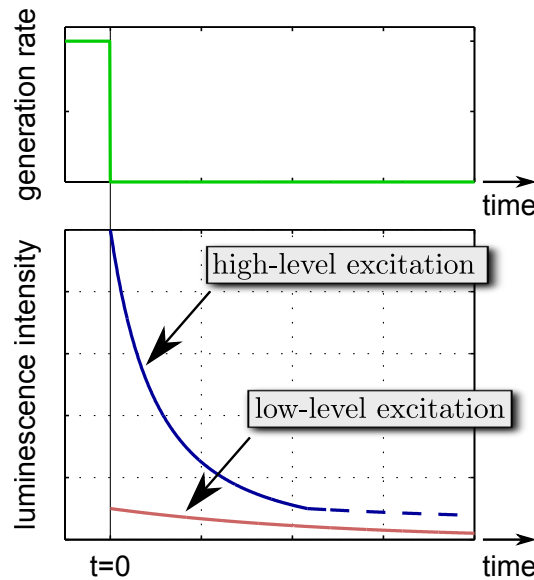


Figure 2.9.: Turnoff transients for low-level and high-level excitation.

The emission spectrum of the LED is usually derived based on carrier density distributions of Eqs. (2.11) and (2.12) on page 22. The corresponding emission is character-

ized by a peak emission at $\hat{E} = E_g + 0.5kT$ and a full width at half maximum (FWHM) of about $1.8kT$ [34]. The spectral width of the emitted light is typically bounded to several tens of nanometers, and is hence perceived by the human eye as monochromatic.

2.4. Heterojunctions

The theory of radiative recombination, as given by Eq. (2.24) on page 28 infers that the device structure of an LED should ideally guarantee carrier densities n and p which, for a given external carrier injection, are as high as possible and further be constant along the semiconductor volume to ensure a well-defined optical emission.

The widely-spread carrier distributions caused by diffusion processes in the pn junction are therefore detrimental. As a result, virtually all modern LEDs rely on more sophisticated semiconductor junction designs such as the double heterostructure (DH) or quantum well (QW) structure, which employ a spatial confinement of carriers. The pn junction made of a single semiconductor material is also referred to as a *homo junction*. Carrier confining semiconductor junctions composed of different semiconductors are referred to as *hetero junctions*.

2.4.1. Double Heterostructure

The energy band structure of a double heterostructure (DH) is schematically shown in Fig. 2.10, where, for the sake of simplicity, the impact of doping is not considered. A layer of a semiconductor with a band gap energy E_g and width W_{DH} is sandwiched between two cladding layers of a second semiconductor with a band gap $E_{g,clad} > E_g$.

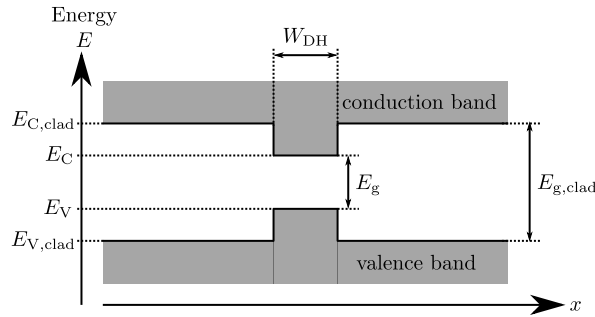


Figure 2.10.: Simplified energy band diagram of a double heterostructure (DH).

With the two cladding layers being p - and n -doped, a carrier confinement may be achieved under forward bias, as illustrated in Fig. 2.11. The cladding semiconductor acts as an energy barrier for the electrons and holes. Ideally, electrons and holes are fully confined within the inner layer of thickness W_{DH} . Then, the active region is restricted to the inner semiconductor layer and hence the band gap E_g determines the emission wavelength of the device.

Photons of energy E_{ph} emitted in the active region will have to pass the cladding layers to exit the device. But due to the energy mismatch $E_{ph} \approx E_g < E_{g,clad}$, re-absorption is unlikely, and hence the cladding layers appear transparent to the photons emitted in the active region.

2. Light-Emitting Diodes: Theoretical Background & Modelling

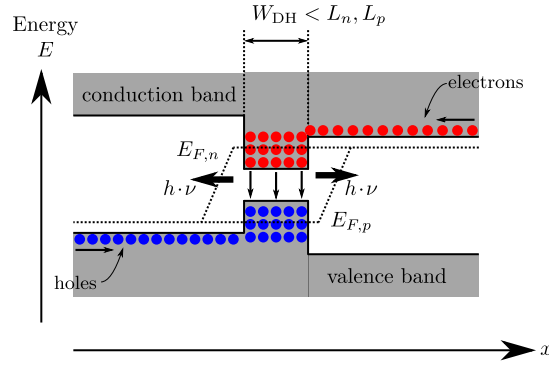


Figure 2.11.: Carrier confinement in a DH under forward bias.

To take advantage of an effective carrier confinement, several design aspects must be satisfied in a DH device:

- To suppress detrimental effects of carrier diffusion in the active region, the width of the active region must be sufficiently small compared to the diffusion lengths; i.e. $W_{\text{DH}} < L_n, L_p$. For example, for an aluminium gallium indium phosphide (AlGaInP) DH LED it was found that $0.15\mu\text{m} \leq W_{\text{DH}} \leq 0.75\mu\text{m}$ should be satisfied [38]. In more recent works, widths in the range of 50 nm to 100 nm were used [39, 40]
- Assuming Boltzmann statistics apply, the carrier distributions within the active region are given by Eqs. (2.11) and (2.12) on page 22. This implies that the barrier heights $\Delta E_V = E_V - E_{V,\text{clad}}$, $\Delta E_C = E_{C,\text{clad}} - E_C$ should be much larger than the thermal energy $E_{\text{th}} = kT$. For example $E_{\text{th}}(300\text{K}) \approx 0.026\text{eV}$ and $\Delta E_g = 0.4\text{eV}$ for GaAs with aluminium gallium arsenide (AlGaAs).
- The active region must usually not be heavily doped. Heavy doping of the active region layer would effectively place a pn junction at one of the interfaces between the cladding and the active region. Typically, the active region is either left undoped or doped with a lower concentration than the cladding layers. For example, for III-V semiconductors, it was observed that a slight p -doping may be beneficial due to the lower hole mobility [38]. Typical doping concentrations are in the 10^{16} to low 10^{17}cm^{-3} range [34] and typical injected carrier densities are in the order of 10^{18}cm^{-3} [41]. As a result, it is typically assumed that the DH device is driven in the regime of high excitation, as introduced in Ch. 2.3.2.
- In order to avoid electrical defects, sufficient matching of the lattice constants of the two semiconductors must be ensured. This limits the choice of semiconductor combinations for a heterojunction. An example is GaAs combined with AlGaAs [1].

2.4.2. Multi Quantum Well

The concept of a DH may be extended to realize devices which exploit quantum effects to improve the emission characteristics.

In a bulk semiconductor carriers are free to move in all three directions (3D). But, as the width of a DH is reduced to a thin layer near the de Broglie wavelength of electrons (≈ 20 nm), carriers are confined in one direction (say x , according to Figure 2.10). Electrons and holes are then confined in a 2-dimensional (2D) system, which is referred to as a quantum well (QW). The theory of quantum mechanics predicts that in a 2D system the density of states (DOS) of both electrons and holes versus energy are no longer given by a square-root shape, as introduced with Eqs. (2.9) and (2.10) on page 22 for the 3D system. As a result, the carrier density distributions $n_E(E)$ and $p_E(E)$ will change compared to the bulk semiconductor, and so will also the spectral emission.

Since the LED device model will be based on integral carrier densities n and p , detailed knowledge of $n_E(E)$ and $p_E(E)$ is not required and the model is, in principle, applicable to both DHs and QWs. However, basic device parameters such as the size of the active volume will be required by the model. Therefore, to find reasonable values for such parameters, the physical foundations of QWs are shortly discussed in the following.

A simplified derivation of the DOS in a QW is obtained when the time-independent Schrödinger equation is applied to a QW of width W_{QW} and *infinite* height, as sketched in Fig. 2.12.

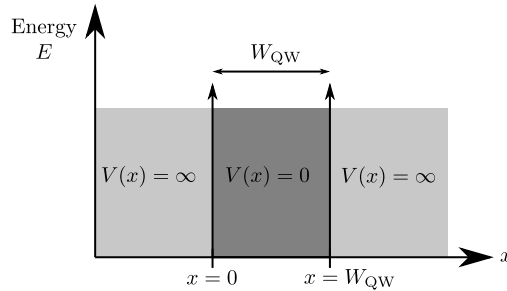


Figure 2.12.: The hypothetical QW of infinite height and width W_{QW} along with the associated potential energy $V(x)$ used for a simplified derivation of the spectral emission.

Considering the x -direction only, the Schrödinger equation of a particle of mass m , which is given as [35]

$$-\frac{\hbar^2}{2m} \frac{\partial^2}{\partial x^2} \psi(x) + V(x)\psi(x) = E\psi(x), \quad (2.40)$$

reduces inside a QW of infinite height to

$$-\frac{\hbar^2}{2m} \frac{\partial^2}{\partial x^2} \psi(x) = E\psi(x), \quad (2.41)$$

with the energy E , and the wave function $\psi(x)$ which describes the particle [37].

2. Light-Emitting Diodes: Theoretical Background & Modelling

With the additional boundary conditions of [35]

$$\psi(0) = \psi(W_{\text{QW}}) = 0, \quad (2.42)$$

the solution to the differential equation (2.41) is of the form

$$\psi(x) = A \sin(kx) \quad \text{with} \quad A = \text{const}, \quad k = \frac{\pi n}{W_{\text{QW}}} \quad (n \in \mathbb{N}). \quad (2.43)$$

Substituting Eq. (2.43) into Eq. (2.41) yields discrete energy states with respect to x of

$$E_x = E_n = \frac{\hbar^2 \pi^2 n^2}{2mW_{\text{QW}}^2} \quad (n \in \mathbb{N}). \quad (2.44)$$

The wave functions for $n = 1, 2, 3$ with the corresponding energy levels in a QW are sketched in Fig. 2.13. Since $E_{e1} > E_c$ and $E_{h1} < E_v$, the minimum energy of a photon emitted from the QW is $E_{11} > E_g$. That is, the emission spectrum of a QW device is blue-shifted with respect to the emission of the same bulk semiconductor.

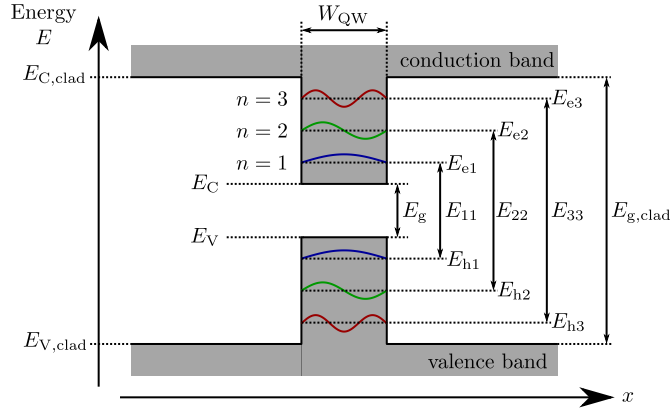


Figure 2.13.: Energy levels in the conduction and valence band of a QW.

The impact of QW width on the first three energy levels of electrons is exemplarily sketched in Fig. 2.14a for a GaAs QW of infinite height.

For an infinite extent of the QW in the yz -plane, however, the Schrödinger equation still yields continuous ranges of allowed energies for the contributions E_y and E_z . In the semiconductor bulk such a domain of allowed energies is called an *energy band*. In a QW, however, due to the discrete nature of E_x , the equivalent domain is referred to as a *subband*. The total energy of an electron or a hole in the n^{th} subband of a QW is generally given as $E = E_n + E_y + E_z$ [35]. That is, the lower bound of each subband is defined by Eq. (2.44).

It can be shown that for the 2D system of a QW, where the in-plane dispersion relation (energy versus momentum) is again assumed to be parabolic, the DOS of an electron or hole of effective mass m^* is constant within a subband and given as [35]

$$\rho_{\text{subband}}^{2\text{D}}(E) = \frac{m^*}{\pi \hbar^2}. \quad (2.45)$$

The total 2D DOS at a particular energy E is the sum over all subbands below that point [35], i.e.

$$\rho^{2D}(E) = \sum_{i=1}^n \Theta(E - E_i), \quad (2.46)$$

where Θ is the unit step function. The resulting 2D DOS of an exemplary GaAs QW is shown in Fig. 2.14b. It is characterized by a staircase shape where the steps are of equal height and occur at E_n . According to Eq. (2.44), the spacing of the unit steps is quadratic with respect to n . A reduction of W_{QW} causes a broadening of the subbands.

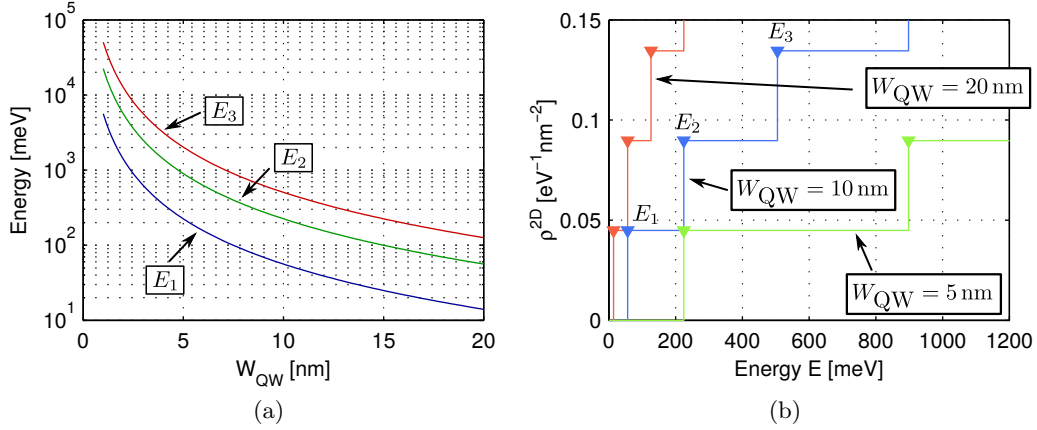


Figure 2.14.: On the simplified derivation of the spectral emission of a QW LED: (a) Subband energy levels for varying width of the QW. (b) The resulting DOS exhibits a staircase shape which is constant within each subband.

In analogy to Eqs. (2.6) and (2.7) on page 21, which describe the carrier densities in the bulk, 2D carrier densities are obtained with

$$n^{2D} = \int_{E_{e1}}^{\infty} n_E^{2D}(E) dE \quad (2.47)$$

$$p^{2D} = \int_{-\infty}^{E_{h1}} p_E^{2D}(E) dE, \quad (2.48)$$

where E_{e1} and E_{h1} are the energy levels of the first subband in the conduction and valence band, respectively. Further holds for each subband (in analogy to Eqs. (2.4) and (2.5) on page 20)

$$n_E^{2D}(E) = \rho_e^{2D}(E) f_e(E), \quad (2.49)$$

$$p_E^{2D}(E) = \rho_h^{2D}(E) f_h(E). \quad (2.50)$$

With the Fermi-Dirac distributions $f_e(E)$, $f_h(E)$ of Eqs. (2.2) and (2.3) on page 19 and a quasi Fermi energy which describe the probability of occupation of the corresponding energy state within each subband.

The corresponding 3D carrier densities established in the QW device are then ap-

2. Light-Emitting Diodes: Theoretical Background & Modelling

proximated by [34]

$$n = \frac{n^{2D}}{W_{\text{QW}}}, \quad p = \frac{p^{2D}}{W_{\text{QW}}}. \quad (2.51)$$

That is, increased carrier densities may be achieved with a reduction of the width of the QW.

The spectral emission of a QW device is characterized by a minimum emission energy of $E_{11} > E_g$ and a resulting FWHM of about $0.7kT$, which is clearly below the value of $1.8kT$ obtained for the bulk emission. This further demonstrates the attractiveness of QW devices over devices with a regular bulk semiconductor.

The small active volume of a single QW, however, limits the optical power emitted from the device. To overcome this limitation, the design of a single QW may be extended to systems employing a multi quantum well (MQW) structure [42]. A simplified sketch of an MQW energy band structure is depicted in Fig. 2.15, where the impact of doping is not considered.

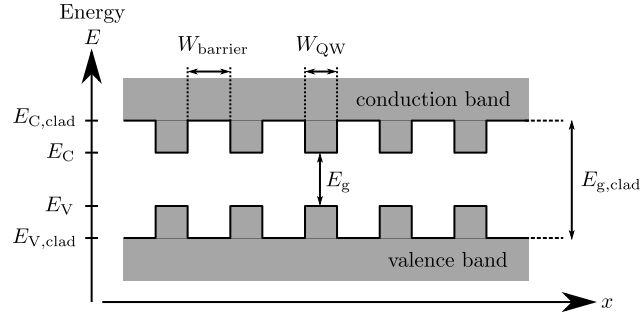


Figure 2.15.: Band diagram of an ideal multi quantum well (MQW) structure with equal barrier widths and equal quantum well widths (without doping).

In MQWs special attention must be paid to the thickness of the cladding layers, i.e. the spacing of the quantum wells. The assumption of Eq. (2.42) that the wavefunction is zero outside the well is an idealization. It is found that the wavefunctions actually decay exponentially in the cladding layers [35]. As a result, adjacent QWs may interact when the thickness W_{barrier} is too small. In that case, the emission characteristics may be altered compared to the characteristics derived above for the single QW. It is found however, that for barrier thicknesses above about 10 nm, the QWs may assumed to be uncoupled [42].

Nevertheless, some practical restrictions are imposed in the design of MQW LEDs. Fluctuations in the widths of the QWs are always present, no matter which growth technique is used. This results in slightly different emission spectra of the different QWs, and as a result, the emission spectrum of the MQW device is broadened compared to the single QW device [42].

Further, as electrons and holes are injected from opposite sides, equal carrier densities n^{2D} , p^{2D} cannot be obtained in all QWs. Experiments with $\text{In}_{0.16}\text{Ga}_{0.84}\text{As}/\text{GaAs}$ LEDs showed that at a given injection current the emission intensity of an MQW LED is in fact a multiple of that of a single QW device [43]. The additional optical power per QW, however, decreases as the number of QWs is increased and the results suggest that a number of quantum wells of $4 < N_{\text{QW}} < 10$ is a good choice.

2.5. Nonradiative Carrier Loss Mechanisms

Electrons and holes which are injected into the active zone of the LED may recombine in several ways. Besides the desired radiative electron-hole recombination described by Eq. (2.24) on page 28, three classes of nonradiative carrier loss mechanisms are typically discussed in the context of modern LEDs.

2.5.1. Shockley-Reed-Hall Recombination

The Shockley-Reed-Hall (SRH) recombination describes the effect that electron-hole pairs may recombine via additional energy levels which are located within the bandgap, as depicted in Fig. 2.16.

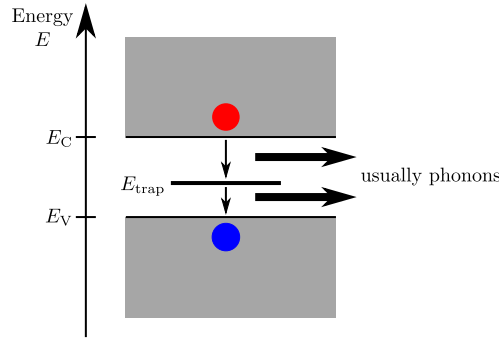


Figure 2.16.: The principle of Shockley-Reed-Hall (SRH) recombination with an additional energy level E_{trap} within the bandgap.

Such energy levels within the bandgap, also referred to as deep levels or traps, may, for example, be caused by native defects or unwanted impurities [34]. Although usually considered being nonradiative with excitation of phonons (vibrations of the semiconductor lattice), SRH recombination may also be of radiative nature with a broad emission spectrum at wavelengths larger than the wavelength defined by the bandgap [44].

In the regime of high excitation (i.e. when the doping concentrations are low compared to the injected carrier densities), as is typically assumed for the active region in a DH or QW, and for $n = p$, the SRH recombination may be described by a recombination rate of [33]

$$R_{\text{SRH}} = A \cdot n. \quad (2.52)$$

The SRH recombination coefficient A is given by the trap density N_t , the thermal velocity v_{th} , and the electron and hole cross sections σ_n, σ_p as [33]

$$A = \frac{1}{(\sigma_n v_{\text{th}} N_t)^{-1} + (\sigma_p v_{\text{th}} N_t)^{-1}} = \frac{N_t \cdot v_{\text{th}}}{\sigma_n^{-1} + \sigma_p^{-1}}. \quad (2.53)$$

Obviously, the concentrations of traps N_t is strongly dependent on fabrication processes, and so is A . Numerical values for A which are of somewhat general validity are therefore hard to find in the literature.

2.5.2. Auger Recombination

Auger recombination describes the effect when the energy which is released by recombination of an electron-hole pair is not emitted in form of a photon, but absorbed by a third particle. The third particle may be an electron (the process is then referred to as "eeh") or a hole (referred to as "hhe") [33]. Various kinds of Auger processes do exist [45,46], two examples are sketched in Fig.2.17.

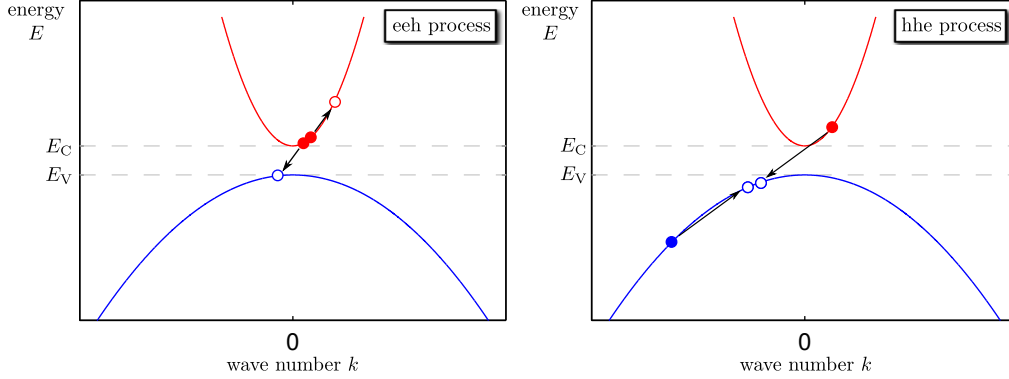


Figure 2.17.: The principle of Auger recombination involving two electrons and one hole (left) and two holes and one electron (right).

Auger recombination is a three-particle process and its probability is $\propto n^2p$ (for eeh) and $\propto np^2$ (for hhe). The corresponding recombination rates may then be written as

$$R_{\text{eeh}} = C_n \cdot n^2p, \quad (2.54)$$

$$R_{\text{hhe}} = C_p \cdot np^2, \quad (2.55)$$

where C_n and C_p are the associated recombination coefficients. Some values for the Auger recombination coefficients C_n and C_p are shown in Table 2.3.

Table 2.3.: Auger recombination coefficients of some semiconductors, according to [33].

Material	C_n in cm^6/s	C_p in cm^6/s
Si, Ge	$2.8 \cdot 10^{-31}$	$9.9 \cdot 10^{-32}$
GaAs, InP	$5.0 \cdot 10^{-30}$	$3.0 \cdot 10^{-30}$

In the regime of high excitation and with $p = n$, the Auger recombination rate is usually written with the help of a single Auger recombination coefficient C as [34]

$$R_{\text{auger}} = (C_n n + C_p p) np = Cn^3 \quad \text{with} \quad C = C_n + C_p. \quad (2.56)$$

In [47] measurements were carried out with AlGaAs and InGaAsP devices in which the corresponding Auger recombination coefficients were determined to be around $C \approx 10^{-29} \dots 10^{-28} \frac{\text{cm}^6}{\text{s}}$.

2.5.3. Carrier Leakage in Heterojunctions

Modern devices based on DHs and QWs are potentially prone to another carrier loss mechanism which is referred to as carrier leakage.

Carrier leakage describes the effect when electrons or holes are generated whose energy exceeds that of the confining energy barrier. This situation is sketched in Fig. 2.18 for electrons, where the carrier distribution $n_E(E)$ is assumed to be given by Eq. (2.11) on page 22.

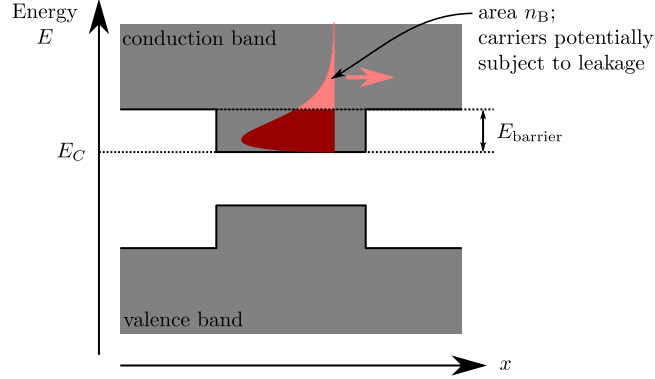


Figure 2.18.: The potential problem of carrier leakage in a double heterostructure (DH) device.

The carrier density which exceeds the confining barrier is calculated by

$$n_B = \int_{E_C + E_{\text{barrier}}}^{\infty} n_E(E) dE. \quad (2.57)$$

These carriers are lost from the active region when they leak into the cladding layers before they recombine (either radiatively or nonradiatively). The corresponding carrier loss may be estimated by calculation of the carriers which drift or diffuse to spatial positions of $x > W_{\text{DH}}$ [34].

An accurate determination of the leakage process requires the detailed knowledge of the carrier dynamics, the carrier distributions $n_E(E)$ and $p_E(E)$, as well as the junction parameters. As a result, a generalized well-accepted description of the leakage process in analogy to Eqs. (2.24), (2.52), (2.56) does not exist. But in the past, leakage rates of the form

$$R_{\text{leak}} = D \cdot n^{3.5} \quad (\text{diffusion}) \quad (2.58)$$

$$R_{\text{leak}} = D \cdot n^{5.5} \quad (\text{drift}) \quad (2.59)$$

were assumed [47, 48].

2.6. Quantum Efficiency

2.6.1. Internal Quantum Efficiency

Carriers injected into the LED will either recombine radiatively or nonradiatively. That is, the desired bimolecular radiative recombination and the undesired nonradiative loss mechanisms are in competition with each other. The relation between radiative and nonradiative recombination rates R_{rad} and R_{nr} therefore defines an internal quantum efficiency of [1, 34]

$$\eta_{\text{int}} = \frac{\text{number of photons emitted from the active region per second}}{\text{number of electrons injected into the LED per second}} \quad (2.60)$$

$$= \frac{P_{\text{int}}/(h\nu)}{I/q} = \frac{R_{\text{rad}}}{R_{\text{rad}} + R_{\text{nr}}}. \quad (2.61)$$

With the electric input current I , optical power P_{int} generated inside the device, the Planck constant h , emission frequency ν , and elementary charge q . For state-of-the-art LEDs, internal efficiencies between 90 % and even 99 % are obtained [34].

2.6.2. External Quantum Efficiency

Photons emitted from the active region are prone to losses which are described by an extraction efficiency of

$$\eta_{\text{extraction}} = \frac{\text{number of photons emitted into free space per second}}{\text{number of photons emitted from the active region per second}}. \quad (2.62)$$

The extraction efficiency takes into account two loss mechanisms which are present in every LED: Re-absorption of photons (either in the semiconductor substrate or in a metallic contact) and losses due to total internal reflection.

The reflection losses are usually estimated under the assumption that light generation within the semiconductor occurs isotropically, i.e. without a preferred direction. The light emitted from the active region experiences refraction at the interface between the semiconductor and the environment (e.g. air). According to Snell's law, the refraction is described by [1]

$$\frac{\sin(\theta_1)}{\sin(\theta_2)} = \frac{n_2}{n_1}, \quad (2.63)$$

where θ_1 and θ_2 are the incident and output angles normal to the material interface, and n_1, n_2 are the refractive indices of the semiconductor and the environment, respectively, as depicted in Fig. 2.19a.

The refractive index of semiconductors is usually high, typically around $n_1 = 3 \dots 4$ [1]. The ambient environment therefore normally exhibits a lower refractive index (e.g. $n_2 = 1$ for air). According to Snell's law, this defines a critical angle of [1]

$$\theta_{\text{max}} = \theta_1 (\theta_2 = 90^\circ) = \sin^{-1} \left(\frac{n_2}{n_1} \right) \approx \frac{n_2}{n_1} \quad (2.64)$$

from which on total internal reflection occurs. For example, for GaAs with $n_1 = 3.66$ and gallium-phosphide (GaP) with $n_1 = 3.45$, the critical angle is about $\theta_{\max} = 16^\circ \dots 17^\circ$.

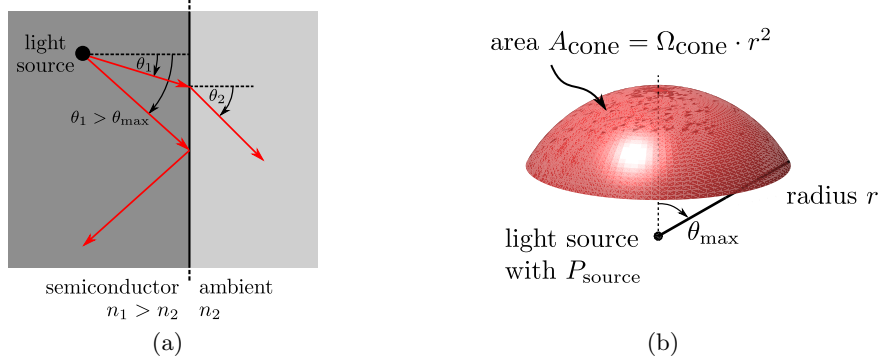


Figure 2.19.: On the derivation of the extraction efficiency: (a) Refraction and total internal reflection according to Snell's law. (b) The light escape cone defined by θ_{\max} .

For an infinitesimal optical point source, which emits an optical power P_{source} , the fraction of optical power which leaves the device may then be calculated by considering the calotte-shaped sphere bounded by θ_{\max} , as depicted in Fig. 2.19b. The resulting fraction of optical power which is coupled out of the LED is defined through the solid angle of the light escape cone

$$\Omega_{\text{cone}} = 2\pi [1 - \cos(\theta_{\max})] \quad (2.65)$$

and the total solid angle of a sphere $\Omega_{\text{sphere}} = 4\pi$ as [34]

$$\frac{P_{\text{escape}}}{P_{\text{source}}} = \frac{\Omega_{\text{cone}}}{\Omega_{\text{sphere}}}. \quad (2.66)$$

This gives an emitted optical power of

$$\begin{aligned} P_{\text{escape}} &= \frac{P_{\text{source}}}{2} \cdot [1 - \cos(\theta_{\max})] \\ &\dots \text{with a truncated Taylor series expansion of } \cos(x) \dots \\ &\approx \frac{P_{\text{source}}}{4} \cdot \theta_{\max}^2 \\ &\approx \frac{P_{\text{source}}}{4} \cdot \frac{n_2^2}{n_1^2}. \end{aligned} \quad (2.67)$$

For typical semiconductors, with a planar surface, and neglecting re-absorption this results in an extraction efficiency for the LED of about

$$\eta_{\text{extraction}} = \frac{P_{\text{escape}}}{P_{\text{source}}} \approx 5\%. \quad (2.68)$$

2. Light-Emitting Diodes: Theoretical Background & Modelling

With the internal efficiency η_{int} introduced in Ch. 2.6.1, the efficiency of the E/O conversion of the LED is described by an external quantum efficiency of

$$\begin{aligned}\eta_{\text{external}} &= \frac{\text{number of photons emitted into free space per second}}{\text{number of electrons injected into the LED per second}} \\ &= \frac{P/(h\nu)}{I/q} = \eta_{\text{int}} \cdot \eta_{\text{extraction}},\end{aligned}\tag{2.69}$$

with the optical output power P and the electric input current I .

2.7. A Simplified Model of Communication LEDs

For the development processes of LEDs, commercial device simulation software, such as APSYS [49] or NEXTANO [50] exist. However, such software is intended to physically model the optoelectronic device as accurate as possible, requiring 3D numerical simulations.

This is not a feasible approach to be used in a communication system context. Here, simple system-theoretic device models of all system components are required which may then be concatenated to build up the whole communication channel. With this motivation, a reduced-complexity LED device model is derived, which describes the linear and nonlinear modulation response in a fully analytical fashion using device parameters which can easily be found in the literature.

The thesis at hand restricts the device modelling to LEDs which are designed for fiber-based optical short-range communication. For POF communication, these devices are typically red-emitting at $\lambda = 650$ nm. Common values for the optical output power are in the eye-safe region of $P \leq 1$ mW $\hat{=} 0$ dBm at input currents of several tens of milliamps.

The model shall describe the E/O conversion of the directly modulated LEDs based on the basic physical phenomena presented in Chapters 2.1 to 2.6. For commercial LEDs, however, most of the design parameters presented in the previous chapters are usually confidential, and hence unknown to the enduser. As a result, the model shall require as few device parameters as possible to accurately describe the linear and nonlinear modulation response of the device.

The model is applied to DH and QW devices, which exhibit negligible doping of the active zone and hence are driven in a regime of high excitation, as described in Ch. 2.3.2. However, the potential impact of doping of the active region is also discussed in Appendix A. In order to be applicable to both DHs and QWs, the integral carrier densities n and p of Eqs. (2.6) and (2.7) on page 21 are used. That is, the underlying shapes of $n_E(E)$ and $p_E(E)$, which are different for DHs and QWs, are not considered. It is also assumed that the carriers are equally distributed within the active volume, and further $p = n$.

Nonradiative recombination mechanisms, as described in Ch. 2.5 are assumed to be negligible. This implies that the carrier confining barriers are high compared to the highest energy level occupied by the carriers, so that carrier leakage is negligible. It further implies that the resulting carrier densities are in a regime where radiative recombination dominates over Auger recombination. It shall be noted that, due to the neglect of these higher-order recombination terms, the resulting device model is ex-

2.7. A Simplified Model of Communication LEDs

pected to describe a lower bound of nonlinearities originated in an LED driven in a high excitation regime.

With these assumptions, the E/O conversion of the communication LED is described by the carrier density rate equation (2.38) on page 30. Setting $n = \Delta n$ (motivated by the previously introduced condition $\Delta n \gg (p_0 + n_0)$ for high-level excitation) gives

$$\frac{dn(t)}{dt} = G - R_{\text{rad}} = \frac{i_{\text{LED}}(t)}{qV_{\text{active}}} - B [n(t)]^2, \quad (2.70)$$

where $n(t)$ is the 3D carrier density in the active volume. The radiative recombination rate R_{rad} is given by Eq. (2.37) on page 30 with the radiative recombination coefficient B , and the generation rate G is given by the LED input current $i_{\text{LED}}(t)$ and the active volume V_{active} , as introduced by Eq. (2.16) on page 24.

Assuming further spatially uniform carrier densities $n(x) = n = p$, the total optical power emitted from the active region is then given as

$$\begin{aligned} p_{\text{opt}}(t) &= \eta_{\text{extraction}} E_{\text{ph}} \int_{V_{\text{active}}} R_{\text{rad}}(t) dV \\ &= \eta_{\text{extraction}} E_{\text{ph}} V_{\text{active}} R_{\text{rad}}(t) \\ &= \underbrace{\eta_{\text{extraction}} E_{\text{ph}} V_{\text{active}} B}_{:=A_P} \cdot [n(t)]^2, \end{aligned} \quad (2.71)$$

with the photon energy E_{ph} given by Eq. (2.1) on page 19 and

$$V_{\text{active}} = \begin{cases} A_{\text{active}} \cdot W_{\text{DH}} & \text{for the DH device} \\ A_{\text{active}} \cdot W_{\text{QW}} \cdot N_{\text{QW}} & \text{for the QW device.} \end{cases} \quad (2.72)$$

Equations (2.70) to (2.72) are the basis of the simplified physical model describing the E/O conversion of the LED. From this physical model a simplified analytical description of the linear and nonlinear frequency responses will be derived.

In order to allow a model verification with measurements of commercial communication LEDs, realistic device parameters must be known. Device parameters such as the active volume etc. are easily found in the literature, and typical ranges for all the parameters, as well as the parameters used in the remainder of this thesis will be given in the next section.

However, finding an appropriate value for the radiative recombination coefficient B is not so trivial. The reason is that the simplified assumption of $R_{\text{rad}} = Bnp$ neglects the effects of the k -selection rule. To take into account the effects of the k -selection rule, a non-constant recombination coefficient is often introduced [34]. Figure 2.20 shows exemplarily the electron distribution for the semiconductor bulk versus energy for a fixed n at two different temperatures (left) and at a fixed temperature for two different values of n (right). It is seen that the range of occupied energy levels increases with both T and n .

Taking into consideration the dispersion relation of Fig. 2.3 on page 21, this causes an increasing spread of the carriers in the k -space and hence a reduced carrier density per dk interval. As a result, it is expected that the recombination coefficient decreases with both the junction temperature T , as well as carrier density n . The recombination

2. Light-Emitting Diodes: Theoretical Background & Modelling

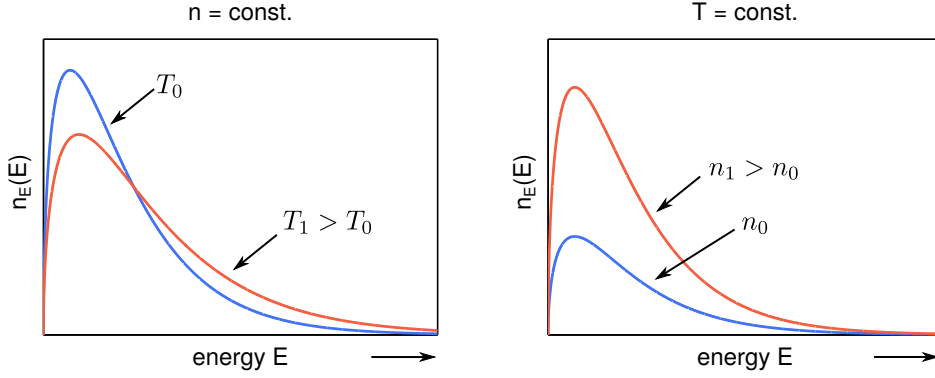


Figure 2.20.: The impact of temperature (left) and carrier density (right) on the carrier distribution.

coefficient B may then be written as

$$B_{\text{LED}} = B(T, n).$$

This temperature and carrier density dependence of B is well known and was addressed in numerous publications in the past, for example in [34, 47, 51–54].

Equations (2.70) to (2.72) model the carrier dynamics under the assumption of a constant radiative recombination coefficient B . The effects of a non-constant B can only be incorporated for physical effects that introduce a "slowly" varying B . That is, the time constants of such a non-constant B must be much larger than the time-constants of the carrier dynamics obtained from the simplified model Eqs. (2.70) to (2.72).

The time constant of a non-constant $B(n)$ must be considered small compared to the carrier dynamics of the LED device model. For example, the relaxation time of electrons in GaAs until the thermal distribution of Eq. (2.11) is reached was found to be in the order of some tens of picoseconds [55]. This is well below any time constants associated with a device bandwidth in the order of ≤ 100 MHz. As a result, the effects of a $B(n)$ cannot be covered by the device model based on Eqs. (2.70) to (2.72).

The thermal time constant of a device, which introduces a non-constant $B(T)$, however, is found to be typically ≥ 1 ms [56]. This may be considered to be slowly varying and hence it may be assumed that when the LED is driven with a unipolar (i.e. biased) modulation signal, only the bias affects the device temperature, and not the modulation signal. As a result, the LED model of Eqs. (2.70) to (2.72) does allow to include a non-constant

$$B_{\text{LED}} = B(T). \quad (2.73)$$

Nevertheless, a constant B will be used throughout the simulations and calculations and the impact of $B(T)$ will be addressed in form of a correction factor afterwards. This is motivated by two aspects: 1) Although simplified models of $B(T)$ do exist, they lack accuracy when compared with actual measurements. 2) The model shall be as simple as possible, and hence using a simple correction factor for $B(T)$ is a very attractive approach. Although not included in the model itself, the potential impact of $B(n)$ will also be shortly discussed in this context, based on typical values found in the literature.

3. Verification of the Carrier Density Rate Equation Model

The simplified LED model introduced in the previous section shall be verified by comparing the model's E/O characteristics with those of commercially available communication LEDs.

The model is verified in terms of:

The static P-I: The optical output power P when the LED is driven with different DC input currents I .

The frequency response: The frequency response of the E/O conversion is investigated when the LED is modulated with a biased electrical input signal

Higher-order harmonics: Higher-order harmonics in the optical output signal are evaluated when the LED is modulated with a biased singletone signal of the form $i_{\text{LED}}(t) = I_0 + I_1 \cos(2\pi ft)$ with a fixed input amplitude I_1 , but varying frequency f .

Second-order intermodulation products: Second-order intermodulation products in the optical output signal are evaluated when the LED is modulated with a biased twotone signal of the form $i_{\text{LED}}(t) = I_0 + I_1 \cos(2\pi f_1 t) + I_2 \cos(2\pi f_2 t)$. Here, special attention is paid to the impact of varying input frequencies f_1, f_2 .

In a real application, communication LEDs are always driven with a large-signal modulation (cf. Fig. 2.7 on page 25). The model is therefore primarily to be verified for large-signal modulation. For this verification two commercial LEDs are used: Hamamatsu L8045 and Avago SFH757V. Both devices are red-emitting around $\lambda = 650$ nm and are designed for optical short-range communication using POFs. The outer mechanical structure of the two devices is totally different. Model L8045 is encapsulated in a plastic package of about $5 \text{ mm} \times 4 \text{ mm} \times 2 \text{ mm}$, model SFH757V is encapsulated in a large plastic housing for connection of a POF, with overall dimensions of about $24 \text{ mm} \times 9 \text{ mm} \times 9 \text{ mm}$.

In addition to the large-signal verification, which is performed at a fixed bias, the LED device model is also verified at different bias points I_0 using a reduced modulation amplitude I_1, I_2 . However, as this requires time-consuming laboratory measurements, these additional model verifications are only done with the LED model L8045. It shall be noted that measurements at small-signal modulation are limited by SNR and sensitivity constraints of the measurement equipment. The model verification at varying input bias is therefore conducted using a modulation amplitude which is reduced by a factor of 2 compared to the large-signal modulation.

The device parameters required by the carrier density rate equation model are listed in Table 3.1 along with typical, well-accepted values given in the literature. The param-

3. Verification of the Carrier Density Rate Equation Model

eters used in this work for the model verification are based on the value ranges found in the literature and are also listed in Table 3.1.

The model may be applied to both QW, as well as DH structures. The active volume in Eq. (2.70) on page 43 is given for the DH and QW device as

$$V_{\text{active,DH}} = A_{\text{active}} \cdot W_{\text{DH}}, \quad (3.1)$$

$$V_{\text{active,QW}} = A_{\text{active}} \cdot N_{\text{QW}} \cdot W_{\text{QW}}. \quad (3.2)$$

Table 3.1.: LED device parameters required by the simplified carrier density rate equation model.

symbol	description	unit	typical values	used in this work
B	bimolecular recombination coefficient	cm^3/s	$10^{-11} \dots 10^{-9}$ [34]	10^{-10}
A_{active}	cross section of the active volume	μm^2	$250^2 \dots 350^2$ [34, 57]	280^2
N_{QW}	number of QWs	dimensionless	$4 \dots 10$ [43, 58, 59]	8
W_{QW}	thickness of the QWs	nm	≤ 10 [1]	5
W_{DH}	thickness of the DH's active layer	nm	$\approx 50 \dots 750$ [38, 39]	(not used)
η_{int}	internal efficiency	dimensionless	$> 90\%$ [34]	100%
$\eta_{\text{extraction}}$	extraction efficiency	dimensionless	$< 5\%$ [34]	2.5%

The E/O conversion of the device model is simulated by solving Eq. (2.70) for $n(t)$ in the time domain using the well-known Runge-Kutta method for numerical integration [60, 61].

3.1. Static P-I

The device model shall be verified for DC input currents up to the maximum rated currents given in the data sheets of the two investigated LEDs. The values are given in Table 3.2.

Table 3.2.: Maximum input currents of the two investigated LEDs, according to the data sheets [62, 63].

device	I_{\max} in mA
L8045	40
SFH757V	50

3.1.1. Carrier Density Rate Equation Model

The simulation model uses the device parameters of Table 3.1. The simulation result of the static P-I for an input current of up to 50 mA is shown in Fig. 3.1. The static P-I is linear over the entire investigated input current range with an optical output power of about 2.4 mW at 50 mA.

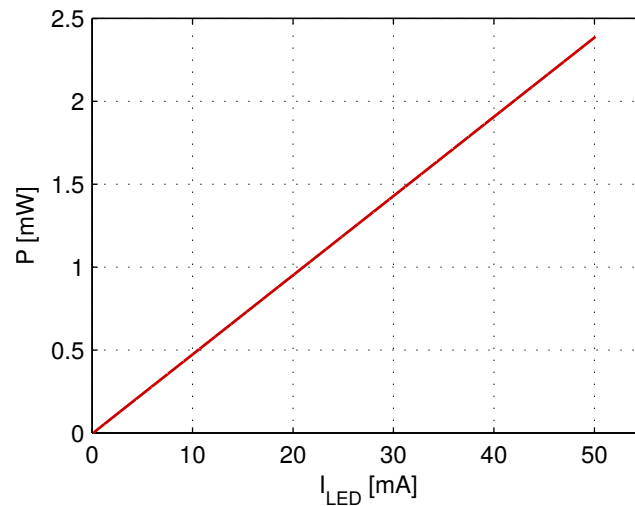


Figure 3.1.: Optical output power versus electrical input current for the device model of Ch. 2.7 (numerical simulation with the parameters of Table 3.1).

The simulation model allows to gain insight in the underlying carrier dynamics. Figure 3.2 shows the corresponding 3D carrier density $n(t)$. The curve shows a strong nonlinear behaviour with a square-root-like shape. This demonstrates that, although the static E/O conversion is linear, the underlying physics are basically given by a nonlinear process which describes the transition from the input current $i(t)$ to the resulting carrier density $n(t)$, in combination with the nonlinear relation between $n(t)$ and optical output power $p_{\text{opt}}(t)$ (given by Eq. (2.71) on page 43). The simulated values of $n(t)$ reach about $10^{18} \frac{1}{\text{cm}^3}$ at an input current of 50 mA, which is a realistic order of magnitude, see for example [41].

3. Verification of the Carrier Density Rate Equation Model

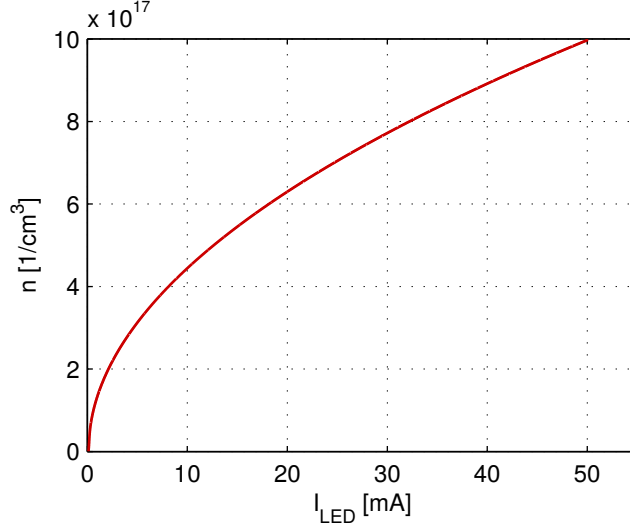


Figure 3.2.: 3D carrier density versus electrical input current for the device model of Ch. 2.7 (numerical simulation with the parameters of Table 3.1).

3.1.2. Measurements

For all laboratory measurements, the LEDs are placed in a small free-space optical (FSO) setup, as depicted in Fig. 3.3. The LED under test is placed in the vicinity of the focus of a collimating lens. The collimated output of this first lens is focused with a second lens and coupled into an optical power meter. The focal lengths of the different lenses (F_1, F_2 in Fig. 3.3) are about 1 cm to 2.5 cm. Due to the relatively wide opening angle of the light emitted from the LEDs, the lenses cannot capture the entire emission. The distances d_1, d_2 are therefore slightly defocussed to maximize the power coupled into the power meter. The DC current is delivered by a lab power supply with a series resistor of 100Ω .

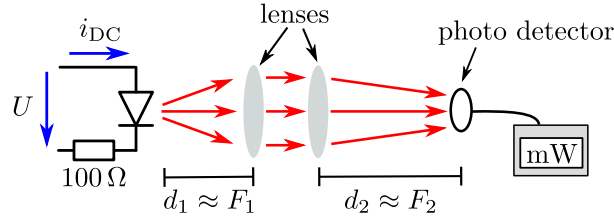


Figure 3.3.: Laboratory setup for measurement of the static P-I.

The static P-I of the two devices measured up to the maximum input DC currents of Table 3.2 are shown in Fig. 3.4, along with a linear fit. Both curves show good linearity, a nonlinear behaviour such as a saturation at high input currents is not observed.

The measured optical output power is about 1 mW at 40 mA (L8045) and 0.8 mW at 50 mA (SFH757V). The lower output power of model SFH757V compared to L8045 is most likely due to the fact that the housing of SFH757V, which is designed for POF connection, causes higher losses in the FSO measurement setup. The measured power of L8045 is about a factor of 2 below the simulated one shown in Fig. 3.1.

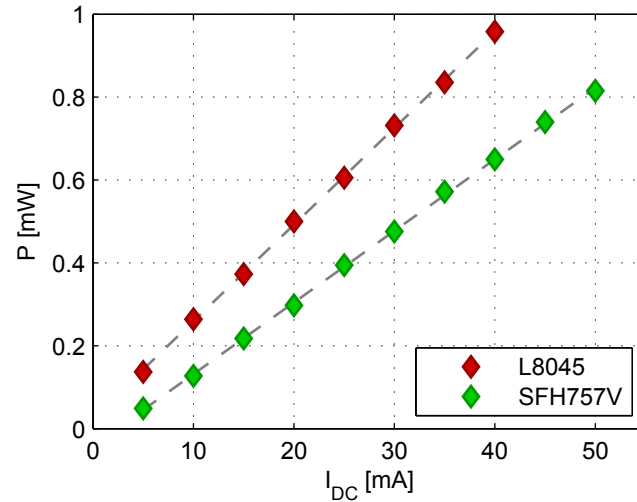


Figure 3.4.: Optical output power versus electrical input current for the commercial LED models L8045 and SFH757V (dashed lines: linear fit).

The fact that the simulation overestimates the optical output power makes perfect sense, since the model neglects some additional loss mechanisms. The most likely origins for these additional losses are: Path losses in the FSO setup due to the fact that the lenses do not capture the entire LED emission. Furthermore, the model neglects losses in the carrier injection due to effects such as leakage currents. Finally, although incorporated in the model, the extraction efficiency $\eta_{\text{extraction}} = 2.5\%$ is only a rough estimate. Equation (2.67) shows that $\eta_{\text{extraction}}$ scales inversely with the square of the refractive index of the semiconductor. Hence, even moderate differences in the refractive index may cause noticeable differences of $\eta_{\text{extraction}}$.

3.1.3. Summary

The simplified device model predicts a linear relationship between DC input current and optical output power. With the device parameters of Table 3.1 (which are chosen based on well accepted values from the literature) the simulated output power lies in the low milliwatt regime for input currents of up to 50 mA. Taking into consideration additional loss mechanisms, this is in good agreement with the lab measurements obtained for the investigated commercial communication LEDs.

The measured static P-I curves showed good linearity up to the maximum rated input currents. However, although linear E/O conversion was observed in both simulation and measurement, the device model introduced in Ch. 2.7 predicts that the physical process of the E/O conversion is mathematically described by two nonlinear functions, cf. Eqs. (2.70) and (2.71) on page 43f.

3. Verification of the Carrier Density Rate Equation Model

3.2. Frequency Response

The frequency response of the E/O conversion is one of the key parameters in the context of communication systems. Hence, good agreement between the measured and the simulated frequency responses is considered crucial for an accurate model of communication LEDs.

The frequency responses of the device model and the commercial LEDs are compared for large-signal modulation at a fixed bias and for varying input bias with a reduced modulation amplitude. The latter shall approximate the small-signal modulation behaviour.

3.2.1. Large-Signal Modulation at a Fixed Input Bias

Carrier Density Rate Equation Model

The electrical input signal is a biased onetone signal of

$$i_{\text{LED}}(t) = I_0 + I_1 \cos(2\pi ft + \phi_{\text{in}}), \quad (3.3)$$

where the input phase is set to $\phi_{\text{in}} = 0$. The values for I_0 and the modulation amplitude I_1 are chosen such that the specified input current ranges of the commercial devices are fully exploited. In a commercial communication system this would be motivated by a maximization of the received SNR. Therefore, the bias is set to $I_0 = I_{\text{max}}/2$. To avoid clipping effects at $i_{\text{LED}}=0$ mA, a modulation index of $m = 0.9$ is used. The resulting input bias and modulation amplitudes are given in Table 3.3.

Table 3.3.: Large-signal modulation parameters used in the measurements.

	L8045	SFH757V
I_0	20 mA	25 mA
$i_{\text{mod,pp}} = 2I_1$	36 mA	45 mA

For the remainder of this thesis, dB signal levels are calculated in terms of electrical signal power, i.e.

$$[\text{dB}] := 20 \cdot \log_{10} \left(\frac{A_{\text{el}}}{A_0} \right),$$

where A_{el}/A_0 represents the normalized electrical amplitude (either current or voltage). This is motivated from a communication point of view, since the dominant source of noise is assumed to be found in the electrical receive circuitry [8].

The simulated frequency responses are shown in Fig. 3.5, along with a fit of a 1st-order lowpass of the form

$$\underline{H}(\omega) = \frac{1}{1 + j \frac{\omega}{\omega_c}} \quad (\omega_c = 2\pi f_c = -3 \text{ dB cutoff frequency}). \quad (3.4)$$

It is seen that the frequency responses are well approximated with a 1st-order lowpass characteristic. The cutoff frequencies of the simulated frequency responses are given in Table 3.4.

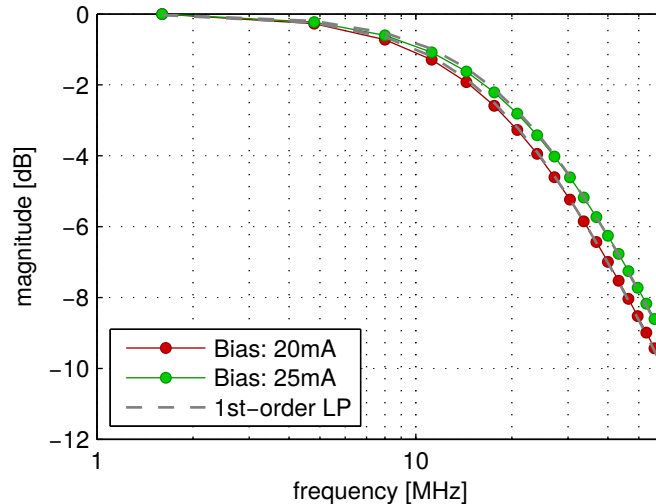


Figure 3.5.: Simulated frequency responses for large-signal modulation with the device parameters of Table 3.1.

Table 3.4.: Simulated cutoff frequencies obtained for the modulation parameters of Table 3.3

	L8045	SFH757V
f_c	19.6 MHz	21.9 MHz

The simulated large-signal frequency responses shall be compared with the measured frequency responses of the two LED models.

Measurements

For the measurement of the modulation characteristics, the FSO measurement setup is now extended as depicted in Fig. 3.6.

The transmit signal is generated offline in Matlab and loaded to an arbitrary waveform generator (AWG). The bipolar output signal of the AWG is amplified with an RF amplifier and positively biased with a bias-T. The unipolar voltage is converted to a unipolar current by a $100\ \Omega$ resistor, which drives the LED under test. The transmit signal's amplitude is monitored with a broadband probe (LeCroy ZS4000). The optical output signal of the LED is coupled to a commercially available broadband (1 GHz) PIN-diode-based optical receiver (Graviton SPA-2). To ensure, that the receiver is driven in a linear regime, the optical signal is attenuated with neutral density (ND) filters¹. The electrical receive signal is captured with a broadband digital sampling oscilloscope (DSO) and processed offline in Matlab. To avoid clipping effects at $i_{LED}=0\ \text{mA}$, a slight margin of the modulation amplitude is introduced to ensure strictly positive input signals. That is, a modulation index of $m < 1$ is used (cf. Eq. (2.17) on page 25).

¹Linearity of the receiver was verified by investigating higher-order harmonics in the received signal for different optical attenuations.

3. Verification of the Carrier Density Rate Equation Model

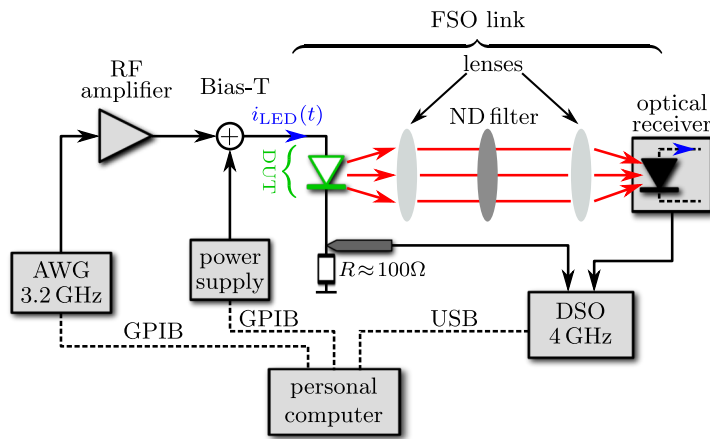


Figure 3.6.: Laboratory setup for measurement of the LED's modulation characteristics.

The measured frequency responses of the two commercial LEDs are shown in Fig. 3.7, again with a fit of a 1st-order lowpass of Eq. (3.4).

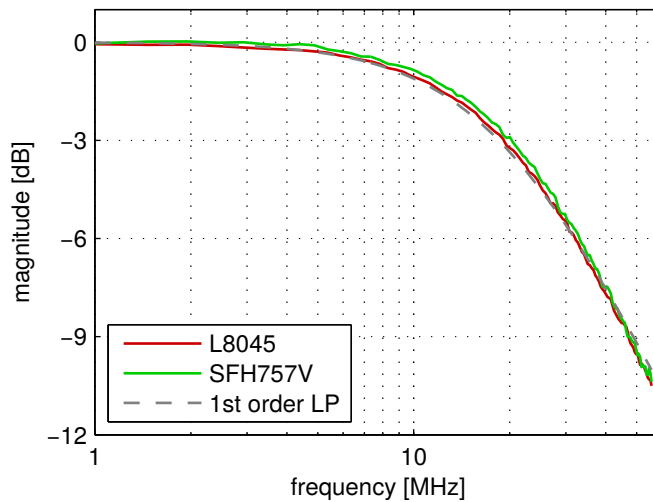


Figure 3.7.: Frequency responses of the E/O conversion for the commercial LED models L8045 and SFH757V.

The two devices exhibit nearly the same magnitude responses, fitting well with that of the 1st-order lowpass transfer function. The measured -3 dB cutoff frequencies are given in Table 3.5. The values fit well with the simulated ones of Table 3.4. Potential origins for the slight discrepancies could, for example, be a parasitic lowpass behaviour of the LED driving circuitry.

Table 3.5.: Measured cutoff frequencies obtained for the modulation parameters of Table 3.3

	L8045	SFH757V
f_c	18.5 MHz	19.2 MHz

Device Parameter Fitting

The E/O conversion of the LED is described by Eqs. (2.70) and (2.71) on page 43f. The carrier density rate equation (2.70) requires numerical solving techniques and does not give an analytical description of the resulting frequency response. Under simplifying assumptions, however, the frequency response of the E/O conversion may be derived.

It is assumed that the LED is modulated with a harmonic electrical input signal as introduced with Eq. (3.3) of the form

$$\begin{aligned}
 i(t) &= I_0 + I_1 \cdot \cos(2\pi f_1 t + \phi_I) \\
 &= I_0 + I_1 \cdot \left[\frac{e^{j(2\pi f_1 t + \phi_I)}}{2} + \frac{e^{-j(2\pi f_1 t + \phi_I)}}{2} \right] \\
 &= I_0 + I_1 \cdot \left[\frac{e^{j(\omega_1 t + \phi_I)}}{2} + \frac{e^{-j(\omega_1 t + \phi_I)}}{2} \right] \\
 &= I_0 + \frac{1}{2} [I_1 \cdot e^{j\omega_1 t} + I_1^* \cdot e^{-j\omega_1 t}], \tag{3.5}
 \end{aligned}$$

where the bias is represented by the subscript 0, and the harmonic tone is represented by the subscript 1. The magnitude I_1 and phase ϕ_I of the harmonic tone are found in the complex-valued term

$$I_1 = I_1 \cdot e^{j\phi_I}.$$

Assuming that in a small-signal scenario only these two frequencies are present throughout the E/O conversion process, the carrier density $n(t)$ and optical output power $p_{\text{opt}}(t)$ may be formulated likewise, i.e.

$$\begin{aligned}
 n(t) &= N_0 + N_1 \cdot \cos(\omega_1 t + \phi_N) \\
 &= N_0 + \underbrace{\frac{1}{2} [N_1 \cdot e^{j\omega_1 t} + N_1^* \cdot e^{-j\omega_1 t}]}_{:=n_1(t)}, \tag{3.6}
 \end{aligned}$$

with

$$N_1 = N_1 \cdot e^{j\phi_N}.$$

And

$$\begin{aligned}
 p_{\text{opt}}(t) &= P_0 + P_1 \cdot \cos(\omega_1 t + \phi_P) \\
 &= P_0 + \underbrace{\frac{1}{2} [P_1 \cdot e^{j\omega_1 t} + P_1^* \cdot e^{-j\omega_1 t}]}_{:=p_1(t)}, \tag{3.7}
 \end{aligned}$$

with the magnitude and phase of the output tone given in

$$P_1 = P_1 \cdot e^{j\phi_P}.$$

With $n(t)$ from Eq. (3.6), the optical output power of Eq. (2.71) on page 43 writes as

3. Verification of the Carrier Density Rate Equation Model

$$\begin{aligned} p_{\text{opt}}(t) &= A_P \cdot [n(t)]^2 = A_P \cdot [N_0 + n_1(t)]^2 \\ &= A_P \cdot [N_0^2 + 2N_0n_1(t) + [n_1(t)]^2], \end{aligned} \quad (3.8)$$

with the previously introduced scaling factor $A_P = \eta_{\text{extraction}} E_{\text{ph}} V_{\text{active}} B$.

According to Eq. (3.6), the signal components N_0 and $n_1(t)$ are harmonic signals at the frequencies 0 and $\pm\omega_1$, and hence the summands in the square brackets on the right-hand side of Eq. (3.8) correspond to harmonic output signals at frequencies

$$\begin{aligned} 0 & \text{ for } N_0^2 \\ \pm\omega_1 & \text{ for } 2N_0n_1(t) \\ \pm 2\omega_1, 0 & \text{ for } [n_1(t)]^2. \end{aligned}$$

The magnitude and phase of the optical output power at the signal frequency $+\omega_1$ is therefore given by the cross term $2N_0n_1(t)$, which writes with Eq. (3.6) as

$$\begin{aligned} \frac{P_1}{2} e^{j\omega_1 t} &= A_P \cdot 2N_0 \frac{N_1}{2} e^{j\omega_1 t} \\ \frac{P_1}{2} &= A_P \cdot 2N_0 \frac{N_1}{2}. \end{aligned} \quad (3.9)$$

The spectral components N_0 and N_1 of the carrier density, which are required for the calculation of P_1 , are derived by putting Eqs. (3.5) and (3.6) into the carrier density rate equation (2.70) on page 43.

The derivative on the left-hand side of Eq. (2.70) gives

$$\frac{d}{dt} n(t) = \frac{N_1}{2} j\omega_1 e^{j\omega_1 t} - \frac{N_1^*}{2} j\omega_1 e^{-j\omega_1 t}. \quad (3.10)$$

Equation (3.10) contains tones at $\pm\omega_1$. The right-hand side of Eq. (2.70) writes as

$$\begin{aligned} \frac{i(t)}{qV_{\text{active}}} - B[n(t)]^2 &= \frac{I_0 + \frac{I_1}{2} e^{j\omega_1 t} + \frac{I_1^*}{2} e^{-j\omega_1 t}}{qV_{\text{active}}} \\ &\quad - B \left[N_0^2 + 2N_0 \left[\frac{N_1}{2} e^{j\omega_1 t} + \frac{N_1^*}{2} e^{-j\omega_1 t} \right] + \left[\frac{N_1}{2} e^{j\omega_1 t} + \frac{N_1^*}{2} e^{-j\omega_1 t} \right]^2 \right]. \end{aligned} \quad (3.11)$$

Equation (3.11) contains tones at frequencies 0, $\pm\omega_1$, $\pm 2\omega_1$.

The spectral components N_0 and N_1 of the carrier density at the frequencies 0 and ω_1 may be determined by separating these two frequency components in Eqs. (3.10) and (3.11). This approach requires that the frequency components in Eqs. (3.10) and (3.11) are independent of each other, which is valid in a small-signal assumption for the corresponding frequency components of $n(t)$ (i.e. $|N_1|^2/2 \ll N_0^2$). This assumption is motivated by the fact that the unipolarity of $n(t)$ sets an upper limit to the modulation amplitude. In a modulation scenario with data transmission, where a certain bandwidth is occupied, it is assumed that this reduces the frequency components to a small-signal

scenario.

For the DC component ($\omega_0 = 0$), Eqs. (3.10) and (3.11) then give

$$0 = \frac{I_0}{qV_{\text{active}}} - BN_0^2 \quad (3.12)$$

or

$$N_0 = \sqrt{\frac{I_0}{qV_{\text{active}}B}}. \quad (3.13)$$

And for the spectral component at ω_1 , Eqs. (3.10) and (3.11) give

$$\begin{aligned} j\omega_1 \frac{N_1}{2} e^{j\omega_1 t} &= \frac{\underline{I}_1 e^{j\omega_1 t}}{qV_{\text{active}}} - B2N_0 \frac{N_1}{2} e^{j\omega_1 t} \\ j\omega_1 N_1 &= \frac{\underline{I}_1}{qV_{\text{active}}} - B2N_0 N_1. \end{aligned} \quad (3.14)$$

Re-arranging yields

$$\begin{aligned} N_1(\omega_1) &= \frac{\underline{I}_1}{qV_{\text{active}}} \cdot \frac{1}{j\omega_1 + 2BN_0} \\ &= \frac{\underline{I}_1}{qV_{\text{active}}} \cdot \frac{1}{2BN_0} \cdot \frac{1}{j\frac{\omega_1}{2BN_0} + 1}. \end{aligned} \quad (3.15)$$

Equation (3.15) describes the magnitude and phase of the tone $n_1(t)$ at the frequency ω_1 as a function of various device parameters and the signal frequency ω_1 . It is seen that $N_1(\omega_1)$ exhibits a low-pass characteristic.

Putting Eqs. (3.13) and (3.15) into Eq. (3.9) gives

$$\begin{aligned} \frac{\underline{P}_1(\omega_1)}{2} &= A_P \cdot N_0 \frac{\underline{I}_1}{qV_{\text{active}}} \cdot \frac{1}{2BN_0} \cdot \frac{1}{j\frac{\omega_1}{2BN_0} + 1} \\ \underline{P}_1(\omega_1) &= A_P \cdot \frac{\underline{I}_1}{qV_{\text{active}}B} \cdot \frac{1}{j\frac{\omega_1}{2BN_0} + 1}. \end{aligned} \quad (3.16)$$

Equation (3.16) describes the magnitude and phase of the output signal at the frequency ω_1 as a function of various device parameters and the signal frequency ω_1 . It is seen that $\underline{P}_1(\omega_1)$ also exhibits a low-pass characteristic.

The frequency response (in terms of magnitude and phase at the frequency ω_1) of the E/O conversion is defined as [64]

$$\underline{H}_1(\omega_1) = \frac{\underline{P}_1(\omega_1)}{\underline{I}_1(\omega_1)}. \quad (3.17)$$

With Eq. (3.16), this gives a frequency response of the LED's E/O conversion of

$$\underline{H}_1(\omega_1) = \frac{\underline{P}_1(\omega_1)}{\underline{I}_1(\omega_1)} = \frac{A_P}{qV_{\text{active}}B} \cdot \frac{1}{j\frac{\omega_1}{2BN_0} + 1}, \quad (3.18)$$

3. Verification of the Carrier Density Rate Equation Model

or normalized to 0 dB

$$\underline{H}_{1,\text{norm}}(\omega_1) = \frac{H_1(\omega_1)}{H_1(0)} = \frac{1}{j\frac{\omega_1}{2BN_0} + 1}. \quad (3.19)$$

Equation (3.18) is a 1st-order lowpass with a -3dB cutoff frequency of

$$\omega_c = 2BN_0 \quad \text{or} \quad f_c = \frac{\omega_c}{2\pi} = \frac{BN_0}{\pi}. \quad (3.20)$$

That is, the simplified LED model introduced in Ch. 2.7 predicts that the LED exhibits a 1st-order lowpass characteristic whose cutoff frequency increases with the input bias current I_0 according to

$$\begin{aligned} f_c &= \frac{BN_0}{\pi} \\ &\dots \text{ with Eq. (3.13)} \dots \\ &= \frac{B}{\pi} \cdot \sqrt{\frac{I_0}{qV_{\text{active}}B}} \\ &= \frac{1}{\pi} \cdot \sqrt{\frac{I_0B}{qV_{\text{active}}}}. \end{aligned} \quad (3.21)$$

For the two investigated bias values of $I_0 = 20 \text{ mA}$ and 25 mA and the device parameters of Table 3.1 on page 46, Eq. (3.21) predicts

$$f_{c,20\text{mA}} \approx 20 \text{ MHz} \quad f_{c,25\text{mA}} \approx 22.4 \text{ MHz}. \quad (3.22)$$

This is in very good agreement with the simulated values of Table 3.4. It should be noted that the numerical simulation is performed in the time domain with a subsequent discrete fourier transform (DFT) which introduces slight inaccuracies in the frequency domain (due to DFT leakage).

Equation (3.21) may be used for a parameter fit between the measured frequency responses and the simulation model. Putting the measured cutoff frequencies of Table 3.5 on page 52 into Eq. (3.21) and using V_{active} from Table 3.1, the fitted recombination coefficients are found as given in Table 3.6.

Table 3.6.: Fitted recombination coefficients of the two LEDs.

	L8045	SFH757V
B in cm^3/s	$8.47 \cdot 10^{-11}$	$7.3 \cdot 10^{-11}$
I_0 in mA	20	25

These values are well within typical ranges for B found in the literature (cf. Table 3.1 on page 46). Hence, the LED device model presented in Ch. 2.7 along with the analytical derivation of the frequency response given by Eqs. (3.19) and (3.21) can be considered an accurate description of real communication LED's frequency responses.

3.2.2. Small-Signal Frequency Response at Varying Bias

So far, the device model was verified using two different commercial communication LEDs, but investigating only one input bias point. In order to present a more universal validation, the model shall further be verified at varying input bias currents. Special attention is here paid to the potential impact of a nonconstant radiative recombination coefficient $B(T, n)$, as discussed in Ch. 2.7.

The simplified carrier density rate equation model predicts a lowpass frequency response whose -3 dB cutoff frequency f_c scales with with input bias as $f_c \propto \sqrt{I_0}$. This phenomenon shall be exemplarily verified for commercial communication LEDs with detailed measurements of model L8045. For that, the simulation model now uses the estimated recombination coefficient of

$$B_{L8045}(I_0 = 20 \text{ mA}) = 8.47 \cdot 10^{-11} \frac{\text{cm}^3}{\text{s}}.$$

A small-signal modulation is approximated by reducing the modulation amplitude by a factor of two, compared to the large-signal modulation. The reduced modulation amplitude is approximately 18 mA (peak-to-peak), which allows a minimum bias current of 10 mA with a modulation index of $m = 0.9$.

The investigated LED is specified up to 40 mA; to verify the model's validity within the entire driving range of the real LED, the investigations are performed at input bias currents up to 45 mA in steps of 5 mA. The corresponding peak-to-peak amplitude ranges used in both simulations and measurements are illustrated as vertical bars in Fig. 3.8. As can be seen, for $I_0 \geq 40$ mA, the LED is already driven well beyond its specifications.

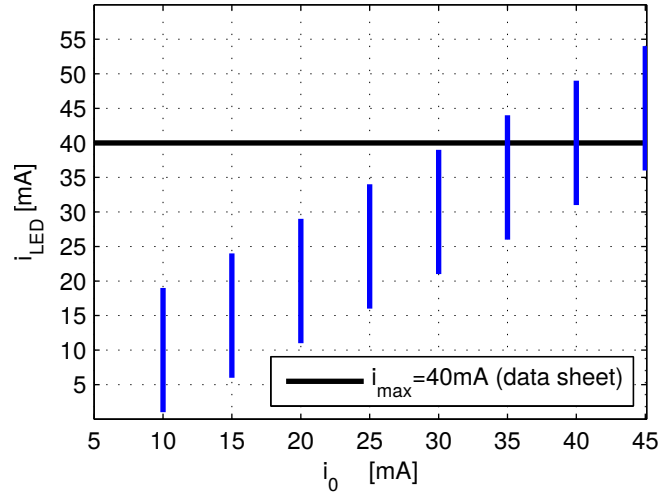


Figure 3.8.: Verification of the LED device model at different input bias currents: Realized amplitude ranges in the simulations and measurements.

3. Verification of the Carrier Density Rate Equation Model

Carrier Density Rate Equation Model

The simulated frequency responses for the different input bias values are shown in Fig. 3.9a. A 1st-order lowpass characteristic is observed at all bias values. Figure 3.9b shows the extracted -3dB cutoff frequencies versus input bias current, as well as the analytical calculation of Eq. (3.21). It is seen that the numerically simulated lowpass characteristic follow precisely the one predicted by Eqs. (3.19) and (3.21).

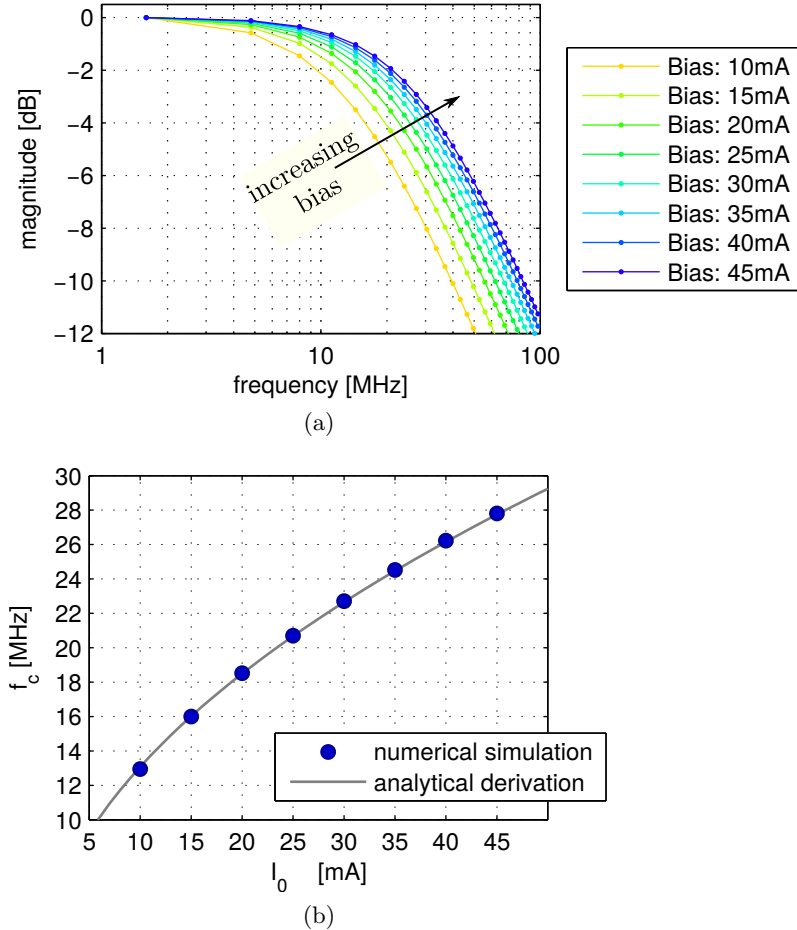


Figure 3.9.: (a) Simulated frequency responses for input bias currents between 10 mA and 45 mA. (b) Extracted -3dB cutoff frequencies versus input bias.

Measurements

It shall now be investigated whether the bias-dependent characteristics observed in Fig. 3.9 are also found in the measured frequency responses of the real communication LED. The measured frequency responses for the different input bias currents using the lab setup of Fig. 3.6 on page 52 are shown in Fig. 3.10a. Again, a lowpass characteristic is observed for all bias values, where the cutoff frequency monotonically increases with input bias. The slope can be read to be about 20 dB/decade, showing that at all bias values, the frequency response is well approximated by a 1st-order lowpass.

The -3dB cutoff frequencies extracted from the measured curves of Fig. 3.10a are shown in Fig. 3.10b, again along with $f_c(I_0)$, as predicted by Eq. (3.21). Comparison of the measured cutoff frequencies and the curve predicted by Eq. (3.21) reveals that the trend of an f_c which increases monotonically with I_0 is confirmed by the measurements. However, it becomes apparent that Eq. (3.21) clearly overestimates the bandwidth increase caused by an increasing input bias current. Possible origins of this discrepancy between the simplified device model of Eqs. (2.70) and (2.71) and the measurement results are discussed in the following.

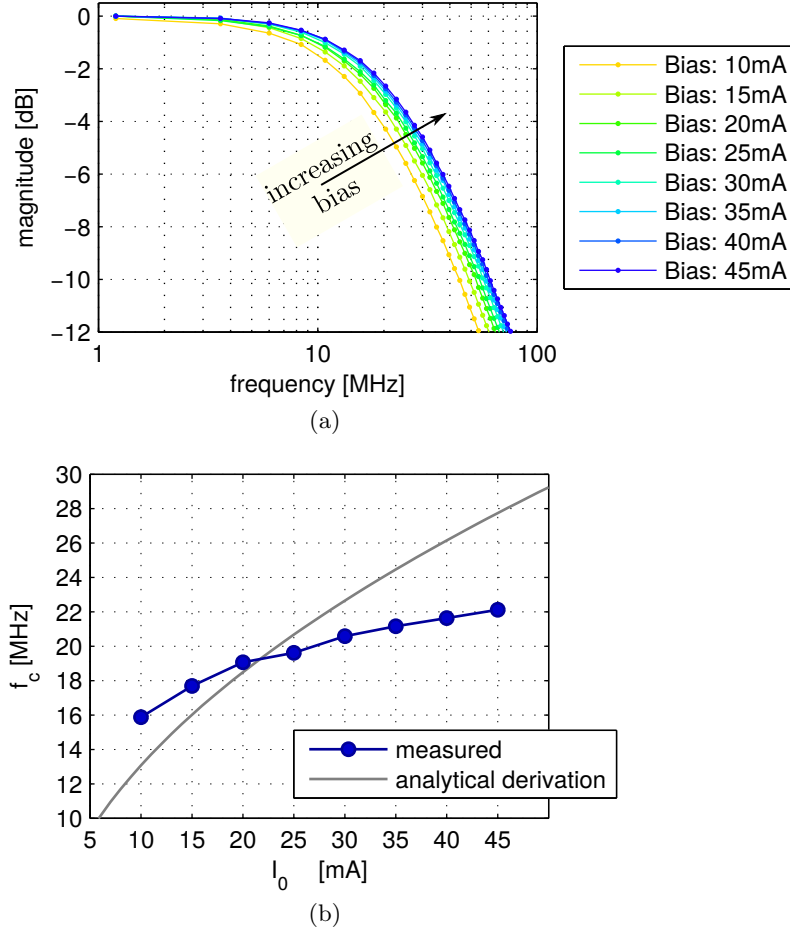


Figure 3.10.: (a) Measured frequency responses for input bias currents between 10 mA and 45 mA. (b) Extracted -3dB cutoff frequencies versus input bias.

Equation (3.21) may be solved for B , which yields

$$B(I_0, f_c) = \frac{(\pi f_c)^2 q V_{\text{active}}}{I_0}. \quad (3.23)$$

Putting the measured values of I_0 and $f_c(I_0)$ from Fig. 3.10b into Eq. (3.23) gives the extracted radiative recombination coefficient B versus input bias current, as shown in Fig. 3.11.

The resulting radiative recombination coefficient monotonically decreases with increasing bias current. Within the investigated input bias current range B decreases by

3. Verification of the Carrier Density Rate Equation Model

about 50%. That is, if the analytical model of Eq. (3.18) on page 55 is extended with the appropriate $B(I_0)$, instead of a constant B , the model may, in principle, be used to predict the frequency response of the LED at arbitrary input bias currents, provided the LED is driven within its specifications.

In the following, potential origins of such a nonconstant B shall be identified and it shall be evaluated whether the calculated drop of $B(I_0)$ of about 50% is a realistic scenario.

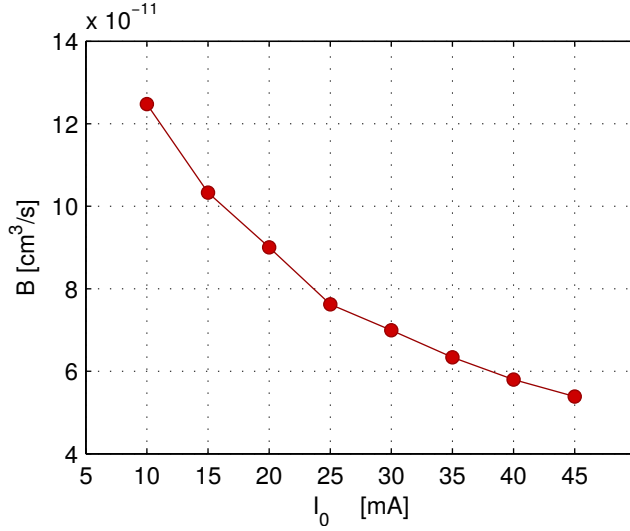


Figure 3.11.: Radiative recombination coefficient versus input bias current derived from the measurements of Fig. 3.10b using Eq. (3.23).

3.2.3. The Bias-Dependence of the Radiative Recombination Coefficient

As pointed out in Ch. 2, radiative recombination obeys the k -selection rule. Both, an increasing junction temperature T , as well as an increasing carrier density n cause the distributions of electrons and holes versus energy in the semiconductor to be spread over an increasing range ΔE . Taking into consideration the dispersion relation of Eq. (2.8) on page 21, this causes an increasing spread of carriers in the k -space, and hence, the carrier density per dk interval is expected to decrease with both T and n . This is a well-known effect (see for example [47, 51]), and is therefore the most prominent potential origin of the observed drop of $B(I_0)$.

As discussed in Ch. 2.7, the LED device model used in this thesis can only be extended to account for $B(T)$. However, based on the device simulation results and values found in the literature, some estimations on the potential impact of both $B(T)$ and $B(n)$ are presented in the following to estimate whether the observed drop of $B(I_0)$ may indeed be attributed to the temperature T .

To account for $B(T)$ and $B(n)$, knowledge of the temperature T and carrier density n is required. The carrier density established in the device is simulated with Eq. (2.70) on page 43, and hence this quantity is readily available. The junction temperature T however, can only be roughly estimated.

The Impact of the Junction Temperature

Measurements of different types of LEDs showed that T scales in good approximation linearly with the LED input bias current [34]. The measured slopes were approximately between 0.9 and 1.3 K/mA. For the investigated input bias range between 10 mA and 45 mA, this results in an expected increase of temperature of roughly about $\Delta T = 40$ K.

The temperature dependence of B was for example studied in [51]. Therein, $B(T)$ was investigated for GaAs/AlGaAs QWs both theoretically and experimentally. The simplified theoretical model predicted a negligible impact of temperature at values below approximately 50 K and predicted for $T > 100$ K that the radiative recombination coefficient scales as $B \propto 1/T$. This model was compared with measurements at various temperatures with a fixed bias current density. Although the two temperature regimes predicted by the model were also found in the experiments, it was observed that the actual drop of $B(T)$ is far more severe for $T > 100$ K than theoretically predicted. For temperatures between about 160 K and 270 K, the measured recombination coefficient scaled approximately as $B(T) \propto 1/T^{1.5}$ and for temperatures between about 270 K and 300 K, the measured recombination coefficient scaled approximately as $B(T) \propto 1/T^3$. Extrapolating this trend to temperatures beyond² 300 K suggests even steeper slopes. The resulting relative drop for different scaling scenarios of B is shown in Fig. 3.12. It is seen that an increase of temperature by 40 K is expected to cause a reduction of B by about 30 to 40 %.

These values confirm the trend found with measurements reported in [65]. Therein, an InGaAs/InGaAsP QW laser below threshold was investigated. For a temperature increase of only 30 K, a relative decrease of B of 40 % was observed.

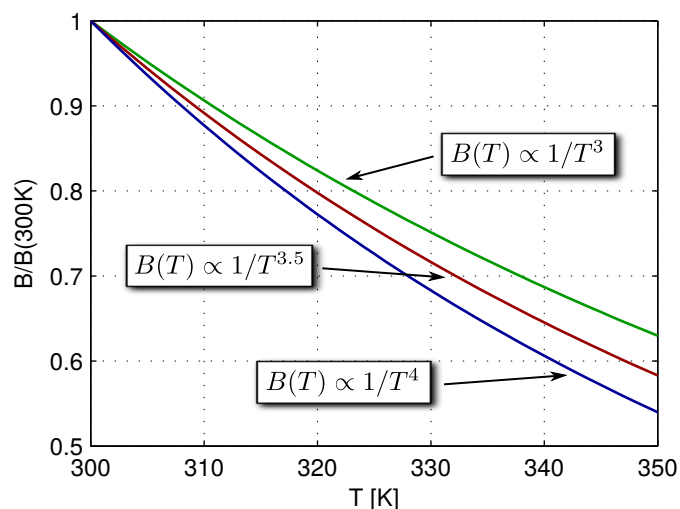


Figure 3.12.: The potential impact of the junction temperature on the radiative recombination coefficient, as extrapolated from the measurement results in [51].

²The measurements of this work were performed at room temperature.

The Impact of the Carrier Density

The impact of the carrier density n on the radiative recombination coefficient B is the subject of research activities for decades. Different analytic models were developed to predict the drop of $B(n)$. For the results of this work, the region of interest is about $4.5 \cdot 10^{17} \leq n \leq 9.5 \cdot 10^{17} \text{ cm}^3/\text{s}$ (cf. Fig. 3.2 on page 48).

A simple model which takes into account k -selection in parabolic bands [47] predicts for this carrier density range a relatively moderate drop of $B(n)$ of about 7%. A more sophisticated model by Stern [53] which takes into account band tail effects predicts a drop of $B(n)$ of about 13%. In [47] measurements were carried out on AlGaAs and InGaAsP LEDs and lasers. Based on these measurement results, the authors suggested a simplified model of the form

$$B(n) = B_0 - B_1 n, \quad (3.24)$$

where the ratios B_1/B_0 were found to be between $1.1 \cdot 10^{-19} \text{ cm}^3$ and $2.9 \cdot 10^{-19} \text{ cm}^3$. For the region of interest, this corresponds to a drop of $B(n)$ between about 6% and 17%, as depicted in Fig. 3.13. In a more recent publication however, measurements on InGaAs/InGaAsP devices showed a much stronger decrease of $B(n)$ of about 25% [65].

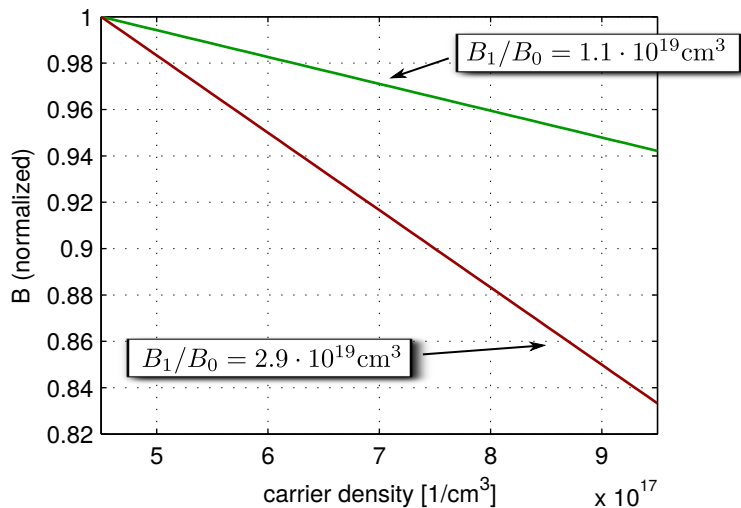


Figure 3.13.: The potential impact of the carrier density on the radiative recombination coefficient, as fitted from the measurement results in [47].

It is generally found that simple analytic models tend to underestimate the impact of both T and n on B . Measurements found in several publications show a clear decreasing radiative recombination coefficient B with both junction temperature T and carrier density n . The observed impact, however, varies significantly, depending on the semiconductor and device structure. Assuming, for the sake of simplicity, some mean values for both $B(T)$ and $B(n)$, the impact of temperature is expected to clearly dominate with a relative decrease of $B(I_0)$ of larger than 40% and the impact of the increasing carrier density is about 10 to 15%. Assuming further the two factors are independent of each other and effectively multiply, a decrease of $B(I_0)$ of about 50% in the range of $10 \text{ mA} \leq I_0 \leq 45 \text{ mA}$ could easily be reached, which is about the same range found in this work and shown Fig. 3.11.

3.2.4. Summary

The simplified LED device model was verified in terms of the frequency response of the E/O conversion. Using commonly used device parameters found in the literature, the model predicts a 1st-order lowpass behaviour with a cutoff frequency of about 20 MHz. This characteristic is in very good agreement with measurements of commercial communication LEDs.

An analytical derivation was presented which predicts the frequency response as a 1st-order lowpass function whose cutoff frequency scales with the electrical input bias current as $f_c \propto \sqrt{I_0}$. A verification with measurements at varying bias currents showed indeed an f_c which monotonically increases with I_0 . It was found, however, that the relation of $f_c \propto \sqrt{I_0}$ overestimates the true increase of $f_c(I_0)$.

It was discussed that a nonconstant radiative recombination coefficient $B(I_0)$ may be incorporated into the device model in order to be able to describe the measured $f_c(I_0)$. Based on values found in the literature, it was derived that when the LED is biased at the upper end of its specification a relative decrease of $B(I_0)$ (caused predominantly by an increased junction temperature) of about 50 % is realistic. With such a decreasing $B(I_0)$, the device model may also be applied for varying input bias currents. When used as an optical transmitter, however, the LED is always biased at a fixed value, typically at about $I_{\max}/2$.

3.3. Higher-Order Harmonics due to Nonlinearities

Linear systems are fully described by their frequency response. But it is well known that LEDs exhibit nonlinear characteristics and as a result the LED cannot be accurately described by its linear frequency response only. The device model with the frequency response of Eq. (3.18) must therefore be extended to incorporate also the nonlinear portion of the E/O conversion.

When a nonlinear system is driven with a sinusoidal input signal, higher-order harmonics are generated at its output at frequencies which are an integer multiple of the input frequency. This is easily verified when a nonlinear function $f(x)$ is expanded at $x = 0$ into a Taylor series as

$$f(x) = \sum_{n=0}^{\infty} \frac{f^{(n)}(0)}{n!} x^n = f(0) + f'(0)x + \frac{f''(0)}{2}x^2 + \frac{f'''(0)}{6}x^3 + \dots, \quad (3.25)$$

with $f^{(n)}$ being the n^{th} derivative of $f(x)$. For a sinusoidal input signal $x = \cos(2\pi ft)$, the output therefore exhibits terms of the form $[\cos(2\pi ft)]^n$. With the trigonometric identities it is seen that these terms produce a series of output harmonics whose frequencies are integer multiples of the input frequency, for example

$$[\cos(2\pi ft)]^2 = \frac{1}{2} [1 + \cos(2 \cdot 2\pi ft)] \quad (3.26)$$

$$[\cos(2\pi ft)]^3 = \frac{1}{4} [3 \cos(2\pi ft) + \cos(3 \cdot 2\pi ft)] \quad (3.27)$$

$$[\cos(2\pi ft)]^4 = \frac{1}{8} [3 + 4 \cos(2 \cdot 2\pi ft) + \cos(4 \cdot 2\pi ft)]. \quad (3.28)$$

The magnitudes of these terms are independent of the signal's frequency, this is also referred to as a static nonlinearity. The n^{th} power of $\cos(2\pi ft)$ produces output harmonics at frequencies $f_{\text{out}} \leq n \cdot f$. As a result, when the LED is modulated with a biased onetone signal, an output spectrum as depicted in Fig. 3.14 is to be expected. The output spectrum contains the carrier signal (whose level is governed by the linear frequency response) and a (possibly infinite) number of higher-order harmonics whose levels are typically measured in dBc (dB level relative to the carrier level).

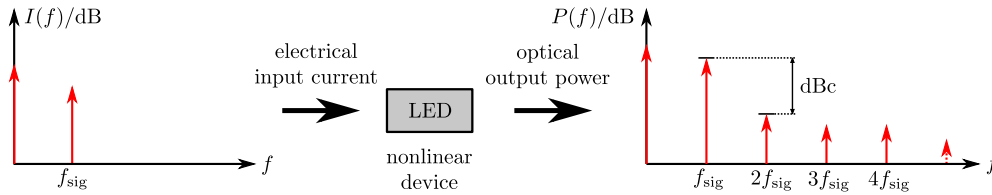


Figure 3.14.: Higher-order harmonics at the output of the LED when the LED is modulated with a biased onetone signal of frequency f_{sig} : Frequency domain representation with the definition of the relative level in dBc.

Higher-order terms (large n in Eq. (3.25)) do also contribute to lower-order harmonics (for example the 2nd harmonic), but due to the factor of $1/n!$ in the Taylor series expansion, it is usually assumed that for a given f_{out} lower-order terms are the dominant source.

3.3. Higher-Order Harmonics due to Nonlinearities

An exact mathematical description of the nonlinear process would usually require the consideration of an infinite number of tones. The aim in this context is to derive a simplified mathematical closed-form description of the dominant terms of the nonlinearities originated in a communication LED, which is based on the physical device model of Ch. 2.7. For this, the nonlinear behaviour of the device model will be compared with measurements of the two commercial devices.

In a first step, the accuracy of the carrier density rate equation model will be evaluated by means of higher-order harmonics for a biased onetone excitation of the LED. Motivated by these results, a generalized investigation of 2nd-order intermodulation products (IM2) occurring for a biased twotone excitation with varying input frequencies will then be conducted in Ch. 3.4. After a detailed validation of the IM2 with measurements, a simplified closed-form expression of the IM2 will be derived in Ch. 4.

3.3.1. Large-Signal Modulation

Higher-order harmonics up to the 4th-order are investigated for large-signal modulation. The measurements are performed using the FSO setup of Fig. 3.6 on page 52. The bias current and modulation amplitude are again set according to Table 3.3 on page 50. The carrier density rate equation model

$$\frac{dn(t)}{dt} = \frac{i_{\text{LED}}(t)}{qV_{\text{active}}} - B [n(t)]^2,$$

$$p_{\text{opt}}(t) = \eta_{\text{extraction}} E_{\text{ph}} V_{\text{active}} B \cdot [n(t)]^2$$

uses the device parameters given in Table 3.7. The two different values for the recombination coefficient B are the fitted recombination coefficients given on page 56.

Table 3.7.: LED device parameters used in the simplified carrier density rate equation model.

symbol	unit	value
B	cm^3/s	$8.47 \cdot 10^{-11}$ and $7.3 \cdot 10^{-11}$
A_{active}	μm^2	280^2
N_{QW}	dimensionless	8
W_{QW}	nm	5
η_{int}	dimensionless	100 %
$\eta_{\text{extraction}}$	dimensionless	2.5 %

The results of the measurements and numerical simulations are shown in Fig. 3.15 for both devices, where HD n denotes the n^{th} harmonic (“Harmonic Distortion”). The sensitivity of the measurement setup is limited by noise and the vertical resolution of the receiving analog-to-digital converter (ADC). A rough worst-case estimate of

3. Verification of the Carrier Density Rate Equation Model

the limitations due to the ADC resolution (neglecting any signal statistics) is given by the gray-shaded area in Fig. 3.15. That is, measured signal levels in that area are potentially prone to uncertainties due to an increased quantization noise.

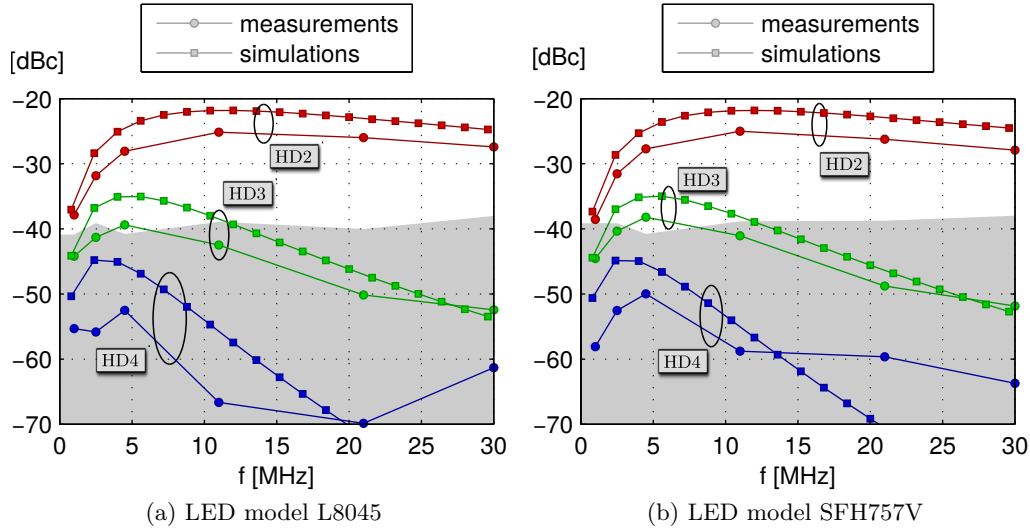


Figure 3.15.: Higher-order harmonics at the output of the communication LEDs: Measurements and simulations (bias and modulation amplitudes set according to Table 3.3 on page 50).

Several important characteristics can be read from Fig. 3.15:

1. The measurement results of the two devices reveal that both devices exhibit virtually the same nonlinear characteristic.
2. For both measurements and numerical simulations of the carrier density rate equation, the 2nd-order nonlinearity clearly dominates over the 3rd-order by at least 10 dB and over the 4th-order by at least 20 dB.
3. The output levels of the higher-order harmonics are strongly frequency dependent with a deterministic behaviour. For an input frequency of about 1 MHz, the HD2 is at about -40 dBc, for frequencies up to 10 MHz, the measured HD2 increases with frequency to about -25 dBc. For a further increase of the input frequency, the output HD2 tends to drop again. A similar behaviour is observed for HD3 and HD4.
4. The measured characteristics of the frequency dependence is well predicted by the carrier density rate equation model, even for HD3 and partly HD4, where the latter is most likely prone to uncertainties caused by noise and a limited vertical resolution of the receiver.
5. The simulation model slightly overestimates the higher-order harmonics, which for HD2 is an approximately constant factor of 3 dB. This is a remarkable accuracy, since the amplitude of HD n scales with the n^{th} power of the signal amplitude, cf. Eq. (3.25). That is, this accuracy of the 2nd-order harmonic power level is

basically equivalent to an accuracy of 1.5 dB signal power level. As a potential origin of this overestimation of the HD x , an extended device model which includes the effects of doping of the active zone is discussed in Appendix A on page 119ff.

3.3.2. Summary

Both investigated LEDs show similar characteristics of higher-order harmonics up to the order 4. The observed frequency dependence can be roughly characterized by a bandpass behaviour with its maximum around 10 MHz, i.e. at approximately $f_c/2$. The fact that both devices behave nearly identically indicates that the observed nonlinear processes are insensitive to slight variations of the device structure or driving scenario.

Numerical simulations of the simplified LED model introduced in Ch. 2.7 agree fairly well with the measurement results, even for HD3 and HD4. This demonstrates that the simple carrier density rate equation model is indeed suitable to model a communication LED's linear and nonlinear E/O conversion in a communication context.

It is found that the 2nd-order nonlinearity clearly dominates over higher-order terms. This suggests that a simplified closed-form analytic description of the nonlinear part of the E/O conversion of the LED may be restricted to the 2nd-order term. In the following, a thorough investigation of the frequency dependence of the 2nd-order nonlinearity is therefore conducted with both measurements and numerical simulations of the carrier density rate equation model.

3.4. The Frequency Dependence of 2nd-order Nonlinearities

A generally valid characterization of the frequency response of 2nd-order nonlinearities requires the evaluation of 2nd-order intermodulation products (IM2) for a twotone excitation with varying input frequencies f_1, f_2 .

With the identity

$$\cos(2\pi ft) = \frac{\exp(j2\pi ft) + \exp(-j2\pi ft)}{2} \quad (3.29)$$

it is easily seen that when a twotone signal with two different frequencies passes a 2nd-order nonlinearity as $[\cos(2\pi f_1 t) + \cos(2\pi f_2 t)]^2$, intermodulation products at $f_2 + f_1$ and $f_2 - f_1$ are generated. This is illustrated in Fig. 3.16 by considering the double-sided spectrum of the signals. The onetone excitation used in the previous section may be interpreted as the special case of a twotone excitation with $f_1 = f_2$.

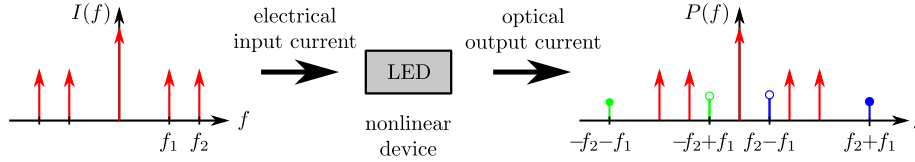


Figure 3.16.: 2nd-order intermodulation products (IM2) of a biased twotone excitation.

To measure or simulate the frequency response of the 2nd-order intermodulation product (IM2), a frequency range of interest $[f_{\min}, f_{\max}]$ and a frequency spacing Δf must be specified. For a baseband frequency range $[0, f_{\max}]$, this results in a frequency grid to be processed, as depicted in Fig. 3.17. Obviously, the two frequencies in the biased twotone signal

$$i(t) = i_0 + \hat{i} \cos(2\pi f_1 t) + \hat{i} \cos(2\pi f_2 t) \quad (3.30)$$

are interchangeable when both tones exhibit the same modulation amplitude \hat{i} . As a result, only one half (including the diagonal of $f_2 = f_1$) of the grid must actually be processed, as indicated by the black dots in Fig. 3.17.

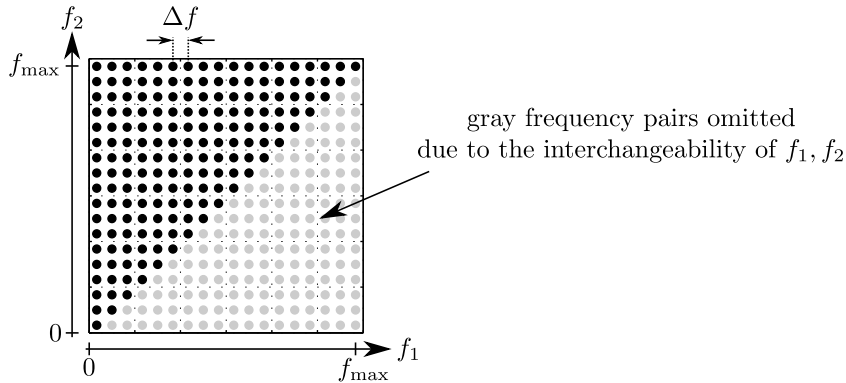


Figure 3.17.: The grid of frequency pairs $[f_1, f_2]$ which is processed for the measurement and simulation of the frequency dependence of the LED's 2nd-order nonlinearity.

3.4. The Frequency Dependence of 2nd-order Nonlinearities

For each frequency pair, the magnitudes at $f_2 + f_1$ and at $f_2 - f_1$ are determined. Since there are two input variables (f_1 and f_2), a matrix-like alignment of the IM2 is convenient.

Throughout this thesis, a matrix representation of the IM2 as depicted in Fig. 3.18 (right) will be used.

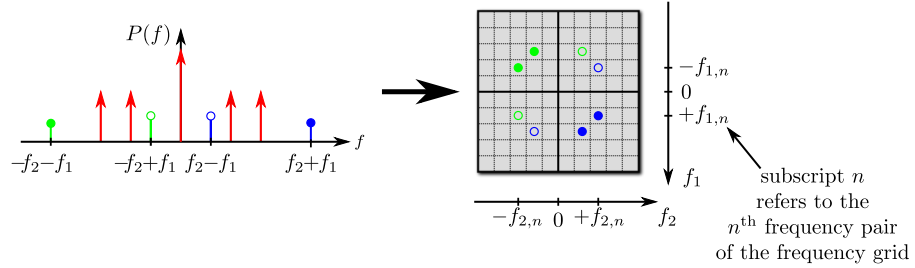


Figure 3.18.: The matrix representation of the IM2 used in this thesis.

For each input frequency pair $[f_1, f_2]$, the IM2 magnitudes are written in the matrix, where the x and y coordinates are given by f_1 and f_2 . All intermodulation frequencies are interpreted as the sum of the two input frequencies. Intermodulation products lying at a difference frequency (such as $f_{\text{IM}} = f_2 - f_1$) are interpreted as the sum of a positive and a negative input frequency (cf. the double-sided spectrum of Fig. 3.18). That is, negative input frequencies are incorporated in the matrix representation. For a given input frequency pair $[f_1, f_2]$, the two intermodulation products $f_{\text{IM, sum}} = |f_1| + |f_2|$ and $f_{\text{IM, difference}} = |f_1| - |f_2|$ are found in the two triangular regions marked in Fig. 3.19.

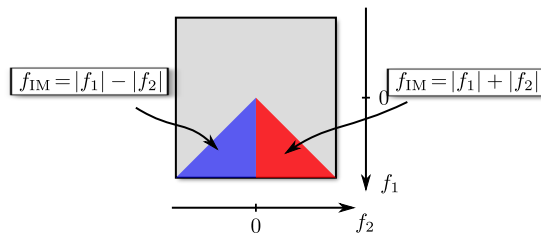


Figure 3.19.: Locations of the two intermodulation products within the matrix representation of the IM2.

The whole matrix is a representation of the double-sided spectrum of the IM2 harmonics. However, only magnitudes will be evaluated, due to the fact that the lab setup cannot accurately extract the phase. As a result, the upper left half of the matrix, which contains the negative IM2 frequencies is basically redundant³. The symmetry resulting from this redundancy is sketched in Fig. 3.20 (left).

Further, as pointed out with Eq. (3.30), the two input tones are interchangeable when their amplitudes are equal. This introduces another redundancy in the matrix, with its corresponding symmetry axis as sketched in Fig. 3.20 (right).

³The negative side of the double-sided Fourier spectrum of a real-valued signal is the complex conjugate of the positive side of the spectrum.

3. Verification of the Carrier Density Rate Equation Model

For the sake of completeness, however, all of these redundant IM2 values are written into the matrix. The motivation for the use of this complete matrix representation is that it is directly compatible with system-theoretic descriptions, which will be introduced in Ch. 4.

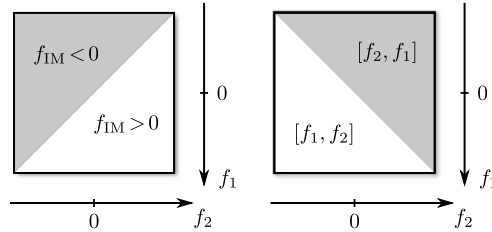


Figure 3.20.: Symmetries found in the IM2 matrix due to the inclusion of negative frequencies (left) and the interchangeability of f_1 and f_2 (right).

Some important additional characteristics of this representation are shown in Fig. 3.21. Diagonals from the lower left to the upper right side represent a constant intermodulation frequency for varying input frequencies, as shown in Fig. 3.21 (left). The diagonal from the upper left to the lower right side shows the IM2 at $f_1 + f_2$ for $f_2 = f_1$, cf. Fig. 3.21 (right).

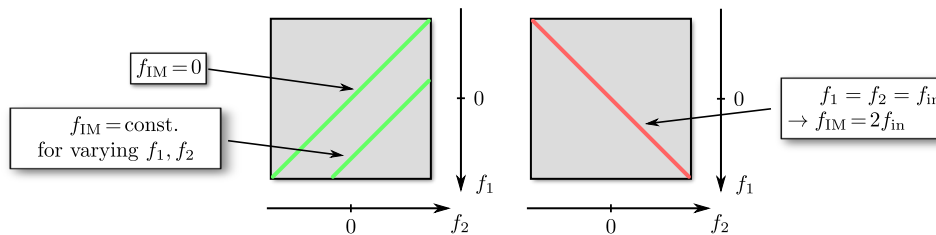


Figure 3.21.: General characteristics found in the matrix representation of the IM2.

The phase of the frequency-dependent intermodulation products is not considered; the IM2 are characterized by their magnitudes in a dB scale. However, in contrast to the evaluation of the higher-order harmonics presented in the previous section, the frequency-dependent IM2 will not be evaluated in dBc, but in a dB scale normalized to the respective maximum. That is, a normalization as used for the linear frequency responses of Fig. 3.5 on page 51 will be used. The motivation is as follows. The dBc scale always incorporates the magnitude response of both the signal itself and of the IM2. But the aim is to identify the characteristics of the IM2, so any impact of the linear response $\underline{H}(f)$ shall be eliminated in the investigations.

3.4.1. Large-Signal Modulation

The processing of the frequency grid presented in Fig. 3.17 is a time consuming procedure, for both numerical simulations and lab measurements. The frequency range and frequency spacing must therefore be carefully chosen to cover the part of the IM2 spectrum which is of most interest for communication purposes. In the following investigations, input frequencies up to slightly above the -3dB cutoff frequencies are chosen, since usually most of the transmit signal's energy is located in that region.

The IM2 of the LEDs are evaluated for frequencies up to about 25 MHz, and a frequency spacing of $\Delta f = 1.6\text{ MHz}$ is used (cf. Fig. 3.17). The input signal is a twotone signal, as given by Eq. (3.30), where the bias current is set according to Table 3.3 on page 50. The modulation amplitudes \hat{i} of both tones are set to an equal value, so that the peak-to-peak modulation amplitudes of 36 mA and 45 mA (as given in Table 3.3 on page 50) are obtained.

Carrier Density Rate Equation Model

The simulation model uses the device parameters of Table 3.1 on page 46, again with the fitted recombination coefficients of Table 3.6 on page 56. Figure 3.22 shows the simulation results for both devices. The IM2 magnitudes are shown in false color image plots, where both plots are scaled to the same magnitude range, that is, same colors map to the same dB values.

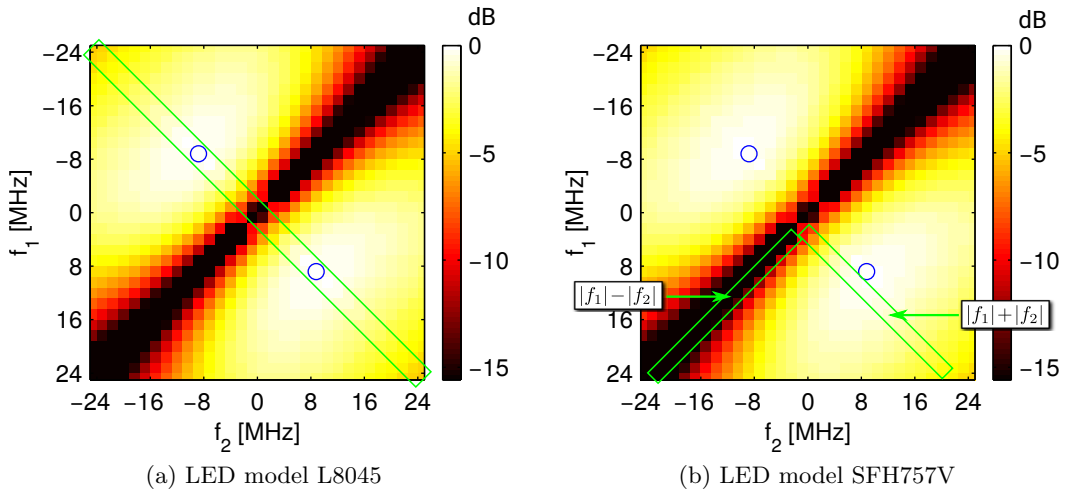


Figure 3.22.: Simulated IM2 magnitudes (normalized) for a twotone signal with varying input frequencies $[f_1, f_2]$ (circles: 0 dB).

It is seen that the simulation of the two devices results in virtually the same frequency-dependence of the IM2. The IM2 magnitudes are strongly frequency-dependent with changes in magnitude of more than 15 dB. Such a behaviour is also referred to as *dynamic nonlinearities*. The maximum IM2 magnitudes (blue circles) are found when the two input frequencies are at $f_1 = f_2 = 8.8\text{ MHz}$, i.e. at approximately $f_c/2$.

The diagonal marked green in Fig. 3.22a corresponds to the intermodulation mag-

3. Verification of the Carrier Density Rate Equation Model

itudes for $f_1 = f_2^4$. This basically corresponds to the HD2 of a onetone excitation. Considering only the positive frequencies⁵, the diagonal shows a passband characteristic with vanishing IM2 magnitudes for low input frequencies $[f_1, f_2]$, a maximum for $f_1 = f_2 \approx f_c/2$, and a moderate decrease for input frequencies beyond $f_c/2$. This is in agreement with the HD2 characteristics found for the onetone excitation of Fig. 3.15 on page 66.

In Fig. 3.22b, the IM2 for closely spaced input frequencies are marked (i.e. $f_2 \approx f_1$). It is seen that the magnitude at $|f_1| + |f_2|$ exhibits the above mentioned passband characteristic, whereas the magnitudes at $|f_1| - |f_2|$ tend to vanish, independent of the input frequencies. That is, the simulation model predicts strongly unequal magnitudes at $f_{\text{IM, pos}} = |f_1| + |f_2|$ and $f_{\text{IM, neg}} = |f_1| - |f_2|$.

Measurements

The 2nd-order intermodulation products (IM2) are measured with the lab setup of Fig. 3.6 on page 52. The results for the two commercial communication LEDs are shown in Fig. 3.23 in a normalized dB scale. The plots are scaled to the same dB range as used for the simulated results of Fig. 3.22 to allow a direct comparison by the colors.

The measured IM2 responses of the two LEDs are virtually identical and resemble those simulated by the carrier density rate equation model. For both devices, the IM2 response shows a passband characteristic with its peak IM2 for input frequencies around 9 – 10 MHz, i.e. again at around $f_c/2$. For further increasing input frequencies up to about 25 MHz, the IM2 drops by about 5 dB. Again, as found in the simulations, low intermodulation frequencies are suppressed by around 15 dB compared to the maximum IM2 levels.

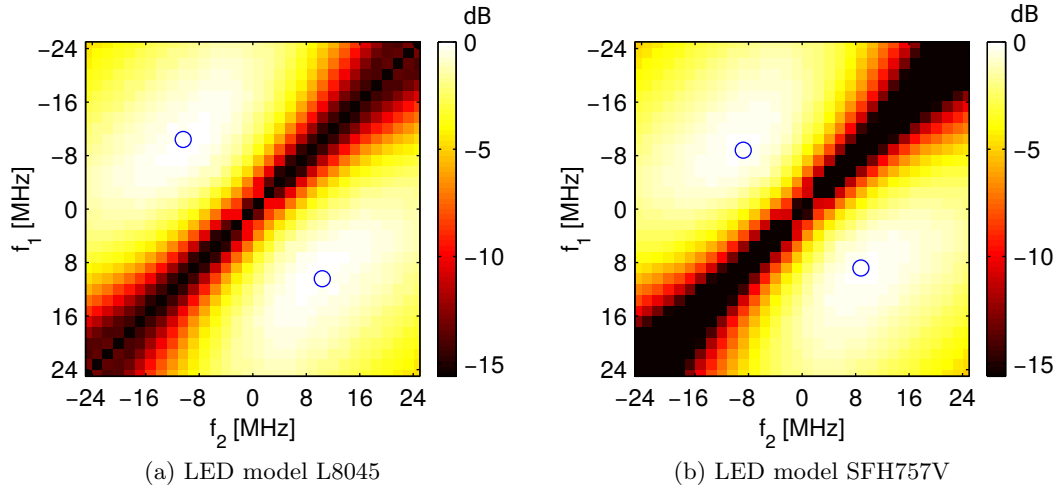


Figure 3.23.: Measured IM2 magnitudes (normalized) for a twotone signal with varying input frequencies $[f_1, f_2]$ (circles: 0 dB).

⁴The upper left end of the diagonal corresponds to the intermodulation product at -48 MHz, the lower right end of the diagonal corresponds to the intermodulation product at $+48$ MHz.

⁵The values at the negative frequencies are redundant, as discussed earlier.

3.5. Summary

The simplified LED model presented in Ch. 2.7 based on a carrier density rate equation was verified against lab measurements of commercially available communication LEDs.

Using numerical simulations, the model was verified in a first step in terms of its static P-versus-I characteristic, its linear frequency response $|H(f)|$, and higher-order harmonics for a onetone excitation. For all these characterizations, good agreement between simulations and measurements was obtained. The simulation model predicts a linear static P-I curve, which was also found for the two LEDs under investigation. The frequency response was found to resemble a 1st-order lowpass characteristic in both numerical simulations and lab measurements. With the electrical input bias current set to half the maximum rated input DC current, the -3 dB cutoff frequency was found to be approximately 20 MHz, for both devices and the simulations.

An analytic small-signal approximation for $H(f)$ was derived to be a 1st-order low-pass, whose cutoff frequency scales with the input bias current as $f_c \propto \sqrt{I_0}$. This behaviour was also found in the numerical simulations of the carrier density rate equation.

The measurements showed also a cutoff frequency which monotonically increases with input bias. However, the relative increase in the investigated range between 10 mA and 45 mA turned out to be only about 60 % of that predicted by the analytic formula. This discrepancy could be explained by a nonconstant radiative recombination coefficient B which monotonically decreases with input bias current. Based on data found in the literature, a potential physical origin of such a bias dependence of B was identified to be an increasing device temperature. That is, a more accurate bias dependence of the model may be achieved when a reasonable approximation for $B(T)$ is included in the device model. However, it shall be emphasized that in a real communication scenario the LED is biased at a fixed value, and hence this aspect won't be much of a concern.

In a next step, the device model was verified in terms of higher-order harmonics at the LED output when the LED is modulated with a biased onetone signal. Again, good agreement between numerical simulations and measurements was obtained. The results showed that 2nd-order nonlinearities clearly dominate over the 3rd and 4th harmonics. It was further found that the IM2 exhibit a passband characteristic with the maximum magnitude at input frequencies around $f_c/2$.

Based on these results, detailed investigations were performed on the frequency dependence of the IM2 using a biased twotone excitation with varying input frequencies. The frequency dependence found in both simulations and measurements turned out to be a passband-like characteristic with vanishing IM2 levels at low frequencies.

The verification generally revealed a linear E/O conversion under DC operation, but a nonlinear E/O conversion under AC operation. These nonlinearities are inherent in the simple carrier density rate equation model. Since this model neglects any nonradiative recombination processes, it is assumed that the observed nonlinearity actually represents a lower bound of nonlinearities which is expected to be always present in an LED driven in the high-excitation regime, as is the idealized case for QW and DH devices.

In the following chapter, an analytic model which accurately describes the observed IM2 behaviour will be derived. The analytic description of these nonlinearities together with the analytic description of the linear frequency response derived in Ch. 3.2.1 then

3. *Verification of the Carrier Density Rate Equation Model*

give an analytic LED device model suitable for applications in a communication context.

4. An Analytic Model of Dynamic Nonlinearities in Directly Modulated LEDs

The well-known Taylor series expansion of a nonlinear function, as given by Eq. (3.25) on page 64 does not take into account the impact of the input signal's frequency. That is, only static nonlinearities can be modelled with a Taylor series.

A mathematical foundation to describe a dynamically (i.e. frequency-dependent) nonlinear system is given by the Volterra series, which may be interpreted as an extension of the Taylor series.

4.1. Volterra-Series Representation of the LED

The Volterra series of a time-invariant dynamic nonlinear system which maps the input signal $x(t)$ to the output signal $y(t)$ is given as [64]

$$\begin{aligned}
 y(t) = & \int_{-\infty}^{\infty} h_1(\tau_1)x(t - \tau_1)d\tau_1 \\
 & + \int_{-\infty}^{\infty} \int_{-\infty}^{\infty} h_2(\tau_1, \tau_2)x(t - \tau_1)x(t - \tau_2)d\tau_1d\tau_2 \\
 & + \int_{-\infty}^{\infty} \int_{-\infty}^{\infty} \int_{-\infty}^{\infty} h_3(\tau_1, \tau_2, \tau_3)x(t - \tau_1)x(t - \tau_2)x(t - \tau_3)d\tau_1d\tau_2d\tau_3 \\
 & + \dots
 \end{aligned} \tag{4.1}$$

The functions $h_n(\tau_1, \dots, \tau_n)$ are called the Volterra kernels of the system. It is seen that the Volterra series is basically a power series which includes memory effects. Equation (4.1) may also be written in a more compact form as

$$y(t) = \mathbf{H}_1[x(t)] + \mathbf{H}_2[x(t)] + \mathbf{H}_3[x(t)] + \dots, \tag{4.2}$$

with the n^{th} -order Volterra operator

$$\mathbf{H}_n[x(t)] = \int_{-\infty}^{\infty} \dots \int_{-\infty}^{\infty} h_n(\tau_1, \dots, \tau_n)x(t - \tau_1) \dots x(t - \tau_n)d\tau_1 \dots d\tau_n. \tag{4.3}$$

The nonlinear system described by Eq. (4.2) is represented by a block diagram as depicted in Fig. 4.1.

4. An Analytic Model of Dynamic Nonlinearities in Directly Modulated LEDs

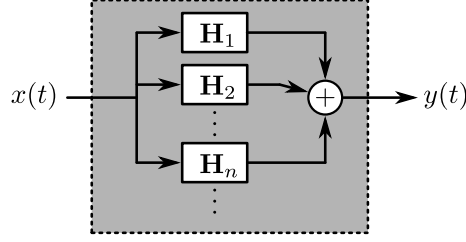


Figure 4.1.: Block diagram of a nonlinear system described by Eq. (4.2).

In the most general form of Eqs. (4.1) and (4.2), the Volterra series incorporates an infinite number of summands. But with the power series character of the Volterra series, as directly seen in Eq. (4.1) and the trigonometric identities for $\cos^n(2\pi ft)$, as introduced in Ch. 3.3, it is obvious that the IM2 of a twotone input signal of the form

$$x(t) = \cos(2\pi f_1 t) + \cos(2\pi f_2 t) \quad (4.4)$$

is expected to be mainly determined by the 2nd-order Volterra operator

$$\mathbf{H}_2[x(t)] = \int_{-\infty}^{\infty} \int_{-\infty}^{\infty} h_2(\tau_1, \tau_2) x(t - \tau_1) x(t - \tau_2) d\tau_1 d\tau_2. \quad (4.5)$$

Just as discussed for the Taylor series, higher-order ($n > 2$) Volterra operators may, in principle, also contribute to the output magnitudes at $f_{\text{IM}} = f_1 \pm f_2$. However, using measurements of various LEDs, it was found in [23], that the 2nd-order Volterra kernel $h_2(\tau_1, \tau_2)$ dominates over higher-order Volterra kernels. As a result, it is assumed that a reasonable Volterra series representation of the LED is given by the truncated Volterra series of

$$\begin{aligned} y(t) &= \int_{-\infty}^{\infty} h_1(\tau_1) x(t - \tau_1) d\tau_1 + \int_{-\infty}^{\infty} \int_{-\infty}^{\infty} h_2(\tau_1, \tau_2) x(t - \tau_1) x(t - \tau_2) d\tau_1 d\tau_2 \\ &= \mathbf{H}_1[x(t)] + \mathbf{H}_2[x(t)]. \end{aligned} \quad (4.6)$$

The corresponding block diagram is shown in Fig. 4.2. Equation (4.6) is the mathematical description of the LED's E/O conversion where, so far, the LED is treated as a black box, since $h_1(\tau_1)$ and $h_2(\tau_1, \tau_2)$ are yet unknown.

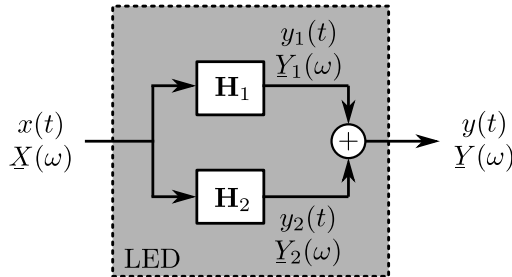


Figure 4.2.: Volterra series representation of the LED used in this work.

4.2. Frequency Domain Representation of the Nonlinear System

In the analysis of LTI systems, the frequency domain representation of the system plays an important role and the system is fully described either in the time domain by its impulse response $h(\tau)$ or in the frequency domain by its frequency response $\underline{H}(f)$.

In the following section, the frequency domain representation of the nonlinear time-invariant system of Eq. (4.6) will therefore be discussed.

4.2. Frequency Domain Representation of the Nonlinear System

4.2.1. First-Order (linear) Part

The time domain representation of the 1st-order part of the Volterra series is given as

$$y_1(t) = \int_{-\infty}^{\infty} h_1(\tau_1)x(t - \tau_1)d\tau_1 = \mathbf{H}_1[x(t)]. \quad (4.7)$$

This is a convolution integral, which is well known from the system-theoretic analysis of linear time-invariant (LTI) systems. It maps the input signal $x(t)$ to the output signal $y_1(t)$. The 1st-order Volterra kernel $h_1(\tau_1)$ is therefore equivalent to the impulse response of an LTI system.

The frequency domain representation of Eq. (4.7) is easily derived with the Fourier transform of the 1st-order Volterra kernel $h_1(\tau_1)$

$$\underline{H}_1(\omega_1) = \mathcal{F}\{h_1(\tau_1)\} = \int_{-\infty}^{\infty} h_1(\tau_1)e^{-j\omega_1\tau_1}d\tau_1, \quad (4.8)$$

which is also referred to as the 1st-order Volterra kernel transform. With the convolution theorem, $\underline{H}_1(\omega_1)$ relates the input spectrum $\underline{X}(\omega_1)$ to the output spectrum as

$$\underline{Y}_1(\omega_1) = \underline{H}_1(\omega_1)\underline{X}(\omega_1). \quad (4.9)$$

Assuming negligible impact of higher-order Volterra operators (small-signal assumption) on the output at the signal frequency $\omega_1 = 2\pi f_1$ (i.e. $\underline{Y}(\omega_1) = \underline{Y}_1(\omega_1)$), the 1st-order Volterra kernel transform may be directly measured in form of the linear frequency response $\underline{H}(\omega_1)$.

The frequency response of the LED was derived in Ch. 3.2.1 and given by Eq. (3.18) on page 55 as

$$\underline{H}_1(\omega_1) = \underline{H}(2\pi f_1) = \frac{A_P}{qV_{\text{active}}B} \cdot \frac{1}{j\frac{\pi f_1}{BN_0} + 1}, \quad (4.10)$$

with the input bias dependent cutoff frequency of

$$f_c = \frac{1}{\pi} \cdot \sqrt{\frac{I_0B}{qV_{\text{active}}}}. \quad (4.11)$$

From Eqs. (4.10) and (4.11), the 1st-order Volterra Kernel may be calculated by the

4. An Analytic Model of Dynamic Nonlinearities in Directly Modulated LEDs

inverse Fourier transform as

$$h_1(\tau_1) = \mathcal{F}^{-1}\{\underline{H}_1(\omega_1)\} = \frac{1}{2\pi} \int_{-\infty}^{\infty} \underline{H}_1(\omega_1) e^{j\omega_1\tau_1} d\omega_1. \quad (4.12)$$

4.2.2. Second-Order Part

The time domain representation of the 2nd-order part of the Volterra series maps the input signal $x(t)$ to its output signal $y_2(t)$ as

$$y_2(t) = \int_{-\infty}^{\infty} \int_{-\infty}^{\infty} h_2(\tau_1, \tau_2) x(t - \tau_1) x(t - \tau_2) d\tau_1 d\tau_2 = \mathbf{H}_2[x(t)]. \quad (4.13)$$

In analogy to Eq.(4.9), the frequency domain representation of Eq.(4.13) shall be derived.

The frequency domain representation of the 2nd-order Volterra kernel is given by a 2D Fourier transform as [64]

$$\underline{H}_2(\omega_1, \omega_2) = \int_{-\infty}^{\infty} \int_{-\infty}^{\infty} h_2(\tau_1, \tau_2) e^{-j\omega_1\tau_1} e^{-j\omega_2\tau_2} d\tau_1 d\tau_2. \quad (4.14)$$

In order to express the output spectrum $\underline{Y}_2(\omega)$ in terms of the input spectrum $\underline{X}(\omega)$ and $\underline{H}_2(\omega_1, \omega_2)$, Eq. (4.13) is re-written as

$$y_{(2)}(t_1, t_2) = \int_{-\infty}^{\infty} \int_{-\infty}^{\infty} h_2(\tau_1, \tau_2) x(t_1 - \tau_1) x(t_2 - \tau_2) d\tau_1 d\tau_2, \quad (4.15)$$

where an artificial output signal $y_{(2)}(t_1, t_2)$ is introduced [64], which is related to $y_2(t)$ by

$$y_{(2)}(t_1 = t, t_2 = t) = y_2(t). \quad (4.16)$$

The 2D Fourier transform of $y_{(2)}(t_1, t_2)$ is given as

$$\underline{Y}_{(2)}(\omega_1, \omega_2) = \int_{-\infty}^{\infty} \int_{-\infty}^{\infty} y_{(2)}(t_1, t_2) e^{-j\omega_1 t_1} e^{-j\omega_2 t_2} dt_1 dt_2. \quad (4.17)$$

Substituting Eq. (4.15) into Eq. (4.17) yields

$$\underline{Y}_{(2)}(\omega_1, \omega_2) = \int_{-\infty}^{\infty} \int_{-\infty}^{\infty} \int_{-\infty}^{\infty} \int_{-\infty}^{\infty} h_2(\tau_1, \tau_2) x(t_1 - \tau_1) x(t_2 - \tau_2) e^{-j(\omega_1 t_1 + \omega_2 t_2)} d\tau_1 d\tau_2 dt_1 dt_2. \quad (4.18)$$

By further substituting the variables

$$\begin{aligned} \sigma_1 &= t_1 - \tau_1 \\ \sigma_2 &= t_2 - \tau_2, \end{aligned}$$

4.2. Frequency Domain Representation of the Nonlinear System

the integrals in Eq. (4.18) may be separated as

$$\begin{aligned}
 \underline{Y}_{(2)}(\omega_1, \omega_2) &= \int_{-\infty}^{\infty} \int_{-\infty}^{\infty} \int_{-\infty}^{\infty} \int_{-\infty}^{\infty} h_2(\tau_1, \tau_2) x(\sigma_1) x(\sigma_2) e^{-j[\omega_1(\sigma_1+\tau_1)+\omega_2(\sigma_2+\tau_2)]} d\tau_1 d\tau_2 d\sigma_1 d\sigma_2 \\
 &= \int_{-\infty}^{\infty} \int_{-\infty}^{\infty} h_2(\tau_1, \tau_2) e^{-j\omega_1\tau_1} e^{-j\omega_2\tau_2} d\tau_1 d\tau_2 \cdot \int_{-\infty}^{\infty} x(\sigma_1) e^{-j\omega_1\sigma_1} d\sigma_1 \cdot \int_{-\infty}^{\infty} x(\sigma_2) e^{-j\omega_2\sigma_2} d\sigma_2 \\
 &= \underline{H}_2(\omega_1, \omega_2) \cdot \underline{X}(\omega_1) \cdot \underline{X}(\omega_2), \tag{4.19}
 \end{aligned}$$

with the 2nd-order kernel transform $\underline{H}_2(\omega_1, \omega_2)$ and the input signal spectrum $\underline{X}(\omega)$ at the frequencies ω_1 and ω_2 . What remains to determine is the relation between $\underline{Y}_{(2)}(\omega_1, \omega_2)$ and the output spectrum $\underline{Y}_2(\omega)$.

The inverse 2D Fourier transform of $\underline{Y}_{(2)}(\omega_1, \omega_2)$ is given as

$$y_{(2)}(t_1, t_2) = \frac{1}{(2\pi)^2} \int_{-\infty}^{\infty} \int_{-\infty}^{\infty} \underline{Y}_{(2)}(\omega_1, \omega_2) e^{j(\omega_1 t_1 + \omega_2 t_2)} d\omega_1 d\omega_2, \tag{4.20}$$

and with Eq. (4.16)

$$y_2(t) = y_{(2)}(t, t) = \frac{1}{(2\pi)^2} \int_{-\infty}^{\infty} \int_{-\infty}^{\infty} \underline{Y}_{(2)}(\omega_1, \omega_2) e^{j(\omega_1 + \omega_2)t} d\omega_1 d\omega_2. \tag{4.21}$$

Substituting $\omega = \omega_1 + \omega_2$ gives

$$y_2(t) = \frac{1}{(2\pi)^2} \int_{-\infty}^{\infty} \int_{-\infty}^{\infty} \underline{Y}_{(2)}(\omega_1, \omega - \omega_1) e^{j\omega t} d\omega_1 d\omega, \tag{4.22}$$

which is the form of an inverse Fourier transform (cf. Eq. (4.12))

$$y_2(t) = \frac{1}{2\pi} \int_{-\infty}^{\infty} \underline{Y}_2(\omega) e^{j\omega t} d\omega \tag{4.23}$$

with

$$\underline{Y}_2(\omega) = \frac{1}{2\pi} \int_{-\infty}^{\infty} \underline{Y}_{(2)}(\omega_1, \omega - \omega_1) d\omega_1. \tag{4.24}$$

It is seen that the output spectrum $\underline{Y}_2(\omega)$ produced by the 2nd-order Volterra kernel transform lies at the frequency $\omega = \omega_1 + \omega_2$, which is actually the frequency of the IM2. The integral in Eq. (4.24) corresponds to an integration along a diagonal in the IM2 matrix representation, as shown in Fig. 3.21 (left) on page 70. For the special case of a twotone excitation with a fixed ω_1 and ω_2 , however, the integration with respect to ω_1 vanishes and $\underline{Y}_2(\omega)$ corresponds to the unique point in the IM2 matrix given by the input frequency pair $[\omega_1, \omega_2]$. That is, the frequency domain representation of the

4. An Analytic Model of Dynamic Nonlinearities in Directly Modulated LEDs

2nd-order Volterra operator

$$\mathbf{H}_2[x(t)] = \int_{-\infty}^{\infty} \int_{-\infty}^{\infty} h_2(\tau_1, \tau_2) x(t - \tau_1) x(t - \tau_2) d\tau_1 d\tau_2, \quad (4.25)$$

which describes the generation of the nonlinearities (lower signal path in Fig. 4.2) and is given by Eq. (4.19) actually corresponds to the frequency response of the IM2, as evaluated in Figs. 3.22 and 3.23. Therefore, with Eq. (4.19) and under the assumption of a twotone excitation where both tones exhibit the same input amplitude for all investigated frequency pairs, measuring a normalized magnitude response of $Y_2(\omega)$ is equivalent to measuring the normalized magnitude response of the 2nd-order Volterra kernel transform $\underline{H}_2(\omega_1, \omega_2)$.

An analytic model of the LED as a 2nd-order nonlinear system is therefore fully described by an analytic expression for the linear frequency response $\underline{H}_1(\omega)$, which was derived in Ch. 3.2.1 and the frequency response of the IM2, as observed in Figs. 3.22 and 3.23 and described by $\underline{H}_2(\omega_1, \omega_2)$. When applied as an LED model, the input signal $x(t)$ would be given by the LED input current $i(t)$ and the system's output signal $y(t)$ would be the optical output power $p_{\text{opt}}(t)$.

An analytic description for $\underline{H}_2(\omega_1, \omega_2)$ which predicts the frequency dependent IM2 at the output of the LED will be derived in the following chapters.

4.2.3. Some Important Nonlinear Models

The 2nd-order Volterra kernel transform allows to identify some special cases of dynamic nonlinear systems.

The Wiener Model

Figure 4.3a shows a dynamically nonlinear system which is mathematically described by an LTI system (which introduces a memory) followed by a static (i.e. memoryless) nonlinearity. Such a system is referred to as a *Wiener model* [66]. The 2nd-order Volterra kernel transform of a Wiener model exhibits some special features, as exemplarily shown in Fig. 4.3b.

The Wiener model example of Fig. 4.3b is composed of a 1st-order lowpass with a -3dB cutoff frequency of 20 MHz, followed by a memoryless 2nd-order nonlinearity, i.e.

$$y(t) = \left[\int_{-\infty}^{\infty} h_{\text{LP}}(\tau) x(t - \tau) d\tau \right]^2,$$

with the impulse response $h_{\text{LP}}(\tau)$ of the lowpass.

For a Wiener model it is observed, that the magnitudes at $f_{\text{IM, pos}} = |f_2| + |f_1|$ and $f_{\text{IM, neg}} = |f_2| - |f_1|$ are the same, as exemplarily marked in Fig. 4.3b. Furthermore, for $f_1 = f_2$, the IM2 at $f_2 + f_1$ exhibits the square of the LTI response, in this case a lowpass with a drop of -6 dB at 20 MHz (marked by the circle in Fig. 4.3b).

It is obvious that the Volterra kernel transforms of Figs. 3.22 and 3.23 found for the LEDs do not represent a Wiener model characteristic. As a result, the LED cannot be simplified to the system-theoretic structure of Fig. 4.3a.

4.2. Frequency Domain Representation of the Nonlinear System

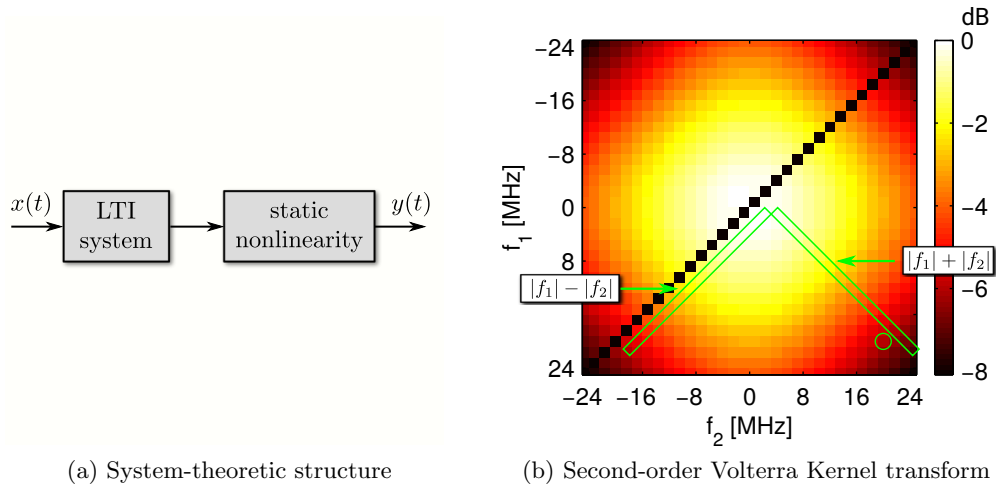


Figure 4.3.: The Wiener model

The Hammerstein Model

Another simplified 2nd-order nonlinear system is shown in Fig.4.4a. The system is composed of a static (memoryless) nonlinear process, followed by an LTI process, which introduces a memory. This model is referred to as a *Hammerstein model* [66]. The corresponding 2nd-order Volterra kernel transform is shown in Fig.4.4b, using again the exemplary 1st-order lowpass with $f_c = 20$ MHz and a squarer. The time domain output signal is given as

$$y(t) = \int_{-\infty}^{\infty} h_{\text{LP}}(\tau) [x(t - \tau)]^2 d\tau.$$

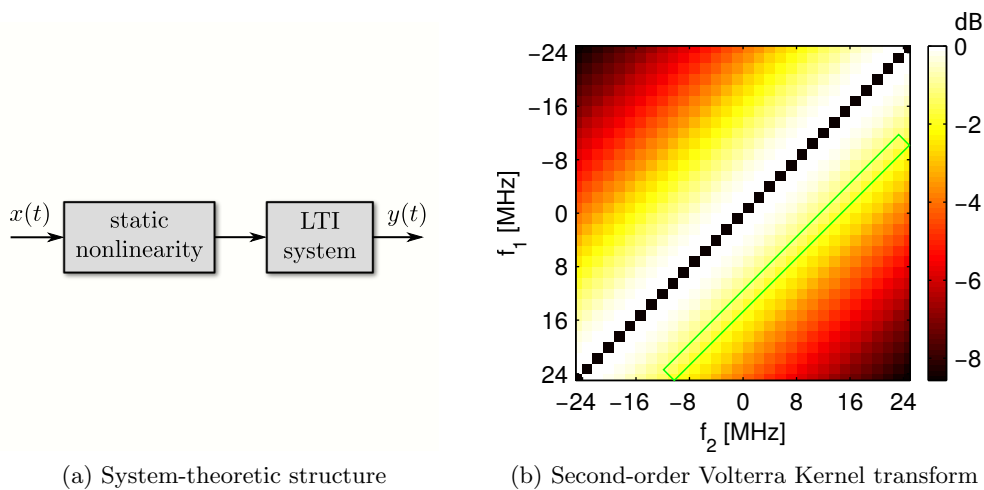


Figure 4.4.: The Hammerstein model

It is seen, that the Volterra kernel transform of a Hammerstein model exhibits at each f_{IM} a magnitude which is independent of the input frequencies f_1, f_2 . For example, the

4. An Analytic Model of Dynamic Nonlinearities in Directly Modulated LEDs

magnitude at $f_{\text{IM,pos}} = f_2 + f_1$ is the same for the input frequency pair $f_2 = 10.4$ MHz, $f_1 = 4$ MHz and the frequency pair $f_2 = 0.8$ MHz, $f_1 = 13.6$ MHz. This is indicated by constant diagonals in the kernel transform, as marked in Fig. 4.4b. Furthermore, the LTI frequency response is found on the diagonal of $f_2 = f_1$, but stretched with respect to the frequency axis by a factor of two.

A comparison with the results of Figs. 3.22 and 3.23 shows that the LEDs can also not be accurately described by a Hammerstein model. This demonstrates that the dynamic nonlinearities of an LED are mathematically of a more complex nature. The memory effects and the nonlinearities cannot be separated.

In the following sections, a simplified analytic expression of the observed dynamic nonlinear behaviour will be derived. The mathematical foundation of this derivation is the carrier density rate equation model of Ch. 2.7. The derivation is done using the so-called *harmonic balance* approach. The 2nd-order Volterra kernel transform $H_2(\omega_1, \omega_2)$ of the LED is derived, which is parametrized by the device parameters found in Eqs. (2.70) and (2.71) on page 43f.

4.3. The Harmonic Balance Approach

The method of harmonic balance is a frequently used mathematical approach to characterize nonlinear devices. It is often used in the microwave area for nonlinear devices such as mixers [67, 68], but has also been applied to the characterization of directly modulated laser diodes [69].

The approach assumes a steady state of the device. The basic idea is that the nonlinear device under investigation, which is defined by a mathematical model describing the underlying physics, is driven by a linear network with a finite number of harmonics. For the case of an LED, the LED is driven by a current source of the form

$$i_{\text{LED}}(t) = I_0 + \sum_{n=1}^N I_n \cos(2\pi f_n t + \phi_{I_n}), \quad (4.26)$$

where the number N of tones at the LED input is to be determined based on the specific problem formulation.

The nonlinear device will generate higher-order harmonics and intermodulation products, which introduce an additional number P of harmonics at frequencies f_p . But due to the linear character of the signal source, these additional tones must balance to zero at the interface between the linear source and the nonlinear device. This results in a set of equations which describes all of the investigated harmonics as a function of the physical device parameters.

Mathematically, the number P of additional tones can reach high values for multitone excitations. But in practice, the investigation must be restricted to a limited number of tones. The harmonic balance approach is therefore a simplified mathematical description of the nonlinear device under the boundary conditions of harmonic excitation and steady state.

4.4. A Harmonic Balance Model of Communication LEDs

The physical device model is given by Eqs. (2.70) and (2.71) on page 43f. The carrier density rate equation (2.70) may be re-arranged as

$$i(t) = i_{\text{LED}}(t) = \underbrace{qV_{\text{active}} \frac{dn}{dt}}_{i_a(t)} + \underbrace{qV_{\text{active}} B n^2}_{i_b(t)}. \quad (4.27)$$

That is, the LED may be represented by an electrical equivalent circuit as depicted in Fig. 4.5, where two controlled current sources $i_a(t)$, $i_b(t)$ are introduced.

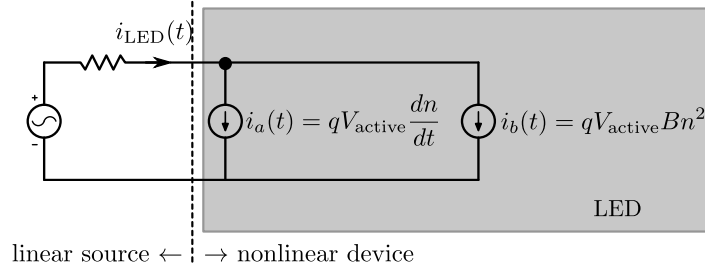


Figure 4.5.: Equivalent circuit of the LED according to the device model of Ch. 2.7.

The input tones and the nonlinearly generated tones are given by the problem formulation: The model shall predict the IM2 for a biased twotone excitation of the LED, that is, for

$$i_{\text{LED}}(t) = I_0 + \sum_{n=1}^2 I_n \cos(2\pi f_n t + \phi_{I_n}) := I_0 + i_1(t) + i_2(t), \quad (4.28)$$

where

$$\begin{aligned} i_1(t) &= I_1 \cos(2\pi f_1 t + \phi_{I_1}) = I_1 \cos(\omega_1 t + \phi_{I_1}) \\ &= \frac{1}{2} [I_1 e^{j\omega_1 t} + I_1^* e^{-j\omega_1 t}], \quad \omega_1 \geq 0 \end{aligned} \quad (4.29)$$

with

$$\underline{I}_1 = I_1 e^{j\phi_{I_1}},$$

which contains the magnitude and phase at the frequency ω_1 . Likewise, for the second input tone

$$\begin{aligned} i_2(t) &= I_2 \cos(2\pi f_2 t + \phi_{I_2}) = I_2 \cos(\omega_2 t + \phi_{I_2}) \\ &= \frac{1}{2} [I_2 e^{j\omega_2 t} + I_2^* e^{-j\omega_2 t}], \quad \omega_2 \geq 0 \end{aligned} \quad (4.30)$$

with

$$\underline{I}_2 = I_2 e^{j\phi_{I_2}}.$$

The two nonlinearly generated tones of interest are the IM2 tones at the intermod-

4. An Analytic Model of Dynamic Nonlinearities in Directly Modulated LEDs

ulation frequencies $\pm\omega_{\text{IM,pos}} := \pm(\omega_1 + \omega_2)$ and $\omega_{\text{IM,neg}} := \pm(\omega_1 - \omega_2)$ in the optical output signal of the LED. This intermodulation signal at the LED output shall therefore be written as

$$\begin{aligned} p_{\text{IM}}(t) &= p_{\text{IM,pos}}(t) + p_{\text{IM,neg}}(t) \\ &= \frac{1}{2} [P_{\text{IM,pos}} \cdot e^{j\omega_{\text{IM,pos}}t} + P_{\text{IM,pos}}^* \cdot e^{-j\omega_{\text{IM,pos}}t}] \\ &\quad + \frac{1}{2} [P_{\text{IM,neg}} \cdot e^{j\omega_{\text{IM,neg}}t} + P_{\text{IM,neg}}^* \cdot e^{-j\omega_{\text{IM,neg}}t}], \end{aligned} \quad (4.31)$$

with

$$\begin{aligned} \underline{P}_{\text{IM,pos}} &= P_{\text{IM,pos}} e^{j\phi_{P,\text{IMpos}}} \\ \underline{P}_{\text{IM,neg}} &= P_{\text{IM,neg}} e^{j\phi_{P,\text{IMneg}}}. \end{aligned}$$

The complex-valued terms $\underline{P}_{\text{IM,pos}}$ and $\underline{P}_{\text{IM,neg}}$ which contain the magnitudes and phases of the two IM2 tones shall be derived as a function of the input frequencies ω_1, ω_2 and the device parameters found in the device model of Eqs. (2.70) and (2.71) on page 43f.

Equations (2.70) and (2.71) may be interpreted as a two-stage process: The carrier density rate equation (2.70) models the conversion from electrical input current $i(t)$ to the 3D carrier density $n(t)$, Eq. (2.71) models the conversion from $n(t)$ to the optical output power $p_{\text{opt}}(t)$, which contains $p_{\text{IM}}(t)$. In order to identify which tones must be considered for the harmonic balance set of equations, the two equations are considered in reversed order.

Equation (2.71) describes $p(n)$ as a 2nd-order nonlinearity of $n(t)$. For the biased twotone excitation of Eq. (4.28) it is assumed that the carrier density $n(t)$ is also a superposition of a finite number M of tones, i.e. in analogy to Eq. (4.26)

$$n(t) = N_0 + \sum_{m=1}^M N_m \cos(\omega_m t + \phi_{N,m}) := N_0 + \sum_{m=1}^M n_m(t), \quad (4.32)$$

with

$$n_m(t) = N_m \cos(\omega_m t + \phi_{N,m}) = \frac{1}{2} [N_m e^{j\omega_m t} + N_m^* e^{-j\omega_m t}], \quad \omega_m \geq 0 \quad (4.33)$$

and

$$\underline{N}_m = N_m e^{j\phi_{N,m}}.$$

In analogy to Eq. (4.31), the two intermodulation tones in $n(t)$ with its corresponding terms lying at $\pm\omega_{\text{IM,pos}}$ and $\pm\omega_{\text{IM,neg}}$ shall be defined by

$$\begin{aligned} n_{\text{IM}}(t) &= n_{\text{IM,pos}}(t) + n_{\text{IM,neg}}(t) \\ &= \frac{1}{2} [N_{\text{IM,pos}} \cdot e^{j\omega_{\text{IM,pos}}t} + N_{\text{IM,pos}}^* \cdot e^{-j\omega_{\text{IM,pos}}t}] \\ &\quad + \frac{1}{2} [N_{\text{IM,neg}} \cdot e^{j\omega_{\text{IM,neg}}t} + N_{\text{IM,neg}}^* \cdot e^{-j\omega_{\text{IM,neg}}t}]. \end{aligned} \quad (4.34)$$

4.4. A Harmonic Balance Model of Communication LEDs

A noticeable contribution to the IM2 in the optical output signal $p_{\text{opt}}(t)$, as defined by $p_{\text{IM}}(t)$ of Eq. (4.31), is then generated by all harmonics in $n(t)$ which satisfy the frequency relation and exhibit certain minimum magnitudes N_m , since the tones in $p_{\text{opt}}(t)$ scale as $\propto N_m^2$ (cf. Eq. (2.71) on page 43).

Assuming therefore that the generation of harmonics at $\pm\omega_{\text{IM,pos}}$ and $\pm\omega_{\text{IM,neg}}$ in the optical output signal $p_{\text{opt}}(t)$ caused by any higher-order harmonics or intermodulation products which might be present in $n(t)$ is negligible due to their small magnitudes, only two 2nd-order intermodulations caused by the term Bn^2 will contribute to the generation of $p_{\text{IM}}(t)$:

- The IM2 between $n_1(t)$ and $n_2(t)$ and
- the IM2 between N_0 and $n_{\text{IM}}(t)$.

As a result, only these four terms of $n(t)$ must be considered in Eq. (2.71) on page 43 to describe $p_{\text{IM}}(t)$. This leads to the simplification

$$p_{\text{opt}}(t) = A_P \cdot [N_0 + n_1(t) + n_2(t) + n_{\text{IM}}(t)]^2, \quad (4.35)$$

with $A_P = \eta_{\text{extraction}} E_{\text{ph}} V_{\text{active}} B$. The above output signal $p_{\text{opt}}(t)$ of the LED is obviously a superposition of several tones. But with the simplifying assumptions introduced above, the output tones at the two IM2 frequencies are then defined by only two cross terms within the square brackets of the right-hand side of Eq. (4.35):

$$\begin{aligned} p_{\text{IM}}(t) &= p_{\text{IM,pos}}(t) + p_{\text{IM,neg}}(t) \\ &= A_P \cdot \left[\underbrace{2N_0 n_{\text{IM}}(t)}_{\text{IM2 of } N_0, n_{\text{IM}}(t)} + \underbrace{2n_1(t)n_2(t)}_{\text{IM2 of } n_1(t), n_2(t)} \right] \\ &= A_P N_0 [N_{\text{IM,pos}} e^{j\omega_{\text{IM,pos}} t} + N_{\text{IM,pos}}^* e^{-j\omega_{\text{IM,pos}} t} + N_{\text{IM,neg}} e^{j\omega_{\text{IM,neg}} t} + N_{\text{IM,neg}}^* e^{-j\omega_{\text{IM,neg}} t}] \\ &\quad + \frac{A_P}{2} [N_1 e^{j\omega_1 t} + N_1^* e^{-j\omega_1 t}] \cdot [N_2 e^{j\omega_2 t} + N_2^* e^{-j\omega_2 t}]. \end{aligned} \quad (4.36)$$

Sorting the right-hand side of (4.36) by the frequency components at

$$\begin{aligned} \omega_{\text{IM,pos}} &= \omega_1 + \omega_2 \\ -\omega_{\text{IM,pos}} &= -(\omega_1 + \omega_2) \\ \omega_{\text{IM,neg}} &= \omega_1 - \omega_2 \\ -\omega_{\text{IM,neg}} &= -(\omega_1 - \omega_2) \end{aligned}$$

gives

$$\begin{aligned} p_{\text{IM}}(t) &= A_P \left[N_0 N_{\text{IM,pos}} + \frac{N_1 N_2}{2} \right] e^{j\omega_{\text{IM,pos}} t} + A_P \left[N_0 N_{\text{IM,pos}}^* + \frac{N_1^* N_2^*}{2} \right] e^{-j\omega_{\text{IM,pos}} t} \\ &\quad + A_P \left[N_0 N_{\text{IM,neg}} + \frac{N_1 N_2^*}{2} \right] e^{j\omega_{\text{IM,neg}} t} + A_P \left[N_0 N_{\text{IM,neg}}^* + \frac{N_1^* N_2}{2} \right] e^{-j\omega_{\text{IM,neg}} t}. \end{aligned} \quad (4.37)$$

4. An Analytic Model of Dynamic Nonlinearities in Directly Modulated LEDs

Equation (4.37) describes the magnitudes and phases of the two IM2 tones in the output signal of the LED as a function of the bias N_0 and the tones $n_1(t)$, $n_2(t)$ and $n_{\text{IM}}(t)$, which are all part of the 3D carrier density $n(t)$. It is seen that the two variables $\underline{N}_{\text{IM, pos}}$ and $\underline{N}_{\text{IM, neg}}$ must be determined for the analytical description of the output IM2 tones. These two variables may be derived by applying the harmonic balance approach to the device model depicted in Fig. 4.5 with its corresponding Eq. (4.27).

For this, Eq. (4.27) is formulated for the four components lying at $\pm\omega_{\text{IM, pos}}$ and $\pm\omega_{\text{IM, neg}}$. The input tones are defined by Eq. (4.28), that is, for both $\pm\omega_{\text{IM, pos}}$ and $\pm\omega_{\text{IM, neg}}$, the left-hand side of Eq. (4.27) is zero. Applying further again the assumption that only the above mentioned two IM2 terms have a relevant contribution via Bn^2 to the signals at $\pm\omega_{\text{IM, pos}}$ and $\pm\omega_{\text{IM, neg}}$, Eq. (4.27) gives for the frequency $\omega_{\text{IM, pos}}$

$$\begin{aligned}
0 &= qV_{\text{active}} j\omega_{\text{IM, pos}} \frac{\underline{N}_{\text{IM, pos}}}{2} e^{j\omega_{\text{IM, pos}} t} \\
&\quad + qV_{\text{active}} B \left(\underbrace{\frac{\underline{N}_1 \underline{N}_2}{2} e^{j(\omega_1 + \omega_2)t}}_{\text{IM2 of } n_1(t), n_2(t)} + \underbrace{N_0 \underline{N}_{\text{IM, pos}} e^{j\omega_{\text{IM, pos}} t}}_{\text{IM2 of } N_0, n_{\text{IM}}(t)} \right) \\
&= j\omega_{\text{IM, pos}} \frac{\underline{N}_{\text{IM, pos}}}{2} + B \left(\frac{\underline{N}_1 \underline{N}_2}{2} + N_0 \underline{N}_{\text{IM, pos}} \right). \tag{4.38}
\end{aligned}$$

Likewise, for the frequency $\omega_{\text{IM, neg}}$ one obtains

$$\begin{aligned}
0 &= qV_{\text{active}} j\omega_{\text{IM, neg}} \frac{\underline{N}_{\text{IM, neg}}}{2} e^{j\omega_{\text{IM, neg}} t} \\
&\quad + qV_{\text{active}} B \left(\frac{\underline{N}_1 \underline{N}_2^*}{2} e^{j(\omega_1 - \omega_2)t} + N_0 \underline{N}_{\text{IM, neg}} e^{j\omega_{\text{IM, neg}} t} \right) \\
&= j\omega_{\text{IM, neg}} \frac{\underline{N}_{\text{IM, neg}}}{2} + B \left(\frac{\underline{N}_1 \underline{N}_2^*}{2} + N_0 \underline{N}_{\text{IM, neg}} \right). \tag{4.39}
\end{aligned}$$

Equations (4.38) and (4.39) may be re-arranged as

$$\underline{N}_{\text{IM, pos}}(\omega_1, \omega_2) = -\frac{B \underline{N}_1 \underline{N}_2}{j(\omega_1 + \omega_2) + 2BN_0}, \quad \omega_1, \omega_2 \geq 0 \tag{4.40}$$

and

$$\underline{N}_{\text{IM, neg}}(\omega_1, \omega_2) = -\frac{B \underline{N}_1 \underline{N}_2^*}{j(\omega_1 - \omega_2) + 2BN_0}, \quad \omega_1, \omega_2 \geq 0. \tag{4.41}$$

The complex-conjugates found in Eq. (4.34) are then given as

$$\underline{N}_{\text{IM, pos}}^*(\omega_1, \omega_2) = -\frac{B \underline{N}_1^* \underline{N}_2^*}{-j(\omega_1 + \omega_2) + 2BN_0}, \quad \omega_1, \omega_2 \geq 0 \tag{4.42}$$

and

$$\underline{N}_{\text{IM, neg}}^*(\omega_1, \omega_2) = -\frac{B \underline{N}_1^* \underline{N}_2}{-j(\omega_1 - \omega_2) + 2BN_0}, \quad \omega_1, \omega_2 \geq 0. \tag{4.43}$$

Equations (4.40) to (4.43) show that the two IM2 products in $n(t)$ are mathematically both dependent on \underline{N}_1 and \underline{N}_2 . The variable \underline{N}_1 which contains the magnitude and

4.4. A Harmonic Balance Model of Communication LEDs

phase of $n_1(t)$ (i.e. the tone at the input frequency ω_1 contained in $n(t)$) was previously derived and is given by Eq. (3.15) on page 55. The magnitude and phase of the second input tone are therefore given in analogy to Eq. (3.15) as

$$\begin{aligned} N_2(\omega_2) &= \frac{I_2}{qV_{\text{active}}} \cdot \frac{1}{j\omega_2 + 2BN_0} \\ &= \frac{I_2}{qV_{\text{active}}} \cdot \frac{2}{2BN_0} \cdot \frac{1}{j\frac{\omega_2}{2BN_0} + 1}. \end{aligned} \quad (4.44)$$

With $N_1^*(\omega_1) = N_1(-\omega_1)$ and $N_2^*(\omega_2) = N_2(-\omega_2)$, Eqs. (4.40) to (4.43) may be rewritten as

$$\begin{aligned} N_{\text{IM,pos}}(\omega_1, \omega_2) &= -\frac{BN_1(\omega_1)N_2(\omega_2)}{j(\omega_1 + \omega_2) + 2BN_0} \\ N_{\text{IM,neg}}(\omega_1, \omega_2) &= -\frac{BN_1(\omega_1)N_2(-\omega_2)}{j(\omega_1 - \omega_2) + 2BN_0} \\ N_{\text{IM,pos}}^*(\omega_1, \omega_2) &= -\frac{BN_1(-\omega_1)N(-\omega_2)}{j(-\omega_1 - \omega_2) + 2BN_0} \\ N_{\text{IM,neg}}^*(\omega_1, \omega_2) &= -\frac{BN_1(-\omega_1)N_2(\omega_2)}{j(-\omega_1 + \omega_2) + 2BN_0}. \end{aligned}$$

It is seen that these four formulas are the same, with only the signs of the corresponding input frequencies being different. As a result, the calculation of the two IM2 tones of interest which are found in $n(t)$ may be re-formulated in a single variable by extending the calculation to negative input frequencies using

$$N_{\text{IM}}(\omega_1, \omega_2) := -\frac{BN_1(\omega_1)N_2(\omega_2)}{j(\omega_1 + \omega_2) + 2BN_0} \quad (\omega_1, \omega_2 \text{ positive and negative}). \quad (4.45)$$

With two input variables (ω_1, ω_2) , a matrix representation which incorporates $N_{\text{IM,pos}}$, $N_{\text{IM,neg}}$, $N_{\text{IM,pos}}^*$, $N_{\text{IM,neg}}^*$ in its quadrants as sketched in Fig. 4.6 is convenient. This representation is then equivalent to the previously introduced matrix representation of the IM2.

The calculation of the four summands which describe the magnitudes and phases of the two IM2 tones in $n(t)$ (as introduced with Eq. (4.34)) is then done as

$$\begin{aligned} n_{\text{IM}}(t) &= \frac{N_{\text{IM}}(\omega_1, \omega_2)}{2} e^{j(\omega_1 + \omega_2)t} + \frac{N_{\text{IM}}(-\omega_1, -\omega_2)}{2} e^{j(-\omega_1 - \omega_2)t} \\ &\quad + \frac{N_{\text{IM}}(\omega_1, -\omega_2)}{2} e^{j(\omega_1 - \omega_2)t} + \frac{N_{\text{IM}}(-\omega_1, \omega_2)}{2} e^{j(-\omega_1 + \omega_2)t}, \quad \omega_1, \omega_2 \geq 0. \end{aligned} \quad (4.46)$$

4. An Analytic Model of Dynamic Nonlinearities in Directly Modulated LEDs

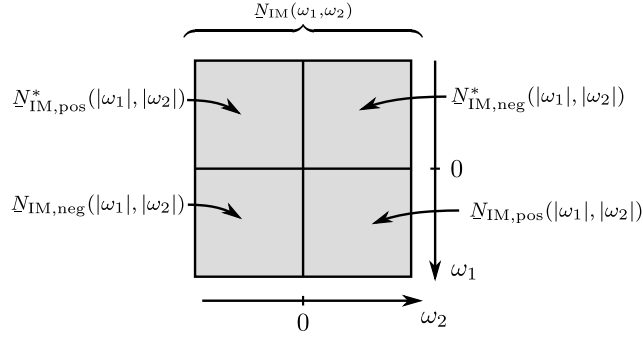


Figure 4.6.: The representation of the two IM2 signals at $\pm\omega_{\text{IM,pos}}$ and $\pm\omega_{\text{IM,neg}}$ with a single variable $\underline{N}_{\text{IM}}(\omega_1, \omega_2)$.

In the same fashion, the two IM2 tones at the output of the LED may be described by a single variable $\underline{P}_{\text{IM}}(\omega_1, \omega_2)$, where

$$p_{\text{IM}}(t) = \frac{\underline{P}_{\text{IM}}(\omega_1, \omega_2)}{2} e^{j(\omega_1 + \omega_2)t} + \frac{\underline{P}_{\text{IM}}(-\omega_1, -\omega_2)}{2} e^{j(-\omega_1 - \omega_2)t} \\ + \frac{\underline{P}_{\text{IM}}(\omega_1, -\omega_2)}{2} e^{j(\omega_1 - \omega_2)t} + \frac{\underline{P}_{\text{IM}}(-\omega_1, \omega_2)}{2} e^{j(-\omega_1 + \omega_2)t}, \quad \omega_1, \omega_2 \geq 0. \quad (4.47)$$

Putting Eq. (4.45) into (4.37) yields with Eq. (4.47)

$$\frac{\underline{P}_{\text{IM}}(\omega_1, \omega_2)}{2} = A_p \cdot \left[\frac{N_1(\omega_1)N_2(\omega_2)}{2} + N_0 \underline{N}_{\text{IM}}(\omega_1, \omega_2) \right], \quad (4.48)$$

with $A_p = \eta_{\text{extraction}} E_{\text{ph}} V_{\text{active}} B$. Equation (4.48) together with Eq. (4.47) is the representation of the magnitude and phase of the two IM2 tones found in the optical output power $p_{\text{opt}}(t)$ with a single variable by incorporating negative input frequencies into the calculation, just as introduced with $\underline{N}_{\text{IM}}$. Hence, the matrix representation shown in Fig. 4.6 may also be applied for $\underline{P}_{\text{IM}}$.

With Eq. (3.15) on page 55 and Eqs. (4.44) and (4.45), the frequency dependence of $\underline{P}_{\text{IM}}(\omega_1, \omega_2)$ may be derived as

4.4. A Harmonic Balance Model of Communication LEDs

$$\begin{aligned}
\frac{P_{\text{IM}}(\omega_1, \omega_2)}{2} &= A_P \left(\frac{N_1 N_2}{2} + N_0 N_{\text{IM}} \right) \\
&= A_P \left[\frac{N_1(\omega_1) N_2(\omega_2)}{2} - \frac{BN_0}{j(\omega_1 + \omega_2) + 2BN_0} N_1(\omega_1) N_2(\omega_2) \right] \\
&= A_P \frac{N_1(\omega_1) N_2(\omega_2)}{2} \cdot \left[1 - \frac{2BN_0}{j(\omega_1 + \omega_2) + 2BN_0} \right] \\
&= A_P \frac{N_1(\omega_1) N_2(\omega_2)}{2} \cdot \left[1 - \underbrace{\frac{1}{j \frac{\omega_1 + \omega_2}{2BN_0} + 1}}_{\text{1st-order lowpass}} \right] \\
&= A_P \frac{N_1(\omega_1) N_2(\omega_2)}{2} \cdot \left[\frac{j \frac{\omega_1 + \omega_2}{2BN_0}}{j \frac{\omega_1 + \omega_2}{2BN_0} + 1} \right] \\
&= 2A_P \cdot \underbrace{\frac{N_1(\omega_1)}{2}}_{\substack{\text{lowpass} \\ \omega_c = \\ 2BN_0}} \cdot \underbrace{\frac{N_2(\omega_2)}{2}}_{\substack{\text{lowpass} \\ \omega_c = \\ 2BN_0}} \cdot \underbrace{\left(\frac{1}{1 - j \frac{2BN_0}{\omega_1 + \omega_2}} \right)}_{\substack{\text{1st-order} \\ \text{highpass} \\ \omega_c = \\ 2BN_0}} \quad (\omega_1, \omega_2 \text{ positive and negative}),
\end{aligned} \tag{4.49}$$

with $A_P = \eta_{\text{extraction}} E_{\text{ph}} V_{\text{active}} B$.

A schematic representation of Eq. (4.49) is shown in Fig. 4.7. The frequency dependence of the IM2 is composed by a 1st-order lowpass filtering (H_{LP}) along ω_1 and along ω_2 , and a 1st-order highpass filtering along the IM2 frequency $\omega_{\text{IM}} = \omega_1 + \omega_2$.

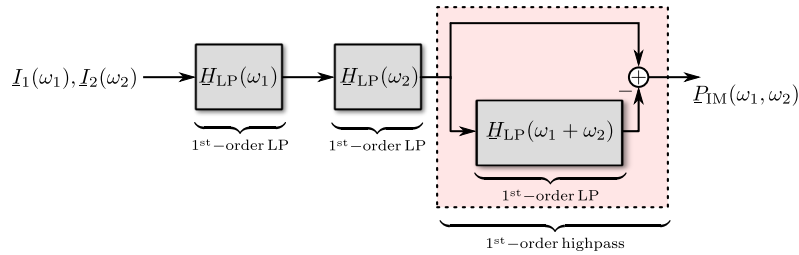


Figure 4.7.: Generation of the frequency-dependent IM2 according to Eq. (4.49).

With Eq. (4.19) on page 79, Eq. (3.15) on page 55 and (4.44), the 2nd-order Volterra kernel transform is then given as

4. An Analytic Model of Dynamic Nonlinearities in Directly Modulated LEDs

$$\begin{aligned} \underline{H}_2(\omega_1, \omega_2) &= \frac{P_{\text{IM}}(\omega_1, \omega_2)/2}{\frac{I_1(\omega_1)}{2} \frac{I_2(\omega_2)}{2}} = 2A_P \frac{N_1(\omega_1)N_2(\omega_2)}{I_1(\omega_1)I_2(\omega_2)} \cdot \left(\frac{1}{1 - j \frac{2BN_0}{\omega_1 + \omega_2}} \right) \\ &= \frac{\eta_{\text{extraction}} E_{\text{ph}}}{2V_{\text{active}} B [qN_0]^2} \cdot \frac{1}{j \frac{\omega_1}{\omega_c} + 1} \cdot \frac{1}{j \frac{\omega_2}{\omega_c} + 1} \cdot \frac{1}{1 - j \frac{\omega_c}{\omega_1 + \omega_2}}. \end{aligned} \quad (4.50)$$

It is seen that the magnitude of the IM2 scales with the model's device parameters. A comparison of Eq. (4.50) with the linear frequency response of Eq. (3.18) on page 55 shows that an underestimation of V_{active} , B , or N_0 may result in an overestimation of the corresponding dBc levels. This is a possible origin of the overestimation of the HD2 observed in Fig. 3.15 on page 66.

The calculation of the four summands describing the frequency dependence of the two IM2 tones at the LED's output is then achieved by simply extending the frequency ranges of the two input frequencies also to the corresponding negative values.

A graphical illustration of the process described by Eq. (4.50) is shown in Fig. 4.8 for the previously used LED device parameters and the IM2 matrix definition as introduced in Ch. 3.4. In Fig. 4.8, the three matrices on the left-hand side are multiplied element-wise to yield the matrix on the right-hand side. It is seen, that the resulting frequency characteristic fits well with the ones obtained by numerical simulations and lab measurements, cf. Figs. 3.22 and 3.23 on pages 71 and 72, respectively.

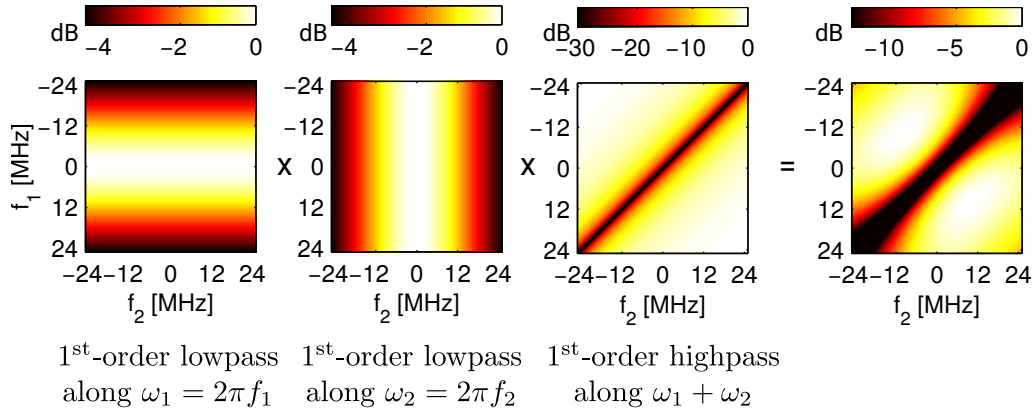


Figure 4.8.: Illustration of how the 2nd-order Volterra Kernel transform is generated.

With this analytic description, the frequency-dependent IM2 may be easily evaluated for all frequency ranges of interest without performing time consuming numerical simulations or lab measurements. Figure 4.9 shows exemplarily the normalized IM2 characteristic for input signal frequencies up to 100 MHz for the device parameters of Table 3.7 on page 65 (using $B = 8.47 \cdot 10^{-11} \text{cm}^3/\text{s}$) and the modulation parameters of model L8045 of Table 3.3 on page 50. It is observed that for higher frequencies the two lowpass characteristics dominate over the highpass part.

In the sense of the truncated Volterra series of Eq. (4.6) on page 76, the linear and nonlinear part of the E/O conversion of the LED is then fully described by Eq. (3.18) on page 55 and Eq. (4.50). The linear part $\underline{H}_1(\omega_1)$ is a 1st-order lowpass and the nonlinear part $\underline{H}_2(\omega_1, \omega_2)$ exhibits two 1st-order lowpass functions and a 1st-order highpass. The analytic model predicts that the frequency dependence of both $\underline{H}_1(\omega_1)$ and $\underline{H}_2(\omega_1, \omega_2)$

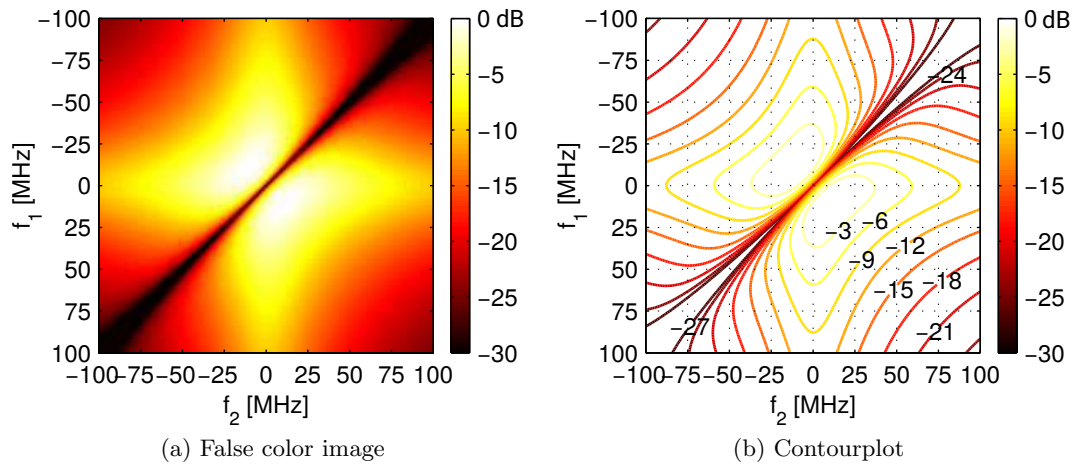


Figure 4.9.: Second-order intermodulation products at the LED output for input frequencies up to 100 MHz, calculated with Eq. (4.49).

scales with one common cutoff frequency of $\omega_c = 2BN_0$ or $f_c = BN_0/\pi$.

In the following, this analytic model will be verified by evaluating this interconnection of $\underline{H}_1(\omega_1)$ and $\underline{H}_2(\omega_1, \omega_2)$ in both numerical simulations of the carrier density rate equation model and measurements of the commercial LEDs.

5. Model Verification

The analytic LED model is verified in terms of its frequency domain representation, which is given by Eq. (3.18) on page 55 and Eq. (4.50) on page 90 as

$$\underline{H}_1(\omega_1) = \frac{\eta_{\text{extraction}} E_{\text{ph}}}{q} \cdot \frac{1}{j \frac{\omega_1}{\omega_c} + 1} \quad (5.1)$$

$$\underline{H}_2(\omega_1, \omega_2) = \frac{\eta_{\text{extraction}} E_{\text{ph}}}{2V_{\text{active}} B [qN_0]^2} \cdot \frac{1}{j \frac{\omega_1}{\omega_c} + 1} \cdot \frac{1}{j \frac{\omega_2}{\omega_c} + 1} \cdot \frac{1}{1 - j \frac{\omega_c}{\omega_1 + \omega_2}} \quad (5.2)$$

with

$$\omega_c = 2BN_0. \quad (5.3)$$

The model accuracy will be evaluated for different LED driving scenarios. In a first step, the model will be compared to the numerical simulation of the carrier density rate equation. This gives an indication on how the mathematical simplifications of the harmonic balance approach impact on the model accuracy and how the model could be adapted for an improved accuracy.

After that, the model will be verified against measurements of the commercial LEDs. This verification will be performed for a large-signal modulation, as used in a real communication scenario, and further for a small-signal modulation at different LED input bias currents. The latter investigation shall give insight on how the nonlinear part $\underline{H}_2(\omega_1, \omega_2)$ of the analytic model behaves at varying input bias, just as conducted in Ch. 3.2.2 for the linear part $\underline{H}_1(\omega_1)$.

Both $\underline{H}_1(\omega_1)$ and $\underline{H}_2(\omega_1, \omega_2)$ are evaluated for a finite number of input frequencies. The total number of input frequencies at which $\underline{H}_1(\omega_1)$ is evaluated is denoted M_1 and the total number of input frequency pairs at which $\underline{H}_2(\omega_1, \omega_2)$ is evaluated is denoted M_2 . The input frequencies of the n^{th} measurement are denoted $\omega_{1,n}$ and $\omega_{2,n}$. The accuracy is then evaluated in terms of a mean squared error (MSE) of the form

$$\begin{aligned} \text{MSE}_H &= \frac{1}{M_1} \sum_n^{M_1} [|\underline{H}_1(\omega_{1,n})| - |\underline{H}_{1,\text{ref}}(\omega_{1,n})|]^2 \\ \text{MSE}_{H_2} &= \frac{1}{M_2} \sum_n^{M_2} [|\underline{H}_2(\omega_{1,n}, \omega_{2,n})| - |\underline{H}_{2,\text{ref}}(\omega_{1,n}, \omega_{2,n})|]^2, \end{aligned} \quad (5.4)$$

where $|\underline{H}_{x,\text{ref}}|$ are the reference responses (either the numerically simulated or measured ones) and all linear and nonlinear frequency responses $|\underline{H}_x|$ are normalized to their respective maximum. This isolates the frequency characteristics from any non-unity multiplicative factors, as already investigated with the static P-I curve in Ch. 3.1.

The frequency ranges and number of measurements M_1 and M_2 for which MSE_H and MSE_{H_2} are evaluated may, in principle, be independently chosen. The comparison be-

5. Model Verification

tween the analytic harmonic balance model and the numerical simulation of the carrier density rate equation will therefore be conducted over a wider frequency range. The comparison between the harmonic balance model and lab measurements will, however, be conducted for the previously used frequency ranges due to the limitations of the equipment's sensitivity and due to the fact that the measurements are time consuming.

It was found in the previous chapter that the frequency characteristics of $\underline{H}_1(\omega_1)$ and $\underline{H}_2(\omega_1, \omega_2)$ of the analytic model are dependent on only one common cutoff frequency $\omega_c = 2BN_0$. The MSEs will therefore be used to check whether this unique ω_c is also found in the numerical simulations and lab measurements.

In order to do so, the MSE between the analytic model and measurement/numerical simulation will be evaluated by using the analytic model with a varying ω_c (or equivalently a varying recombination coefficient B , since $\omega_c = 2BN_0$). For a good agreement with the analytic model, the functions $\text{MSE}_H(B)$ and $\text{MSE}_{H_2}(B)$ are expected to be correlated with their minima at (ideally) the same B value. This evaluation also offers the advantage that the absolute values of the MSEs are of no concern; it is rather the shape of $\text{MSE}_H(B)$, $\text{MSE}_{H_2}(B)$ which matters.

In the following, the model is verified with an evaluation of $\text{MSE}_H(B)$ and $\text{MSE}_{H_2}(B)$ for $1 \cdot 10^{-11} \frac{\text{cm}^3}{\text{s}} \leq B \leq 0.5 \cdot 10^{-9} \frac{\text{cm}^3}{\text{s}}$. This range is motivated by typical ranges for B found in the literature (cf. Table. 3.1 on page 46).

5.1. Verification with the Numerical Simulation

The device parameters of Table. 3.1 on page 46 are used, but the numerical simulation, which serves as the reference for the analytic device model, uses the recombination coefficient of $B = 8.47 \cdot 10^{-11} \frac{\text{cm}^3}{\text{s}}$, as found for the real device (cf. page 56). The bias current is set to 20 mA. The linear frequency responses $|\underline{H}_1(\omega_1)|$ are evaluated for input frequencies up to about 100 MHz, the nonlinear frequency responses $\underline{H}_2(\omega_1, \omega_2)$ are evaluated for input frequencies up to about 50 MHz, which results in maximum IM2 output frequencies of about 100 MHz.

5.1.1. Small-Signal Modulation

Figure 5.1 shows the calculated $\text{MSE}_H(B)$ and $\text{MSE}_{H_2}(B)$ for a peak-to-peak modulation amplitude of 18 mA, which for $I_0 = 20$ mA corresponds to a modulation index of $m = 0.45$.

The curves of $\text{MSE}_H(B)$ and $\text{MSE}_{H_2}(B)$ show a clear correlation, with each curve having only one pronounced minimum. The fitted recombination coefficients for which the minimum MSE is reached are about $B = 8.4 \cdot 10^{-11} \frac{\text{cm}^3}{\text{s}}$ for $|\underline{H}_1(\omega_1)|$ and $B = 8.2 \cdot 10^{-11} \frac{\text{cm}^3}{\text{s}}$ for $|\underline{H}_2(\omega_1, \omega_2)|$. These values are close the value of $B = 8.47 \cdot 10^{-11} \frac{\text{cm}^3}{\text{s}}$ which is used in the underlying numerical simulation, and it may be concluded that under small-signal modulation the analytic device model based on the harmonic balance approach of Eqs. (5.1) to (5.3) fits well with the numerical simulation of the corresponding carrier density rate equation. The mathematical simplifications of the harmonic balance approach do not impose any major discrepancies.

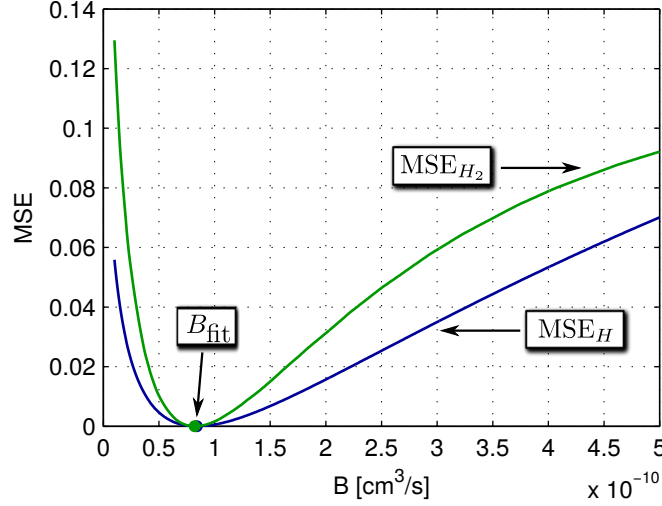


Figure 5.1.: Verification of the harmonic balance approach for small-signal modulation.

5.1.2. Large-Signal Modulation

The device parameters are the same as used for the small-signal model verification. The input bias current is again 20 mA, but the modulation amplitude is doubled compared to the small-signal investigation. The peak-to-peak modulation amplitude is now 36 mA, as previously used for the large-signal investigations. This corresponds to a modulation index of $m = 0.9$ and ensures that the LED input current is strictly positive.

The results for $MSE_H(B)$ and $MSE_{H_2}(B)$ are shown in Fig. 5.2. As observed for the small-signal modulation, both curves show a clearly correlated behaviour, again with one pronounced minimum. The fitted recombination coefficients to obtain a minimum MSE are now $B = 8.24 \cdot 10^{-11} \frac{\text{cm}^3}{\text{s}}$ for $|H_1(\omega_1)|$ and $B = 7.12 \cdot 10^{-11} \frac{\text{cm}^3}{\text{s}}$ for $|H_2(\omega_1, \omega_2)|$.

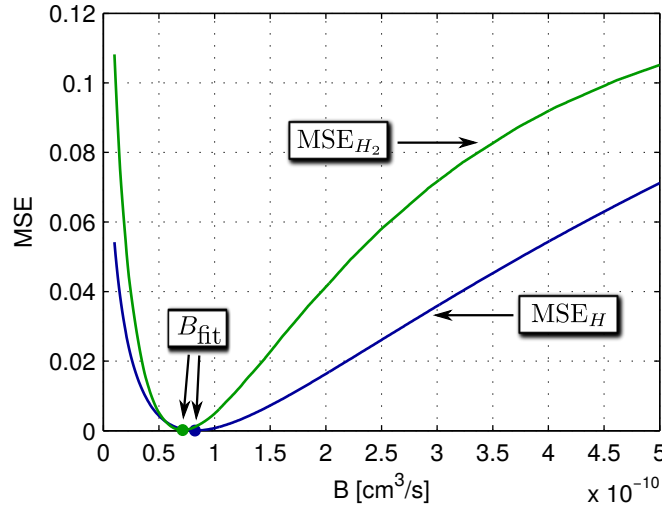


Figure 5.2.: Verification of the harmonic balance approach for large-signal modulation.

These values are slightly reduced compared to the values found for the small-signal modulation and compared to the target value of $B = 8.47 \cdot 10^{-11} \frac{\text{cm}^3}{\text{s}}$ used in the underlying numerical simulation. This moderate discrepancy may be attributed to the

5. Model Verification

fact that the simplifying assumption of $N_0^2 \gg |N_1|^2, |N_2|^2$, which was made for the calculation of N_0 (cf. the derivation of Eq. (3.13) on page 55), is no longer valid in that strict sense for a large-signal modulation.

In a more generalized case of a *large-signal* twotone modulation, Eq. (3.12) on page 55 would be re-written as

$$0 = \frac{I_0}{qV_{\text{active}}} - B \left[N_0^2 + \frac{|N_1|^2}{2} + \frac{|N_2|^2}{2} \right],$$

where it is considered that the squaring of a harmonic tone of magnitude N_x produces a DC offset of $|N_x|^2$. In that case, one obtains

$$N_{0, \text{large signal}} = \sqrt{\frac{I_0}{qV_{\text{active}}B} - \frac{|N_1|^2}{2} - \frac{|N_2|^2}{2}}.$$

As a result, the neglect of $|N_1|^2$ and $|N_2|^2$ in Eq. (3.13) produces a slight over-estimation of N_0 . With this knowledge, the use of a correction factor α in the form

$$N_0 = \alpha \cdot \sqrt{\frac{I_0}{qV_{\text{active}}B}}. \quad (5.5)$$

could be beneficial to improve the model's accuracy.

Table 5.1 shows exemplarily how different values of α impact on the fitted recombination coefficient. It is seen that values of $0.9 \leq \alpha < 1$ offer fitting results which are close to the theoretical optimum (in this case the known value of $B = 8.47 \cdot 10^{-11} \frac{\text{cm}^3}{\text{s}}$ used in the underlying numerical simulation).

Table 5.1.: Fitted recombination coefficient B_{fit} of $|H_2(\omega_1, \omega_2)|$ for different correction factors α .

α	B_{fit} in cm^3/s
1	$7.12 \cdot 10^{-11}$
0.95	$7.89 \cdot 10^{-11}$
0.9	$8.79 \cdot 10^{-11}$

5.2. Verification with Measurements

The analytic model is now verified against measurements with the commercial LEDs L8045 and SFH757V. For this, the FSO measurement setup of Fig. 3.6 on page 52 is used. The analytic model uses the same device parameters as in the previous chapter.

The linear frequency response $|H_1(\omega_1)|$ is measured up to about 80 MHz, the non-linear frequency response $|H_2(\omega_1, \omega_2)|$ is measured for input signal frequencies up to 25 MHz, which results in output IM2 frequencies of up to about 50 MHz.

The model verification is again done by evaluating the MSE of the normalized $|H_1(\omega_1)|$ and $|H_2(\omega_1, \omega_2)|$, as given by Eq. (5.4), for a varying recombination coefficient B in the analytic model. The correlation and minima of $\text{MSE}_H(B)$ and $\text{MSE}_{H_2}(B)$

serve as the measure for the accuracy of the analytic device model. The device model is first verified for small-signal modulation using LED L8045.

In Ch. 3.2.2, the bias dependence of the linear frequency response was addressed and the potential impact of a nonconstant recombination coefficient $B(T)$ was discussed. It was elucidated that this effect directly maps into the cutoff frequency of $\underline{H}_1(\omega_1)$.

Since the analytic device model predicts the same cutoff frequency ω_c for $\underline{H}_1(\omega_1)$ and $\underline{H}_2(\omega_1, \omega_2)$, it is expected that the effect of $B(T)$ is also found for $\underline{H}_2(\omega_1, \omega_2)$. To verify this, the accuracy of the device model is investigated at different input bias currents.

5.2.1. Small-Signal Modulation at varying Bias

To allow a direct comparison with the results obtained in Ch. 3.2.2, the same bias currents and modulation amplitudes are used. That is, input bias currents between 10 mA and 45 mA are investigated with a peak-to-peak modulation amplitude of 18 mA. The resulting input amplitude swings are then as shown in Fig. 3.8 on page 57.

The results for $\text{MSE}_H(B)$ and $\text{MSE}_{H_2}(B)$ are shown in Fig. 5.3, along with the corresponding fitted minima, which are marked by dots. It is seen that at all bias currents, the characteristics are qualitatively the same, each with one distinct minimum in the investigated range of $1 \cdot 10^{-11} \frac{\text{cm}^3}{\text{s}} \leq B \leq 0.5 \cdot 10^{-9} \frac{\text{cm}^3}{\text{s}}$. At each input bias, the curves of $\text{MSE}_H(B)$ and $\text{MSE}_{H_2}(B)$ are clearly correlated, and the minima are close together.

This demonstrates that the characteristics of the analytic device model, given by Eqs. (5.1) and (5.2) with its common cutoff frequency $\omega_c = 2BN_0$ are found with good accuracy also in the real device under small-signal modulation and for the entire input bias current range. It should here be pointed out, that the investigated commercial LED L8045 is rated up to 40 mA. That is, the analytic device model is validated even beyond the official LED's driving specifications. The MSE values of Fig. 5.3 are summarized in Table 5.2

Table 5.2.: Minimum MSE values of the fitting results of Fig. 5.3.

I_0 in mA	10	15	20	25	30	35	40	45
$\text{MSE}_H/10^{-4}$	2.14	1.86	1.73	1.36	1.48	1.47	1.35	1.31
$\text{MSE}_{H_2}/10^{-4}$	11.6	4.16	3.03	3.44	4.95	7.42	16.3	18

The fitted recombination coefficients versus bias current found at the minima of $\text{MSE}_H(B)$ and $\text{MSE}_{H_2}(B)$ are shown in Fig. 5.4. The results show that the fitted $B(I_0)$ of $|\underline{H}_1(\omega_1)|$ and $|\underline{H}_2(\omega_1, \omega_2)|$ are well correlated, just as predicted by the analytic model. However, the recombination coefficients are clearly bias-dependent, monotonically decreasing with increasing bias current. This may be attributed to the effects of junction temperature T on B , as discussed in Ch. 3.2.3. The fitting result for $|\underline{H}_1(\omega_1)|$ (blue curve in Fig. 5.4) is basically equivalent to the results presented in Fig. 3.11 on page 60. Minor discrepancies between the two results stem from the fact that they are obtained differently: The results of Fig. 3.11 are obtained from the -3 dB cutoff frequency read from the measured $|\underline{H}_1(\omega_1)|$, whereas the results of Fig. 5.4 use the MSE fit over the entire frequency range of $|\underline{H}_1(\omega_1)|$ with the resulting ω_c .

It is further observed in Fig. 5.4 that the fitted B values of $|\underline{H}_1(\omega_1)|$ and $|\underline{H}_2(\omega_1, \omega_2)|$ slightly diverge at low input bias currents. This may be attributed to an overestimation

5. Model Verification

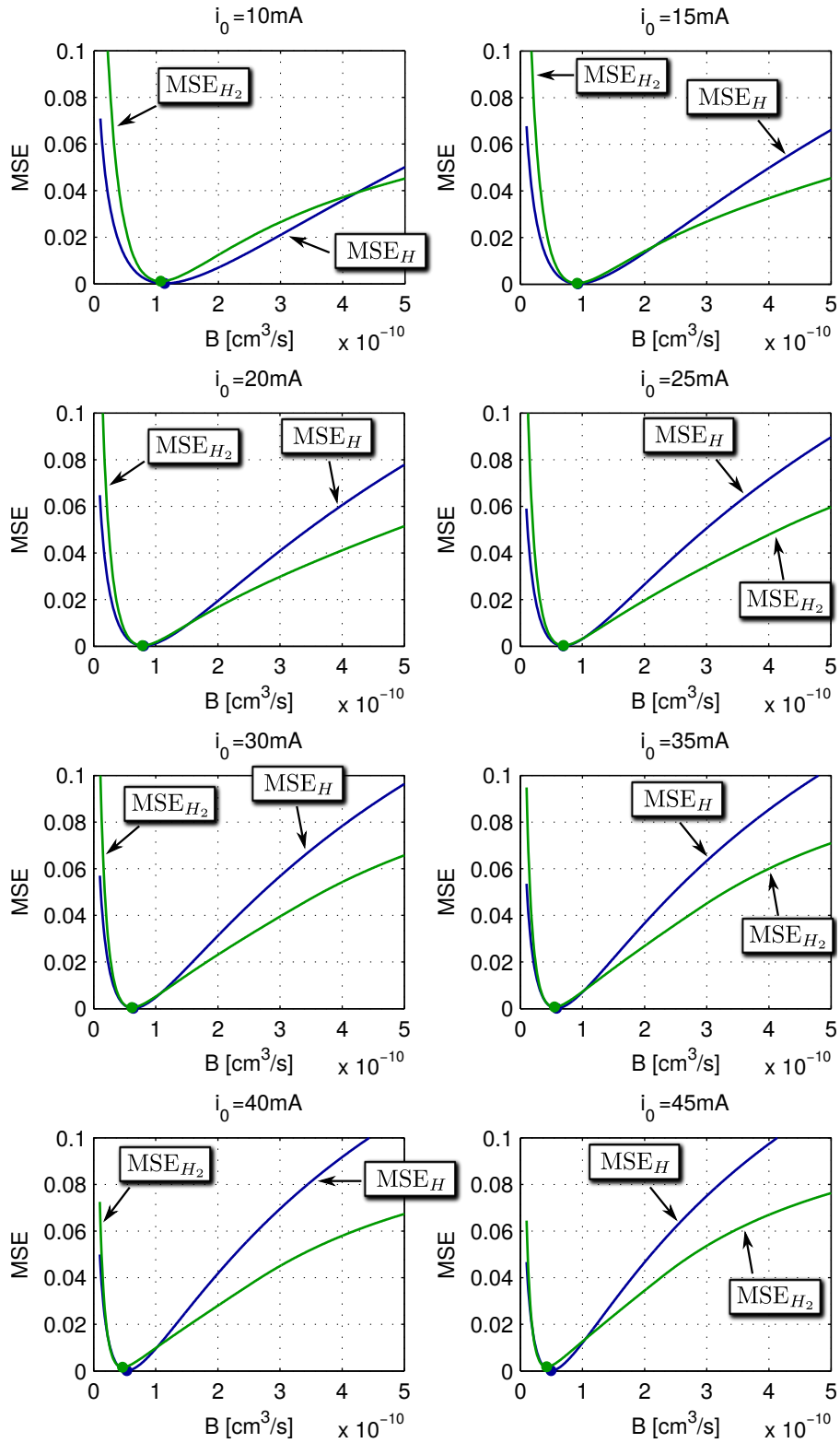


Figure 5.3.: Verification of the analytic device model for small-signal modulation at input bias currents between 10 mA and 45 mA (using LED model L8045).

of N_0 , as discussed above. When the LED is driven in this scenario, a correction factor α , as given by Eq. (5.5), may be added to the model to improve its accuracy.

Furthermore, the curves tend to diverge at input bias currents near the rated maximum. This may be caused by a slight impact of nonradiative carrier losses, such as Auger recombination or carrier leakage, cf. Ch. 2.5. In that case, the carrier density rate equation needs to be extended by the appropriate nonradiative recombination rate. However, the observed divergence between the two curves in Fig. 5.4 is only moderate, and hence the model may seem to be verified over the entire input current range.

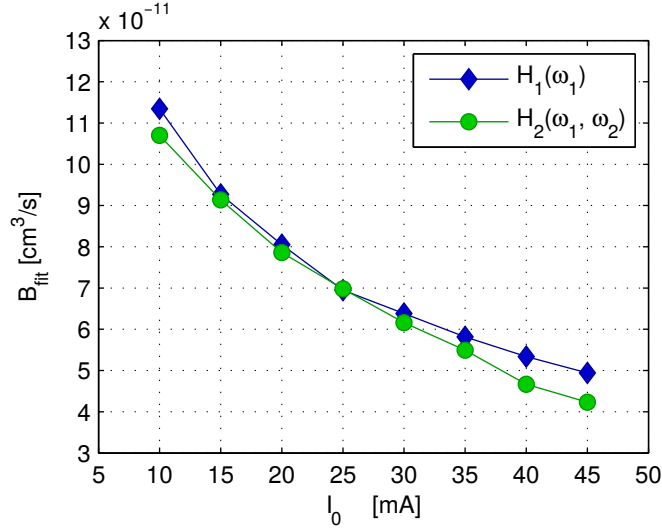


Figure 5.4.: Verification of the analytic device model for small-signal modulation at input bias currents between 10 mA and 45 mA: Fitted radiative recombination coefficients.

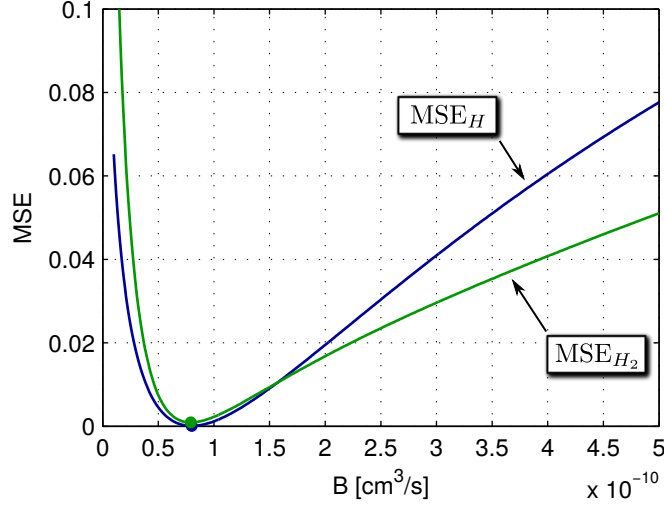
5.2.2. Large-Signal Modulation

The model verification shall be completed with an evaluation for large-signal modulation of the two commercial devices L8045 and SFH757V. Both LEDs are biased according to Table 3.3 on page 50.

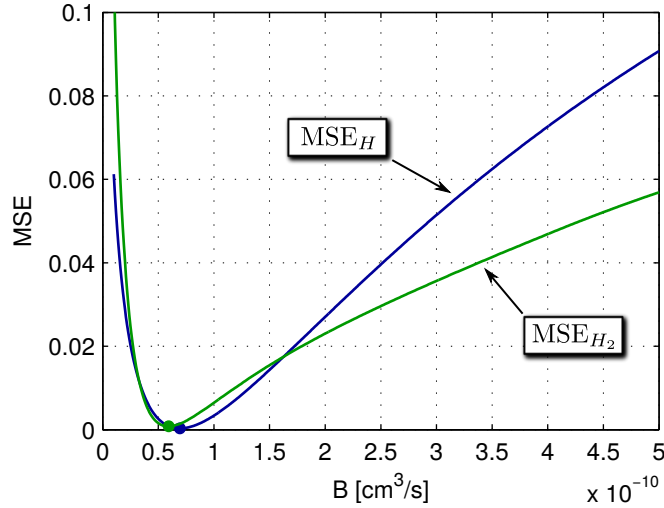
The results are shown in Fig. 5.5. For both devices a similar behaviour is observed with a clear correlation between $\text{MSE}_{H_1}(B)$ and $\text{MSE}_{H_2}(B)$ and a single pronounced minimum within the investigated range of B . For each device, the fitted recombination coefficient B of $|H_1(\omega_1)|$ and $|H_2(\omega_1, \omega_2)|$ are close together. This shows that the common ω_c predicted by the analytic device model is indeed found in the output characteristics of the LEDs, even for large-signal modulation. The fitted coefficients for model L8045 are $B_{\text{fit}} = 8 \cdot 10^{-11} \frac{\text{cm}^3}{\text{s}}$ (for $|H_1|$) and $B_{\text{fit}} = 7.92 \cdot 10^{-11} \frac{\text{cm}^3}{\text{s}}$ (for $|H_2|$).

The fitted values for model SFH757V are $B_{\text{fit}} = 6.95 \cdot 10^{-11} \frac{\text{cm}^3}{\text{s}}$ (for $|H_1|$) and $B_{\text{fit}} = 5.94 \cdot 10^{-11} \frac{\text{cm}^3}{\text{s}}$ (for $|H_2|$). That is, in both cases the recombination coefficient is slightly underestimated for $|H_2|$ compared to the value found for $|H_1|$. This may be attributed to an overestimation of N_0 , as discussed in Ch. 5.1.2 and may hence, in principle, be reduced with a properly chosen correction factor α .

5. Model Verification



(a) model L8045 at $I_0 = 20$ mA



(b) model SFH757V at $I_0 = 25$ mA

Figure 5.5.: Verification of the analytic device model for large-signal modulation of commercial communication LEDs.

5.3. Summary

The analytic nonlinear LED model was verified against numerical simulations of the carrier density rate equation and lab measurements of the real LEDs. For this, it was analyzed, whether the connection of the linear frequency response $|\underline{H}_1(\omega_1)|$ and the frequency response of the IM2, which in the device model is given by the common cutoff frequency $\omega_c = 2BN_0$ is also found in the carrier density rate equation and the real devices.

The results showed that this connection between $|\underline{H}_1(\omega_1)|$ and $|\underline{H}_2(\omega_1, \omega_2)|$ is indeed found in both the rate equation model and the real devices. A detailed analysis of the fitting results showed that the analytic expression of $|\underline{H}_2(\omega_1, \omega_2)|$, which is given by Eq. (5.2) tends to slightly underestimate ω_c . This effect may be attributed to the simplified assumption of the DC component of $N_0 = \sqrt{I_0/(qV_{\text{active}}B)}$ which is used for

the derivation of the harmonic balance model approach.

With this knowledge, a correction factor α , as introduced with Eq. (5.5) on page 96 is motivated in order to increase the model's accuracy. The optimum value of this factor is basically expected to be dependent on both the modulation index and the modulation bandwidth of the transmit signal. However, values of around $0.9 \leq \alpha \leq 0.95$ showed to be a good choice.

With the nonlinear LED model being successfully verified, different applications for the use in LED-based communication systems will be discussed in the next chapter.

6. Applications in LED-based Communication

The LED device model presented in this thesis gives detailed information on how the optical output signal of the directly modulated LED is nonlinearly distorted. For the design of LED-based communication systems, this is a valuable information which may be used in two ways to optimize a communication system:

Transmitter Model: The model (which is so far defined in the frequency domain) may be transformed into the time domain and may then be used as a building block for the optical transmitter in communication system simulation environments.

Signal Equalizer: With the knowledge of the nonlinear system defined by \underline{H}_1 and \underline{H}_2 , a system inverse may be derived which, under certain restrictions, is capable of equalizing the linear and nonlinear signal impairments caused by the LED.

These two applications are discussed in the following.

6.1. A Transmitter Model for Communication Systems

Simplified simulation models of the communication channel are a commonly used tool to investigate and optimize the system performance. Device models which incorporate a large number of physical effects often result in complicated models which require time consuming simulations and do not allow to give intuitive information about performance trends. Typical system parameters which are investigated are the modulation format (such as M -PAM or DMT) or the usable modulation bandwidth.

For example in [8], a simplified model of a step-index polymer optical fiber (SI-POF)-based short-range communication system with an LED as transmitter as depicted in Fig. 6.1 was introduced.

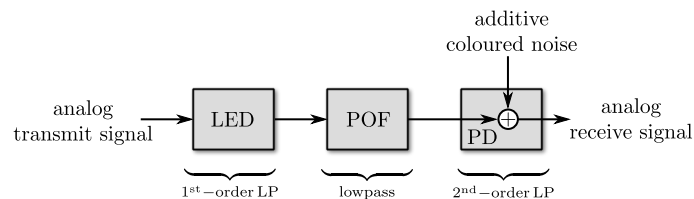


Figure 6.1.: Simplified channel model of an LED-SI-POF communication channel, according to [8].

Therein, the LED is modelled as a 1st-order lowpass, the SI-POF is also modelled as a lowpass function (with a bandwidth-length product of 4 MHz·km, caused by modal

6. Applications in LED-based Communication

dispersion), and the photo detector (PD) (which is assumed to consist of a photodiode followed by a two-stage trans-impedance amplifier (TIA)) is modelled as a 2nd-order lowpass of adjustable bandwidth. The dominant noise source is assumed to be the first stage of the TIA, and as a result, additive coloured noise is present at the receiver.

This model, which predicts only linear signal impairments, may now be easily extended with the LED device model derived in this work to incorporate also nonlinear transmitter signal impairments. The resulting block diagram is shown in Fig. 6.2.

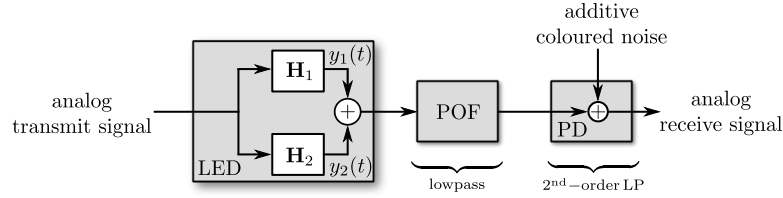


Figure 6.2.: Nonlinear channel model of an LED-SI-POF communication channel.

In Fig. 6.2, the LED is fully described by its 1st-order Volterra operator \mathbf{H}_1 and 2nd-order Volterra operator \mathbf{H}_2 , cf. Eq. (4.6) on page 76. This time domain representation of the LED allows a direct application of the nonlinear device model to arbitrary transmit signals, in analogy to the convolution performed by linear finite impulse response (FIR) filters.

The time domain representation is given by the Volterra kernels $h_1(\tau_1)$ and $h_2(\tau_1, \tau_2)$ (cf. Eq. (4.6) on page 76), which, in turn, may be calculated from the frequency domain device model of Eqs. (5.1) and (5.2) by their inverse Fourier transforms according to

$$h_1(\tau_1) = \frac{1}{2\pi} \int_{-\infty}^{\infty} \underline{H}_1(\omega_1) e^{j\omega_1\tau_1} d\omega_1 \quad (6.1)$$

$$h_2(\tau_1, \tau_2) = \frac{1}{(2\pi)^2} \int_{-\infty}^{\infty} \int_{-\infty}^{\infty} \underline{H}_2(\omega_1, \omega_2) e^{j\omega_1\tau_1 + j\omega_2\tau_2} d\omega_1 d\omega_2, \quad (6.2)$$

where the latter is a 2D inverse Fourier transform. When the Volterra series model shown Fig. 4.2 on page 76 is applied to an LED, the input signal $x(t)$ represents the input current $i(t)$ and the output signal $y(t)$ represents the optical output power $p_{\text{opt}}(t)$.

As seen from the time domain definition of the Volterra series of Eq. (4.6) on page 76, the 1st-order Volterra Kernel $h_1(\tau_1)$ relates its input and output signals by a convolution integral. As a result, $h_1(\tau_1)$ is equivalent to the impulse response of the 1st-order part and can therefore be directly implemented in the form of an FIR filter with the filter coefficients being equal to $h_1(\tau_1)$. In a similar manner, an impulse response of the 2nd-order part may be defined. The corresponding coefficients of the 2D FIR filter are then given as $h_2(\tau_1, \tau_2)/2$ [64]. Both $h_1(\tau_1)$ and $h_2(\tau_1, \tau_2)$ may in practice easily be calculated from $\underline{H}_1(\omega_1)$ and $\underline{H}_2(\omega_1, \omega_2)$ using an inverse FFT.

As an example, the time domain Volterra kernels obtained with the device parameters of Table 3.1 on page 46 with $B = 8.47 \cdot 10^{-11} \frac{\text{cm}^3}{\text{s}}$ for an input bias current of 20 mA are shown in Fig. 6.3. The kernels are here sampled at 1 GHz. It is seen that the nonlinear memory (the spread of $h_2(\tau_1, \tau_2)$) is basically the same as that of $h_1(\tau_1)$. However, the effective nonlinear memory length acting in a real communication scenario is expected to be dependent on the underlying modulation format (for example 8-PAM is more susceptible to nonlinearities than 2-PAM). From Fig. 6.3b it is seen that the number of coefficients required to model the nonlinearities scales with the square of the nonlinear memory length. Further, the 2nd-order Volterra kernel exhibits a symmetry along its diagonal $h_2(\tau, \tau)$ (with $\tau = \tau_1 = \tau_2$). As a result, a filter implementation may be reduced to one half of the $h_2(\tau_1, \tau_2)$ matrix (including the diagonal).

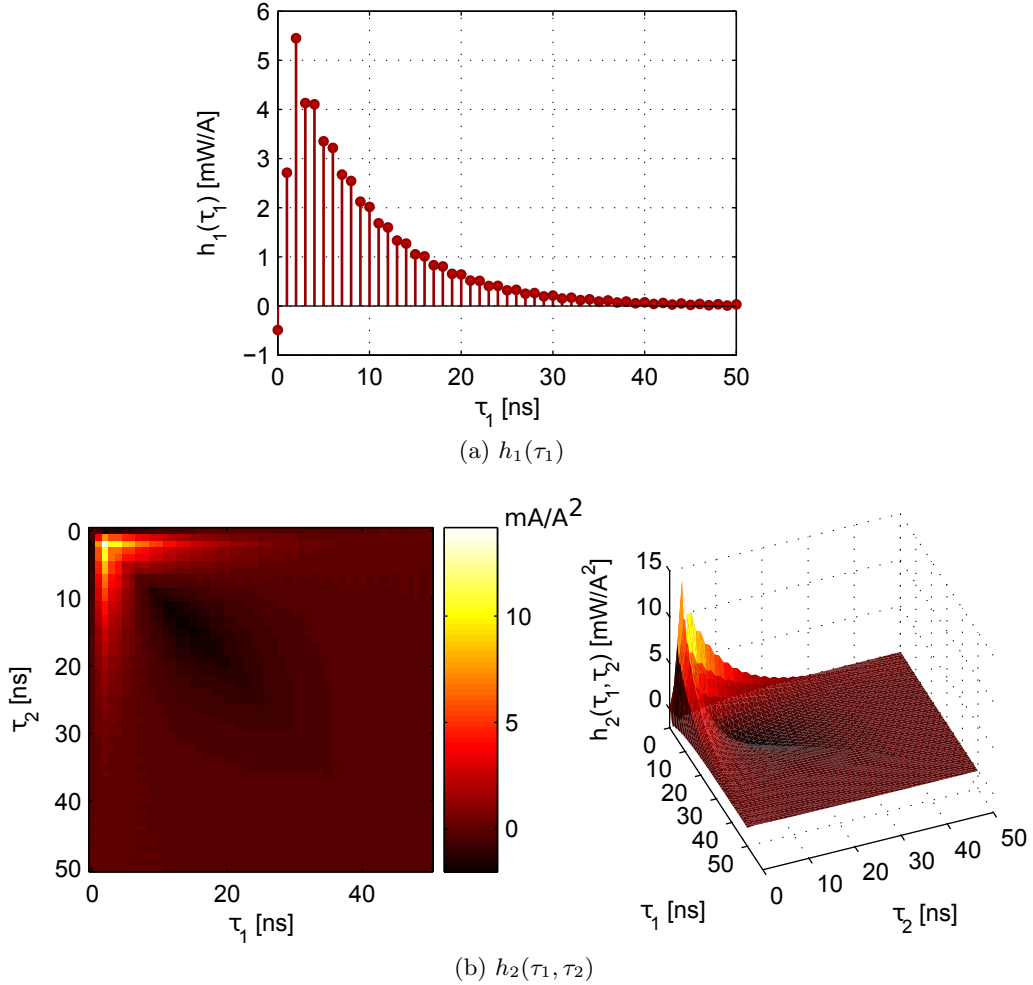


Figure 6.3.: Volterra kernels of the LED.

In order to apply the nonlinear time domain LED model to the simulation environment as shown in Fig. 6.2, the linear and nonlinear part must be implemented in a suitable time domain filter structure. The implementation of the linear part $\mathbf{H}_1[x(t)]$ is straightforward, as $h_1(\tau_1)$ represents the impulse response of an FIR filter. The implementation of $\mathbf{H}_2[x(t)]$ may be done with three matrices, as sketched in Fig. 6.4. The unbiased input signal is fed into two two-dimensional tapped delay lines. At each time

6. Applications in LED-based Communication

instant the three matrices are multiplied element-wise and the result is summed up to give the output $y_2(t)$.

The output signal of the LED is then given as the sum of the linear part's output $y_1(t)$ and the nonlinear part's output $y_2(t)$.

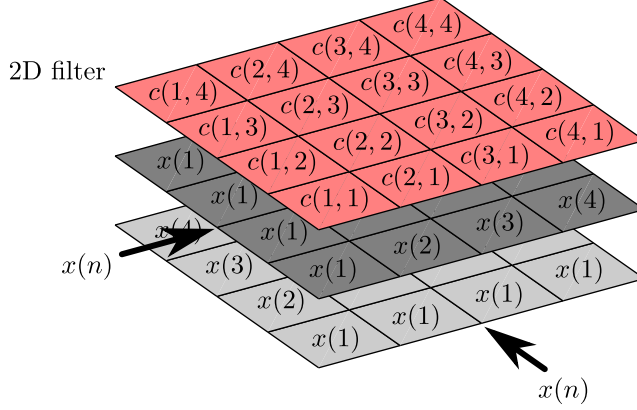


Figure 6.4.: Implementation of $\mathbf{H}_2[x(t)]$ using matrices as 2D tapped delay lines.

It is seen from Eqs. (5.1) and (5.2) on page 93 that an implementation of the nonlinear device model requires the knowledge of the radiative recombination coefficient B and the size of the active volume V_{active} as well the extraction efficiency $\eta_{\text{extraction}}$ and the photon energy E_{ph} . But it is seen, that, in principle, the latter two parameters are not required when the output of the transmitter device model is re-normalized to arbitrary units. The normalization factors A_{lin} and A_{NL} of the linear and nonlinear frequency responses of Eqs. (5.1) and (5.2) are

$$A_{\text{lin}} = \frac{\eta_{\text{extraction}} E_{\text{ph}}}{q},$$

$$A_{\text{NL}} = \frac{\eta_{\text{extraction}} E_{\text{ph}}}{2V_{\text{active}} B (qN_0)^2},$$

and may be re-normalized as

$$A_{\text{lin, norm}} \stackrel{!}{=} 1, \quad (6.3)$$

$$A_{\text{NL, norm}} = \frac{A_{\text{NL}}}{A_{\text{lin}}} = \frac{1}{2qV_{\text{active}} B N_0^2}. \quad (6.4)$$

6.2. Equalization with an Inverse Volterra Series Approach

The system-theoretic description of the LED in terms of a Volterra series allows to derive an inverse system, which may be used for signal equalization in a communication system. That is, this system inverse can compensate the observed 2nd-order nonlinearities introduced by the LED.

The underlying mathematical foundation is given by the so-called p^{th} -order inverse, developed by Schetzen [64, 70]. Based on this theory, an equalizer structure may be derived, which is capable of compensating nonlinearities up to the order p .

The tandem connection of a nonlinear system \mathbf{H} with its p^{th} -order inverse system \mathbf{K} is depicted in Fig. 6.5 (top). The output signal of the nonlinear system \mathbf{H} is given as

$$y(t) = \mathbf{H}[x(t)] = \sum_{n=1}^{\infty} \mathbf{H}_n[x(t)]. \quad (6.5)$$

The tandem connection of the nonlinear system \mathbf{H} with its p^{th} -order inverse \mathbf{K} forms then an overall nonlinear system \mathbf{Q} which has an output signal of

$$z(t) = \mathbf{K}[y(t)] = \mathbf{K}[\mathbf{H}[x(t)]] = \mathbf{Q}[x(t)] = \underbrace{x(t)}_{\text{equalized linear part}} + \underbrace{\sum_{n=p+1}^{\infty} \mathbf{Q}_n[x(t)]}_{\text{residual nonlinear orders}}. \quad (6.6)$$

That is, at the output of the overall system \mathbf{Q} , the linear part is equalized to give a delta function impulse response, nonlinear orders from 2 to p are compensated to zero, and nonlinear orders $n > p$ are still present.

Although only a limited number of nonlinear orders can be compensated with this approach, the technique proved to be promising; for example in [71] a 5th-order inverse was applied to compensate for fiber nonlinearities in a glass fiber SMF transmission system.

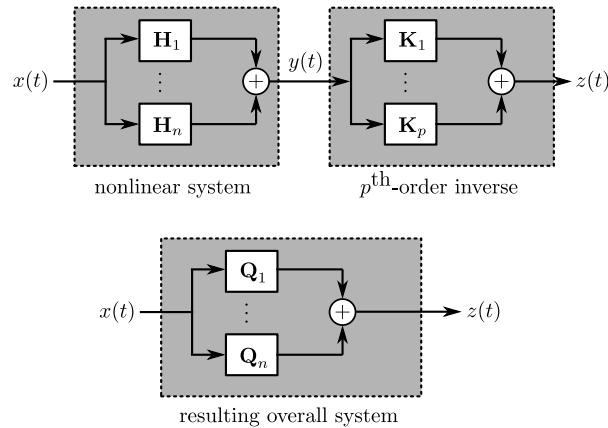


Figure 6.5.: Tandem connection of a Volterra-series-based system and its p^{th} -order inverse.

A block diagram of the tandem connection and the resulting overall system \mathbf{Q} is depicted in Fig. 6.5. From this block diagram it may be deduced that (due to the

6. Applications in LED-based Communication

parallel structure of a Volterra system) the n^{th} -order Volterra operator \mathbf{Q}_n is actually composed by various combinations of \mathbf{H}_a and \mathbf{K}_b (with a and b being various orders). But it is generally found that \mathbf{Q}_n is only dependent on orders of $j \leq n$ in the form [70]

$$\mathbf{Q}_n = \mathbf{K}_n \mathbf{H}_1 + \text{terms involving } \mathbf{K}_j \text{ for } j \leq (n-1). \quad (6.7)$$

This means that in order to compensate linear signal distortions and the 2nd-order nonlinearities originated in the LED, the system inverse requires only a 1st-order Volterra operator \mathbf{K}_1 and a 2nd-order Volterra operator \mathbf{K}_2 . It is easily seen that for this simplified situation, the Volterra operators of the equalized system are given as illustrated in Fig. 6.6 as

$$\mathbf{Q}_1[x(t)] = \mathbf{K}_1[y_1(t)] = \mathbf{K}_1 \mathbf{H}_1[x(t)], \quad (6.8)$$

$$\mathbf{Q}_2[x(t)] = \mathbf{K}_1[y_2] + \mathbf{K}_2[y_1] = \mathbf{K}_1 \mathbf{H}_2[x] + \mathbf{K}_2 \mathbf{H}_1[x]. \quad (6.9)$$

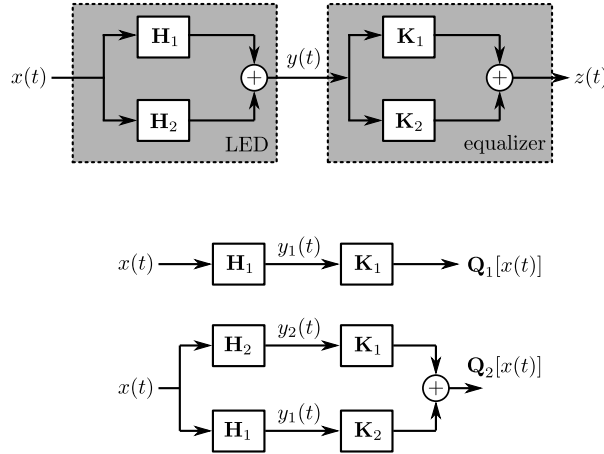


Figure 6.6.: Compensation of the LED nonlinearities with a 2nd-order inverse.

Equalization then requires

$$\mathbf{Q}_1[x(t)] \stackrel{!}{=} x(t), \quad (6.10)$$

$$\mathbf{Q}_2[x(t)] \stackrel{!}{=} 0. \quad (6.11)$$

Equation (6.10) states that the 1st-order Volterra operator of the equalizer has to be the inverse of the LED's 1st-order Volterra operator, i.e.

$$\mathbf{K}_1 = \mathbf{H}_1^{-1}. \quad (6.12)$$

In the frequency domain this translates to the well-known inverse of

$$K_1(\omega_1) = \frac{1}{H_1(\omega_1)}. \quad (6.13)$$

Equation (6.11) together with Eq. (6.9) gives for the 2nd-order Volterra operator of the

equalizer

$$\begin{aligned}
 \mathbf{K}_2 \mathbf{H}_1 &= -\mathbf{K}_1 \mathbf{H}_2 \\
 \mathbf{K}_2 \mathbf{H}_1 \mathbf{H}_1^{-1} &= -\mathbf{K}_1 \mathbf{H}_2 \mathbf{H}_1^{-1} \\
 \mathbf{K}_2 &= -\mathbf{K}_1 \mathbf{H}_2 \mathbf{H}_1^{-1} \\
 \mathbf{K}_2 &= -\mathbf{H}_1^{-1} \mathbf{H}_2 \mathbf{H}_1^{-1}.
 \end{aligned} \tag{6.14}$$

With Eq. (6.12), Eq. (6.14) may be re-written as

$$\mathbf{K}_2 = -\mathbf{K}_1 [\mathbf{H}_2 [\mathbf{K}_1]]. \tag{6.15}$$

Equation (6.15) states that the output signal of \mathbf{K}_2 is obtained by using the output of \mathbf{K}_1 as the input of \mathbf{H}_2 , followed by an application of $-\mathbf{K}_1$ on the output of \mathbf{H}_2 . The operator \mathbf{K}_2 given by Eq. (6.15) may be derived in the frequency domain in terms of its Volterra kernel transform $\underline{K}_2(\omega_1, \omega_2)$. With the knowledge that the operator \mathbf{H}_2 performs for a twotone excitation a frequency translation from the two input frequencies ω_1, ω_2 to the intermodulation frequency $\omega_{\text{IM}} = \omega_1 + \omega_2$, as derived with Eqs. (4.19) and (4.24) on page 79, Eq. (6.15) translates into the frequency domain as

$$\underline{K}_2(\omega_1, \omega_2) = -\underline{K}_1(\omega_1 + \omega_2) \cdot \underline{H}_2(\omega_1, \omega_2) \cdot \underline{K}_1(\omega_1) \cdot \underline{K}_1(\omega_2). \tag{6.16}$$

Equations (6.13) and (6.16) are the formulas to calculate the frequency response of a zero-forcing equalizer which is capable of equalizing the linear frequency response $\underline{H}_1(\omega_1)$ and nonlinear frequency response $\underline{H}_2(\omega_1, \omega_2)$ of the LED. This equalizer is only dependent on the driving and device parameters of the LED model given by Eqs. (5.1) and (5.2) on page 93.

The realization of this equalizer in form of an FIR filter structure is straightforward, as described in the previous chapter. That is, the filter coefficients are obtained by applying an inverse FFT on Eq. (6.13) and a 2D inverse FFT on Eq. (6.16) to obtain $k_1(\tau_1)$ and $k_2(\tau_1, \tau_2)$. Where the filter coefficients of the 2nd-order part of the equalizer are again given as $k_2(\tau_1, \tau_2)/2$, as stated earlier. The implementation of $k_2(\tau_1, \tau_2)$ may be realized with the matrix form shown in Fig. 6.4.

With the LED's frequency response given by Eqs. (5.1) and (5.2) on page 93, the frequency domain representation of the equalizer may be derived as

$$\begin{aligned}
 K_1(\omega_1) &= \frac{1}{\underline{H}_1(\omega)} = \frac{q}{\eta_{\text{extraction}} E_{\text{ph}}} \left[j \frac{\omega_1}{\omega_c} + 1 \right] \\
 &= A_1 \cdot \left[j \frac{\omega_1}{\omega_c} + 1 \right]
 \end{aligned} \tag{6.17}$$

6. Applications in LED-based Communication

and

$$\begin{aligned}
\underline{K}_2(\omega_1, \omega_2) &= - \underline{K}_1(\omega_1 + \omega_2) \cdot \underline{H}_2(\omega_1, \omega_2) \cdot \underline{K}_1(\omega_1) \cdot \underline{K}_1(\omega_2) \\
&= - A_1 \underbrace{\left[j \frac{\omega_1 + \omega_2}{\omega_c} + 1 \right]}_{K_1(\omega_1 + \omega_2)} \cdot \\
&\quad \underbrace{A_2 \frac{1}{j \frac{\omega_1}{\omega_c} + 1} \cdot \frac{1}{j \frac{\omega_2}{\omega_c} + 1} \cdot \frac{1}{1 - j \frac{\omega_c}{\omega_1 + \omega_2}}}_{H_2(\omega_1, \omega_2)} \cdot \underbrace{A_1 \left[j \frac{\omega_1}{\omega_c} + 1 \right]}_{K_1(\omega_1)} \cdot \underbrace{A_1 \left[j \frac{\omega_2}{\omega_c} + 1 \right]}_{K_1(\omega_2)} \\
&= - A_1^3 A_2 \left(j \frac{\omega_1 + \omega_2}{\omega_c} + 1 \right) \cdot \left(\frac{1}{1 - j \frac{\omega_c}{\omega_1 + \omega_2}} \right), \tag{6.18}
\end{aligned}$$

where

$$A_1 = \frac{q}{\eta_{\text{extraction}} E_{\text{ph}}}, \quad A_2 = \frac{\eta_{\text{extraction}} E_{\text{ph}}}{2V_{\text{active}} B [qN_0]^2}. \tag{6.19}$$

It is seen that $\underline{K}_2(\omega_1, \omega_2)$ is only dependent on the intermodulation frequency $\omega_{\text{IM}} = \omega_1 + \omega_2$, and not on the input frequencies ω_1, ω_2 .

For this equalizer based on the theory of the p^{th} -order inverse two important characteristics are noted:

1. From Eq. (6.15) it is seen that \mathbf{K}_2 is stable and causal if \mathbf{K}_1 and \mathbf{H}_2 are stable and causal.
2. It may be shown that the p^{th} -order post-inverse and pre-inverse are identical [64]. That is, the nonlinear system and its p^{th} -order inverse may be interchanged in the tandem connection of Fig. 6.5. Higher-order terms ($n > p$), however, will generally not be the same, but nonlinear orders $n \leq p$ are equalized.

Often, a stable and causal inverse of \mathbf{H}_1 does not exist. In such cases, however, the requirements concerning the stability and causality may be relaxed by allowing slight deviations from the perfect equalization given in Eq. (6.6). For example, causality may usually be achieved by allowing the output signal of \mathbf{Q} to be a delayed version of the input signal $x(t)$.

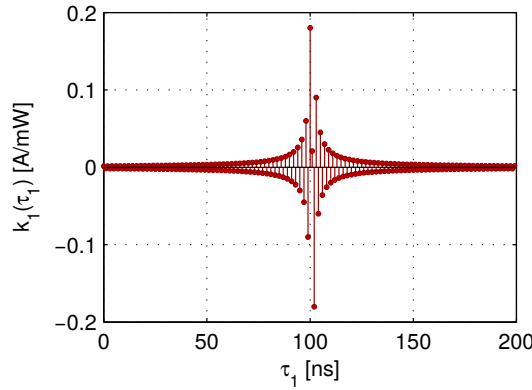
6.2.1. Exemplary Applications

The nonlinear zero-forcing equalizer is exemplarily tested for two applications:

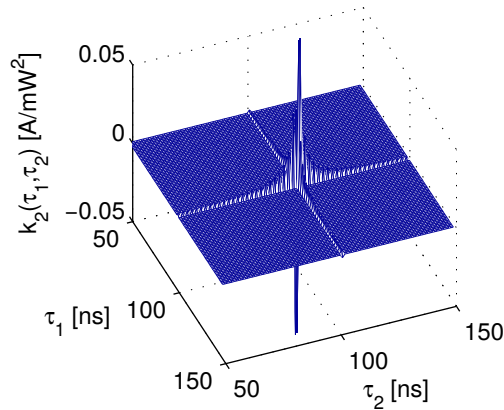
1. Suppression of 2nd-order harmonics (HD2) for a onetone excitation of the LED
2. Post equalization of a multilevel PAM transmit signal.

The equalizer is tested in a simulation environment where the LED is modelled by the carrier density rate equation introduced in Ch. 2.7. Using this physical simulation model, rather than lab measurements allows perfect isolation of the linear and nonlinear signal impairments induced by the LED without being affected by other components such as a signal generator or a photo detector (PD). Further, the impact of noise can be treated separately.

The equalizer used in the subsequent investigations is built up based on the device parameters of Table. 3.1 on page 46, but again with the fitted recombination coefficient of $B = 8.47 \cdot 10^{-11} \frac{\text{cm}^3}{\text{s}}$. The corresponding time domain Volterra kernels are obtained by applying an inverse FFT on $\underline{K}_1(\omega_1)$ and an inverse 2D FFT on $\underline{K}_2(\omega_1, \omega_2)$. The results with a sampling frequency of 1 GHz are shown in Fig. 6.7. In order to approximate a causal system inverse, a delay of 100 ns was here introduced.



(a) $k_1(\tau_1)$



(b) $k_2(\tau_1, \tau_2)$ (extract of 100 ns \times 100 ns)

Figure 6.7.: Volterra kernels of the 2nd-order inverse.

Suppression of HD2 for a Onetone Excitation

In Ch. 3.3, higher-order harmonics at the output of the LED were evaluated for both measurements and numerical simulations of the carrier density rate equation model. The maximum observed HD2 were in the order of -25 dBc (cf. Fig. 3.15 on page 66). Good agreement was found between measurements and simulations, where the simulations overestimated the HD2 by a nearly constant factor of about 3 dB. This is most likely due to the fact that the device parameters are estimations, cf. Eq. (6.4) on page 106. But such a correction factor could easily be incorporated into the filter taps.

The performance of the equalizer is evaluated by comparing the higher-order harmonics at the output of the equalizer with the unequalized ones of Fig. 3.15. It should be noted that the derived equalizer achieves perfect equalization only if it is tandem connected to the underlying system model \mathbf{H} from which it is derived, for example as used in the simulation setup shown in Fig. 6.2. When the equalizer is applied to the output of the numerically simulated carrier density rate equation, non-perfect equalization is to be expected, just as it is to be expected in a real measurement scenario.

The corresponding simulational setup is shown in Fig. 6.8, the results for HD2, HD3, and HD4 at the output of the equalizer are shown in Fig. 6.9, along with the unequalized results of Fig. 3.15.

Comparing the equalized and unequalized results shows that the 2nd harmonic (HD2) is attenuated by the equalizer by about ≥ 10 dB. The 3rd and 4th harmonics are not suppressed, which is in agreement with the theory, since, by definition, the equalizer is the 2nd-order inverse of the LED. In fact, HD3 and HD4 are enhanced compared to the unequalized case. However, HD3 and HD4 are still below -30 dBc, and hence it may be summarized that the equalizer based on the 2nd-order inverse Volterra system effectively suppresses the observed higher-order harmonics by about ≥ 8 dB.

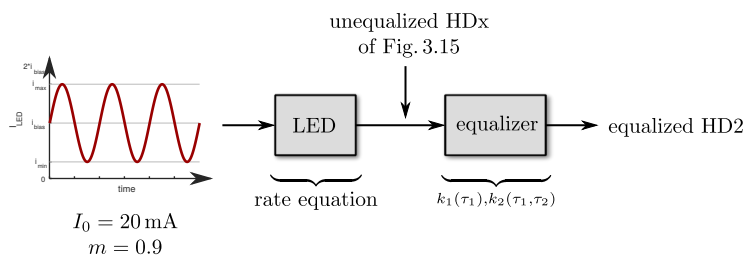


Figure 6.8.: Equalization of HD2 for a onetone excitation of the LED.

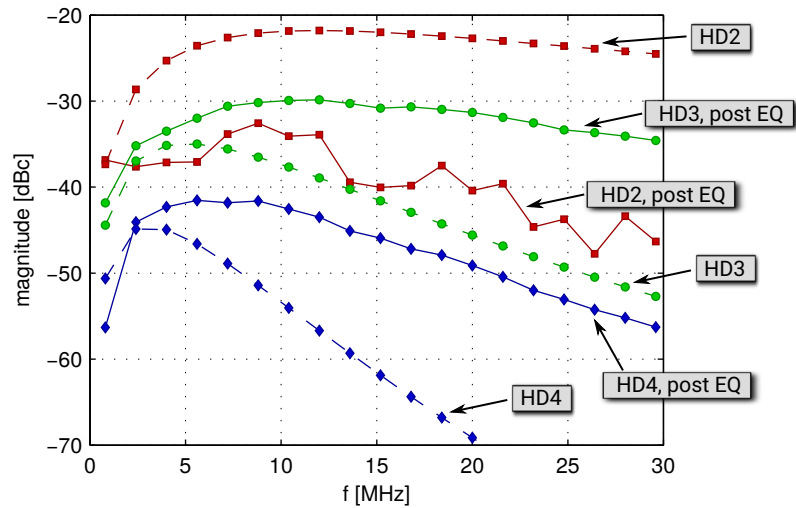


Figure 6.9.: Higher-order harmonics at the output the equalizer.

Equalization with Reduced Complexity The coefficients of Fig. 6.7b show the interesting characteristic that only one column and one line of the matrix have significant magnitudes. All other coefficients of the matrix are virtually zero. This gives rise to the question whether the equalizer may work at similar performance with a drastically reduced filter tap number of $k_2(\tau_1, \tau_2)$.

Figure 6.10 shows the obtained HD2, HD3, and HD4 at the output of the equalizer when all coefficients in $k_2(\tau_1, \tau_2)$ are set to zero, except for the center line and column. It is seen that the performance is indeed the same as the one obtained with the full number of coefficients shown in Fig. 6.9.

That is, the filter structure based on the 2nd-order inverse of the LED allows a drastic reduction of filter taps (and hence also multipliers) from N^2 to $2N - 1$ (where N is the number of filter taps required by the nonlinear memory length) without sacrificing performance.

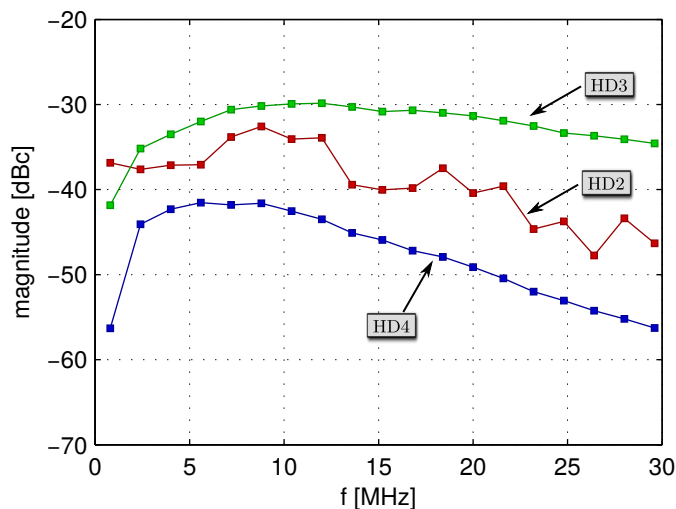


Figure 6.10.: Higher-order harmonics at the output the equalizer with a reduced number of coefficients.

Equalization of a Multilevel PAM Signal

The performance evaluations of the equalizer are completed with an exemplary application to a multilevel PAM transmit signal. The simulational testbed for a back-to-back transmission setup is depicted in Fig. 6.11.

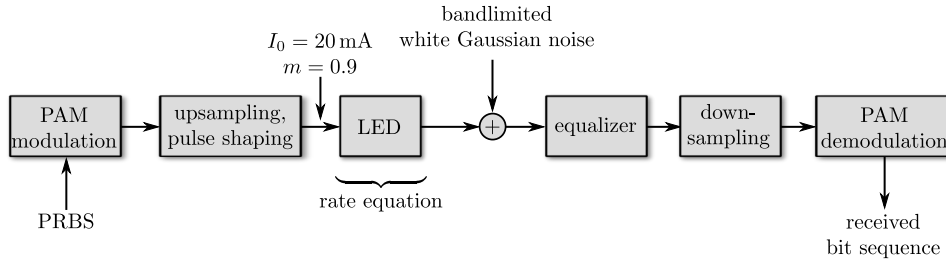


Figure 6.11.: Simulational setup for the equalization of an 8-PAM transmit signal.

The transmit signal is composed of a PRBS of length 2^{12} which is repeated several times to yield an overall length of $> 10^5$ bits. The bit sequence is 8-PAM modulated by mapping $\log_2(8) = 3$ bits into each PAM symbol with gray coding. The PAM sequence is upsampled to 1 GS/s and pulse-shaped with a raised cosine pulse shaping filter with a rolloff of 0.8.

The LED is modulated with the 8-PAM signal, biased at 20 mA with a modulation index of $m = 0.9$. The output signal of the LED experiences additive white Gaussian noise which is bandlimited to 2-baudrate. This simulates a noisy PD.

The noisy receive signal is then fed to the zero-forcing equalizer. The output of the equalizer is downsampled and 8-PAM demodulated to obtain the received bit sequence.

The system performance is evaluated in terms of bit error ratio (BER) versus received SNR. The equalizer based on the 2nd-order system inverse is compared to a linear equalizer which uses only $k_1(\tau_1)$ for equalization. Based on the results above, the 2nd-order nonlinear equalizer uses the reduced number of coefficients of $k_2(\tau_1, \tau_2)$, that is, the number of coefficients in the nonlinear part is only $2 \cdot N_{\text{lin}} - 1$, where N_{lin} is the number of coefficients in the linear part. The bitrate is chosen to be 300 MBit/s, which corresponds to a modulation bandwidth of about 90 MHz, i.e. a factor of about 4.5 of the LED's -3dB cutoff frequency. For each SNR value, 10 independent simulations are performed to calculate an average BER.

The performances of the two equalizers are shown in Fig. 6.12. It is seen that the equalization of the LED's 2nd-order nonlinearities based on the system inverse drastically improves the system performance. In fact, when only linear signal impairments are compensated, the system basically fails with an error floor at around $\text{BER} = 10^{-2}$. This demonstrates that LED nonlinearities may affect the system margin by several dB, depending on the underlying modulation format and bitrate. An equalizer based on a Volterra series approach is a powerful device in communication systems, and with the device model derived in this thesis, a Volterra series based equalizer could be realized which needs only a fraction of the regular number of filter taps at the same performance.

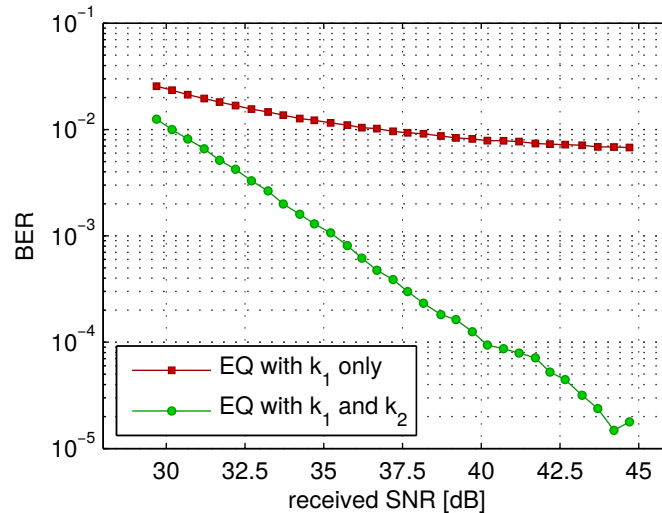


Figure 6.12.: System performance with and without equalization of LED nonlinearities.

Optimizing the Equalizer Performance It was elucidated in Ch. 5.1 that the accuracy of the analytic device model may be improved by incorporating a correction factor α into the calculation of N_0 (cf. Eq. (5.5) on page 96).

As a final investigation, the impact of such a correction factor on the equalizer's performance is investigated. It was empirically found that values of about $0.9 \leq \alpha < 1$ yield the best accuracy of the device model. Figure 6.13 compares the equalizer performance for $\alpha = 1$ (used in the previous simulations), $\alpha = 0.95$, and $\alpha = 0.9$.

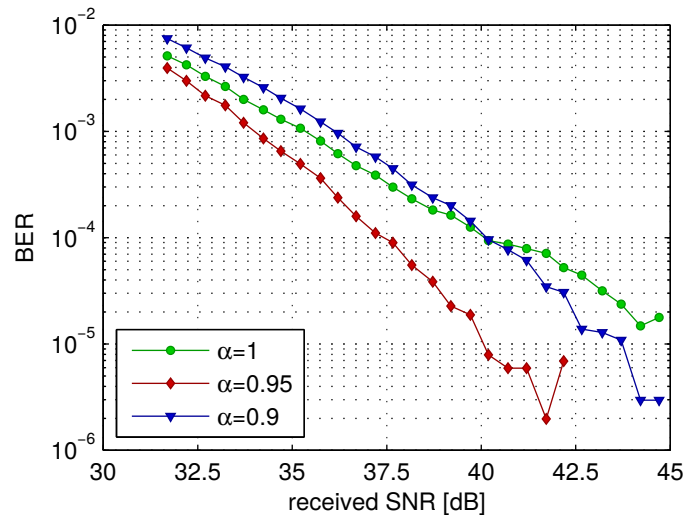


Figure 6.13.: System performance using different LED model correction factors.

It is observed that an α slightly below 1 does indeed result in an improved accuracy of the equalizer. The performance improvement compared to $\alpha = 1$ is about 2 dB at $\text{BER} = 10^{-3}$. It should be pointed out that further improvements are likely with a more comprehensive study of this parameter. For example, taking into consideration the spectral shaping of the transmit and/or receive signals may be beneficial in a real optimization procedure. An adaptive equalization could then use the model Eqs. (5.1)

6. Applications in LED-based Communication

and (5.2) on page 93, along with Eq. (5.5) to calculate and optimize the filter taps, for example in a minimum MSE sense. However, even without detailed optimizations from an information-theoretic point of view, the equalizer derived from the analytic LED model demonstrates an impressive performance improvement for LED-based communication systems.

Without such an optimization procedure, an adaptive equalizer based on the device model of Eqs. (5.1) and (5.2) will basically require three fitting parameters: One parameter to estimate the magnitude of \underline{H}_1 , a second parameter to estimate the magnitude of \underline{H}_2 , and a third parameter to estimate the cutoff frequency ω_c , which is found in both \underline{H}_1 and \underline{H}_2 . Here, the first two parameters would be realized with one multiplier stage at the input of each signal branch of the equalizer (cf. Fig. 6.5 on page 107).

7. Conclusion

The thesis at hand investigated the characteristics of nonlinear distortions occurring in the electro-optical (E/O) conversion of directly modulated communication LEDs.

These investigations were motivated by the fact that nonlinear signal distortions caused by the LED were shown to have a strong detrimental impact on the performance of LED-based communication systems. Gaining insight into the dominant physical origins and finding a suitable mathematical approximation which describes the observed nonlinear behaviour is therefore of great importance to optimize the performance of next-generation LED communication systems.

Based on a well-accepted carrier density rate equation model, a simplified mathematical description was derived in a closed form which describes the 2nd-order nonlinearities of the LED's E/O conversion. This mathematical model was applied in the frequency domain to predict the frequency dependence of the 2nd-order intermodulation products (IM2). It was found that the frequency response of the IM2 is mathematically connected to the LED's frequency response by a common characteristic frequency. A comparison of the model with measurements of commercially available LEDs which are designed for POF communication showed very good agreement.

Using the theory of the Volterra series, the device model was transformed into the time domain. This time domain representation may be implemented in a digital filter topology in a straightforward way to give a nonlinear simulation model of the LED. Such a time domain model may be conveniently incorporated into simulation testbeds of communication systems to give realistic predictions of the system performance.

Further, a nonlinear system inverse was analytically derived. This may be used as a time domain pre or post equalizer to compensate for the 2nd-order nonlinearities caused by the LED. It was found that this equalizer may be implemented in a reduced-complexity topology without performance degradation. Due to the above-mentioned interconnection between the linear frequency response and nonlinear frequency response, application of the ideal nonlinear equalizer (in the sense of the 2nd-order Volterra series inverse), could, for example, be implemented by estimating the linear frequency response by an adaptive equalizer and using this result to calculate the coefficients of the nonlinear part.

The results obtained in this work hold for LEDs which are driven under high excitation in a regime where nonradiative recombination processes are negligible. That is, where the static P -versus- I curve is sufficiently linear. Several aspects found in this work are also a valuable information for a nonlinear modelling of other types of LEDs.

The model is based on a carrier density rate equation which neglects spatially non-uniform carrier distributions. The results showed an impressive accuracy of this simplified modelling approach, even for the third harmonics generated in the LED. This suggests that detailed information of the carrier dynamics, such as drift and diffusion processes, is not required when the LED is treated from a communication-point-of-view. It is further expected that the nonlinearities found in this work represent a lower

7. Conclusion

bound of nonlinearities when an LED is driven in a regime of high excitation, as is usually the case for modern DH and QW devices.

A. The Potential Impact of Doping

The model presented in this thesis used the assumption of an ideal regime of high excitation where the radiative recombination has the form

$$R_{\text{rad}} = Bn^2. \quad (\text{A.1})$$

The verification of both $\underline{H}_1(\omega_1)$ and $\underline{H}_2(\omega_1, \omega_2)$, as presented in Ch. 5, proved good agreement with both numerical simulations and lab measurements.

In this chapter, it is evaluated whether the nonlinear LED device model with its characteristic functions $\underline{H}_1(\omega_1)$ and $\underline{H}_2(\omega_1, \omega_2)$ also hold for the case when doping of the active region is present. Then, with an ionized doping concentration N (in units of $1/\text{cm}^3$), the radiative recombination term is of the form

$$R_{\text{rad}} = Bn(n + N) = Bn^2 + BNn. \quad (\text{A.2})$$

That is, an additional recombination term which is linear with n is present. In this case, the device model equations (2.70) and (2.71) on page 43 are re-written as

$$\frac{dn}{dt} = \frac{i(t)}{qV_{\text{active}}} - Bn^2 - BNn \quad (\text{A.3})$$

and

$$p_{\text{opt}}(t) = \eta_{\text{extraction}} E_{\text{ph}} V_{\text{active}} \left[B [n(t)]^2 + BNn(t) \right]. \quad (\text{A.4})$$

In the following, the impact of N on the linear frequency response $\underline{H}_1(\omega_1)$ and the nonlinear frequency response $\underline{H}_2(\omega_1, \omega_2)$ of the LED is evaluated. The derivations are conducted in the same manner as presented in Chapters 3.2 and 4, respectively.

The LED device model of Fig. 4.5 on page 83 is extended as shown in Fig. A.1 with

$$i(t) = i_{\text{LED}}(t) = \underbrace{qV_{\text{active}} \frac{dn}{dt}}_{i_a(t)} + \underbrace{qV_{\text{active}} Bn^2}_{i_b(t)} + \underbrace{qV_{\text{active}} BNn}_{i_c(t)}. \quad (\text{A.5})$$

A. The Potential Impact of Doping

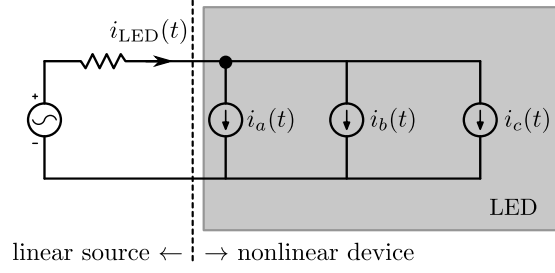


Figure A.1.: Equivalent circuit of the LED according to the extended device model.

A.1. Linear Frequency Response

The electrical input current signal is again assumed to be given by a biased onetone signal of Eq. (3.5) on page 53. Likewise, the carrier density $n(t)$ and optical output power $p_{\text{opt}}(t)$ are given by Eqs. (3.6) and (3.7), respectively.

For the extended model of Eq. (A.4), Eq. (3.8) on page 54 translates into

$$\begin{aligned}
 p_{\text{opt}}(t) &= A_P \cdot [n(t)]^2 + Nn(t)] \\
 &= A_P \cdot [N_0 + n_1(t)]^2 + NN_0 + Nn_1(t) \\
 &= A_P \cdot [N_0^2 + 2N_0n_1(t) + [n_1(t)]^2 + NN_0 + Nn_1(t)] \\
 &= A_P \cdot [N_0^2 + NN_0 + (2N_0 + N)n_1(t) + [n_1(t)]^2], \tag{A.6}
 \end{aligned}$$

with $A_P = \eta_{\text{extraction}} E_{\text{ph}} V_{\text{active}} B$. This gives the output signal component at ω_1 in equivalence to Eq. (3.9) on page 54 as

$$\frac{P_1}{2} = A_P \cdot (2N_0 + N) \frac{N_1}{2}. \tag{A.7}$$

To derive N_0 and N_1 , the right-hand side of Eq. (A.3) is re-written in equivalence to Eq. (3.11) on page 54 as

$$\begin{aligned}
 \frac{i(t)}{qV_{\text{active}}} - B[n(t)]^2 &= \frac{I_0 + \frac{I_1}{2}e^{j\omega_1 t} + \frac{I_1^*}{2}e^{-j\omega_1 t}}{qV_{\text{active}}} \\
 &- B \cdot \left[N_0^2 + 2N_0 \left[\frac{N_1}{2}e^{j\omega_1 t} + \frac{N_1^*}{2}e^{-j\omega_1 t} \right] + \left[\frac{N_1}{2}e^{j\omega_1 t} + \frac{N_1^*}{2}e^{-j\omega_1 t} \right]^2 \right] \\
 &- B \cdot \left[NN_0 + N \frac{N_1}{2}e^{j\omega_1 t} + N \frac{N_1^*}{2}e^{-j\omega_1 t} \right]. \tag{A.8}
 \end{aligned}$$

Equation (A.8) contains tones at frequencies $0, \pm\omega_1, \pm 2\omega_1$. The left-hand side of Eq. (A.3) is given by Eq. (3.10) on page 54, i.e.

$$\frac{d}{dt}n(t) = \frac{N_1}{2}j\omega_1 e^{j\omega_1 t} - \frac{N_1^*}{2}j\omega_1 e^{-j\omega_1 t}. \tag{A.9}$$

For small-signal modulation, separation of the frequency components at DC in Eqs. (A.8) and (A.9) gives

$$0 = \frac{I_0}{qV_{\text{active}}} - BN_0^2 - BNN_0, \quad (\text{A.10})$$

with the two solutions for the carrier density N_0 of

$$N_{0,a/b} = -\frac{N}{2} \pm \sqrt{\left(\frac{N}{2}\right)^2 + \frac{I_0}{qV_{\text{active}}B}}.$$

As N and N_0 must be positive, this leaves

$$N_0 = -\frac{N}{2} + \sqrt{\left(\frac{N}{2}\right)^2 + \frac{I_0}{qV_{\text{active}}B}}. \quad (\text{A.11})$$

Equation (A.11) is the equivalent to Eq. (3.13) on page 55 when an additional radiative recombination term caused by a doping concentration N is present.

A comparison of N_0 versus LED input bias is shown in Fig. (A.2) using numerical simulations, along with the verification of Eq. (A.11). It is seen that the presence of an additional radiative recombination term lowers the static carrier density N_0 compared to the purely quadratic recombination of Eq. (2.70) on page 43.

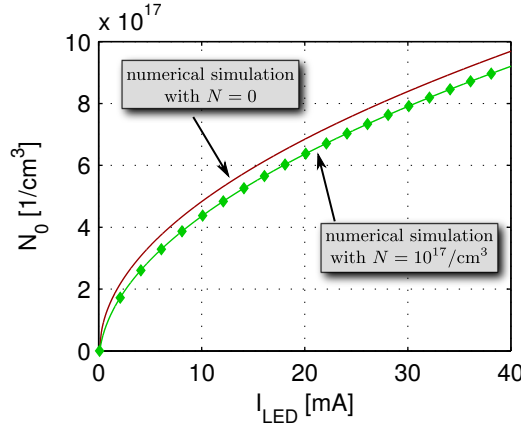


Figure A.2.: 3D carrier density versus electrical input current for the device model Eqs. (2.70) and (A.3) with the parameters of Table 3.7 on page 65 and $B = 8.47 \cdot 10^{-11} \text{cm}^3/\text{s}$ (markers: calculation with Eq. (A.11)).

The complex-valued term \underline{N}_1 , which contains the magnitude and phase of $n_1(t)$ (cf. Eq. (3.6) on page 53) is derived in analogy to Eq. (3.14) on page 55 as

$$\begin{aligned} j\omega_1 \frac{\underline{N}_1}{2} e^{j\omega_1 t} &= \frac{\underline{I}_1}{2} \frac{e^{j\omega_1 t}}{qV_{\text{active}}} - B(2N_0 + N) \frac{\underline{N}_1}{2} e^{j\omega_1 t} \\ j\omega_1 \underline{N}_1 &= \frac{\underline{I}_1}{qV_{\text{active}}} - B(2N_0 + N) \underline{N}_1. \end{aligned} \quad (\text{A.12})$$

A. The Potential Impact of Doping

Re-arranging yields

$$\begin{aligned} \underline{N}_1(\omega_1) &= \frac{\underline{I}_1}{qV_{\text{active}}} \cdot \frac{1}{j\omega_1 + B(2N_0 + N)} \\ &= \frac{\underline{I}_1}{qV_{\text{active}}} \cdot \frac{1}{B(2N_0 + N)} \cdot \frac{1}{j\frac{\omega_1}{B(2N_0 + N)} + 1}. \end{aligned} \quad (\text{A.13})$$

Putting Eqs. (A.11) and (A.13) into Eq. (A.7) gives

$$\begin{aligned} \frac{\underline{P}_1(\omega_1)}{2} &= A_P \cdot \frac{(2N_0 + N)}{2} \frac{\underline{I}_1}{qV_{\text{active}}} \cdot \frac{1}{B(2N_0 + N)} \cdot \frac{1}{j\frac{\omega_1}{B(2N_0 + N)} + 1} \\ \underline{P}_1(\omega_1) &= A_P \cdot \frac{\underline{I}_1}{qV_{\text{active}}B} \cdot \frac{1}{j\frac{\omega_1}{B(2N_0 + N)} + 1}. \end{aligned} \quad (\text{A.14})$$

With the definition of the frequency response of Eq. (3.17) on page 55, this yields

$$\underline{H}_{1,\text{with doping}}(\omega_1) = \frac{\underline{P}_1(\omega_1)}{\underline{I}_1(\omega_1)} = \frac{A_P}{qV_{\text{active}}B} \cdot \frac{1}{j\frac{\omega_1}{B(2N_0 + N)} + 1}. \quad (\text{A.15})$$

Comparing Eqs. (3.18) on page 55 and (A.15) shows that the analytic LED model predicts a 1st-order lowpass characteristic, with and without a doping term. It is further seen, that with the small-signal assumption, the magnitude response is not affected by N . With doping incorporated into the model, the cutoff frequency is given as

$$\omega_{c,\text{with doping}} = B(2N_0 + N), \quad (\text{A.16})$$

and with Eq. (A.11) and Eq. (3.13) on page 55

$$\omega_{c,\text{with doping}} = B \left[-N + 2\sqrt{\left(\frac{N}{2}\right)^2 + \frac{I_0}{qV_{\text{active}}B}} + N \right] = 2B\sqrt{\left(\frac{N}{2}\right)^2 + N_{0,\text{no doping}}^2}. \quad (\text{A.17})$$

That is, the model predicts a (slightly) increased bandwidth, compared to the undoped case with ω_c given by Eq. (3.20) on page 56. The corresponding input bias dependence of the cutoff frequency is plotted in Fig. A.3.

It is seen that the square-root shaped curve obtained without doping gets more linearized when an increased doping is present.

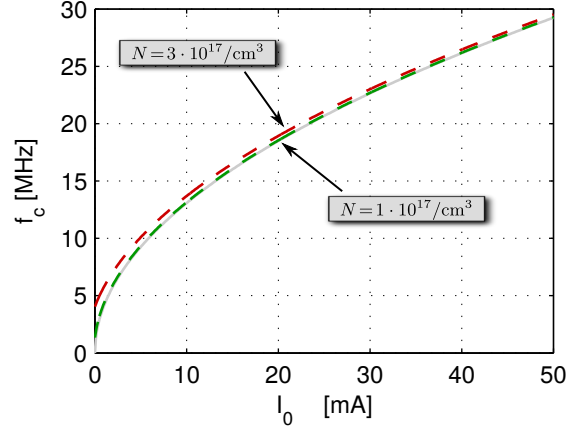


Figure A.3.: Calculated -3 dB cutoff frequency versus input bias when recombination due to a concentration N of ionized dopants is present (gray curve: without doping).

A.2. Nonlinear Frequency Response

The frequency response $H_2(\omega_1, \omega_2)$ of the IM2 is derived in analogy to the derivation presented in Ch. 4.4 on page 83ff.

The electrical input current is the biased twotone signal given by Eqs. (4.27) to (4.30) on page 83. The output signal $p_{\text{IM}}(t)$ containing the two intermodulation tones is described by Eq. (4.31) on page 84. Similarly, the signal $n(t)$ describing the 3D carrier density is assumed to be a superposition of a finite number of tones, as described by Eqs. (4.32) and (4.33).

When recombination due to doping of the active region is also present, the optical output signal is given by Eq. (A.4). The tones in $n(t)$ which are expected to noticeably contribute to the generation of $p_{\text{IM}}(t)$ are found as done in Ch. 4.4.

The first term $B[n(t)]^2$ on the right-hand side of Eq. (A.4) is the same as found in Eq. (2.71) on page 43. Hence, it will contribute to the generation of $p_{\text{IM}}(t)$ with the three tones $n_1(t)$, $n_2(t)$ and $n_{\text{IM}}(t)$ and the bias N_0 , as discussed in Ch 4.4, which lead to Eq. (4.35) on page 85.

The additional term $BNn(t)$ on the right-hand side of Eq. (A.4) is linear with n , and hence here only the intermodulation tone $n_{\text{IM}}(t)$ contained in $n(t)$ can contribute to the generation of $p_{\text{IM}}(t)$. As a result, the tones which must be considered for the calculation of $p_{\text{opt}}(t)$ are the same as for the LED device model without doping, i.e. in analogy to Eq. (4.35) on page 85

$$p_{\text{opt}}(t) = A_P \left[[N_0 + n_1(t) + n_2(t) + n_{\text{IM}}(t)]^2 + N [N_0 + n_1(t) + n_2(t) + n_{\text{IM}}(t)] \right], \quad (\text{A.18})$$

with $A_P = \eta_{\text{extraction}} E_{\text{ph}} V_{\text{active}} B$. With the definition of $n_{\text{IM}}(t)$ of Eq. (4.34) on page 84, this gives for the intermodulation signal at the output of the LED

A. The Potential Impact of Doping

$$\begin{aligned}
p_{\text{IM}}(t) &= p_{\text{IM,pos}}(t) + p_{\text{IM,neg}}(t) = A_P [(2N_0 + N)n_{\text{IM}}(t) + 2n_1(t)n_2(t)] \\
&= A_P \left(N_0 + \frac{N}{2} \right) \\
&\quad \cdot [N_{\text{IM,pos}} e^{j\omega_{\text{IM,pos}} t} + N_{\text{IM,pos}}^* e^{-j\omega_{\text{IM,pos}} t} + N_{\text{IM,neg}} e^{j\omega_{\text{IM,neg}} t} + N_{\text{IM,neg}}^* e^{-j\omega_{\text{IM,neg}} t}] \\
&\quad + \frac{A_P}{2} [N_1 e^{j\omega_1 t} + N_1^* e^{-j\omega_1 t}] \cdot [N_2 e^{j\omega_2 t} + N_2^* e^{-j\omega_2 t}] \\
&= A_P \left[\left(N_0 + \frac{N}{2} \right) N_{\text{IM,pos}} + \frac{N_1 N_2}{2} \right] e^{j\omega_{\text{IM,pos}} t} \\
&\quad + A_P \left[\left(N_0 + \frac{N}{2} \right) N_{\text{IM,pos}}^* + \frac{N_1^* N_2^*}{2} \right] e^{-j\omega_{\text{IM,pos}} t} \\
&\quad + A_P \left[\left(N_0 + \frac{N}{2} \right) N_{\text{IM,neg}} + \frac{N_1 N_2^*}{2} \right] e^{j\omega_{\text{IM,neg}} t} \\
&\quad + A_P \left[\left(N_0 + \frac{N}{2} \right) N_{\text{IM,neg}}^* + \frac{N_1^* N_2}{2} \right] e^{-j\omega_{\text{IM,neg}} t}. \tag{A.19}
\end{aligned}$$

Equation (A.19) is the equivalent to Eq. (4.37) on page 85. To derive $N_{\text{IM,pos}}$ and $N_{\text{IM,neg}}$, the harmonic balance approach is applied to Eq. (A.5) at the frequencies $\pm\omega_{\text{IM,pos}}$ and $\pm\omega_{\text{IM,neg}}$.

As the input current does not contain the frequencies $\pm\omega_{\text{IM,pos}}$ and $\pm\omega_{\text{IM,neg}}$, the left-hand side of Eq. (A.5) is zero, and in analogy to Eqs. (4.38) and (4.39) on page 86 one obtains

$$\begin{aligned}
0 &= qV_{\text{active}} j\omega_{\text{IM,pos}} \frac{N_{\text{IM,pos}}}{2} e^{j\omega_{\text{IM,pos}} t} \\
&\quad + qV_{\text{active}} B \left(\frac{N_1 N_2}{2} e^{j(\omega_1 + \omega_2)t} + N_0 N_{\text{IM,pos}} e^{j\omega_{\text{IM,pos}} t} \right) \\
&\quad + qV_{\text{active}} B N \frac{N_{\text{IM,pos}}}{2} e^{j\omega_{\text{IM,pos}} t} \\
&= j\omega_{\text{IM,pos}} \frac{N_{\text{IM,pos}}}{2} + B \left[\frac{N_1 N_2}{2} + N_{\text{IM,pos}} \left(N_0 + \frac{N}{2} \right) \right] \tag{A.20}
\end{aligned}$$

and

$$\begin{aligned}
0 &= qV_{\text{active}} j\omega_{\text{IM,neg}} \frac{N_{\text{IM,neg}}}{2} e^{j\omega_{\text{IM,neg}} t} \\
&\quad + qV_{\text{active}} B \left(\frac{N_1 N_2^*}{2} e^{j(\omega_1 - \omega_2)t} + N_0 N_{\text{IM,neg}} e^{j\omega_{\text{IM,neg}} t} \right) \\
&\quad + qV_{\text{active}} B N \frac{N_{\text{IM,neg}}}{2} e^{j\omega_{\text{IM,neg}} t} \\
&= j\omega_{\text{IM,neg}} \frac{N_{\text{IM,neg}}}{2} + B \left[\frac{N_1 N_2^*}{2} + N_{\text{IM,neg}} \left(N_0 + \frac{N}{2} \right) \right]. \tag{A.21}
\end{aligned}$$

Solving for $N_{\text{IM,pos}}(\omega_1, \omega_2)$ and $N_{\text{IM,neg}}(\omega_1, \omega_2)$ yields

$$\underline{N}_{\text{IM,pos}}(\omega_1, \omega_2) = -\frac{BN_1N_2}{j(\omega_1 + \omega_2) + B(2N_0 + N)}, \quad \omega_1, \omega_2 \geq 0 \quad (\text{A.22})$$

$$\underline{N}_{\text{IM,neg}}(\omega_1, \omega_2) = -\frac{BN_1N_2^*}{j(\omega_1 - \omega_2) + B(2N_0 + N)}, \quad \omega_1, \omega_2 \geq 0. \quad (\text{A.23})$$

And for the complex-conjugates

$$N_{\text{IM,pos}}^*(\omega_1, \omega_2) = -\frac{BN_1^*N_2^*}{-j(\omega_1 + \omega_2) + B(2N_0 + N)}, \quad \omega_1, \omega_2 \geq 0 \quad (\text{A.24})$$

$$N_{\text{IM,neg}}^*(\omega_1, \omega_2) = -\frac{BN_1^*N_2}{-j(\omega_1 - \omega_2) + B(2N_0 + N)}, \quad \omega_1, \omega_2 \geq 0. \quad (\text{A.25})$$

Or, in analogy to Eq. (4.45) on page 87

$$\underline{N}_{\text{IM}}(\omega_1, \omega_2) := -\frac{BN_1N_2}{j(\omega_1 + \omega_2) + B(2N_0 + N)}, \quad (\omega_1, \omega_2 \text{ positive and negative}). \quad (\text{A.26})$$

Equation (A.19) may then be re-written as

$$\begin{aligned} p_{\text{IM}}(t) = & A_P \left[\left(N_0 + \frac{N}{2} \right) \underline{N}_{\text{IM}}(\omega_1, \omega_2) + \frac{N_1N_2}{2} \right] e^{j(\omega_1 + \omega_2)t} \\ & + A_P \left[\left(N_0 + \frac{N}{2} \right) \underline{N}_{\text{IM}}(-\omega_1, -\omega_2) + \frac{N_1^*N_2^*}{2} \right] e^{j(-\omega_1 - \omega_2)t} \\ & + A_P \left[\left(N_0 + \frac{N}{2} \right) \underline{N}_{\text{IM}}(\omega_1, -\omega_2) + \frac{N_1N_2^*}{2} \right] e^{j(\omega_1 - \omega_2)t} \\ & + A_P \left[\left(N_0 + \frac{N}{2} \right) \underline{N}_{\text{IM}}(-\omega_1, \omega_2) + \frac{N_1^*N_2}{2} \right] e^{j(-\omega_1 + \omega_2)t}. \end{aligned} \quad (\text{A.27})$$

For $\underline{P}_{\text{IM}}(\omega_1, \omega_2)$, as introduced by Eq. (4.47) on page 88, this gives with $\underline{N}_{1/2}^*(\omega_{1/2}) = \underline{N}_{1/2}(-\omega_{1/2})$

A. The Potential Impact of Doping

$$\begin{aligned}
\frac{P_{\text{IM}}(\omega_1, \omega_2)}{2} &= A_P \left[\frac{N_1 N_2}{2} + \left(N_0 + \frac{N}{2} \right) N_{\text{IM}} \right] \\
&= A_P \left[\frac{N_1(\omega_1) N_2(\omega_2)}{2} - \frac{B \left(N_0 + \frac{N}{2} \right)}{j(\omega_1 + \omega_2) + B(2N_0 + N)} N_1(\omega_1) N_2(\omega_2) \right] \\
&= A_P \frac{N_1(\omega_1) N_2(\omega_2)}{2} \cdot \left[1 - \frac{B(2N_0 + N)}{j(\omega_1 + \omega_2) + B(2N_0 + N)} \right] \\
&= A_P \frac{N_1(\omega_1) N_2(\omega_2)}{2} \cdot \left[1 - \frac{1}{j \frac{\omega_1 + \omega_2}{B(2N_0 + N)} + 1} \right] \\
&= 2A_P \frac{N_1(\omega_1)}{2} \frac{N_2(\omega_2)}{2} \cdot \frac{1}{1 - j \frac{B(2N_0 + N)}{\omega_1 + \omega_2}} \quad (\omega_1, \omega_2 \text{ positive and negative}).
\end{aligned} \tag{A.28}$$

And, in analogy to Eq. (5.2) on page 93 for the frequency response of the IM2 (i.e. the 2nd-order Volterra kernel transform) using (A.13) and corresponding $N_2(\omega_2)$

$$\begin{aligned}
H_2(\omega_1, \omega_2) &= \frac{P_{\text{IM}}(\omega_1, \omega_2)/2}{\frac{I_1(\omega_1)}{2} \frac{I_2(\omega_2)}{2}} = 2A_P \frac{N_1(\omega_1) N_2(\omega_2)}{I_1(\omega_1) I_2(\omega_2)} \cdot \left(\frac{1}{1 - j \frac{B(2N_0 + N)}{\omega_1 + \omega_2}} \right) \\
&= \frac{2A_P}{(2qV_{\text{active}})^2} \cdot \frac{1}{[B(2N_0 + N)]^2} \cdot \frac{1}{j \frac{\omega_1}{B(2N_0 + N)} + 1} \cdot \frac{1}{j \frac{\omega_2}{B(2N_0 + N)} + 1} \cdot \frac{1}{1 - j \frac{B(2N_0 + N)}{\omega_1 + \omega_2}} \\
&= \frac{\eta_{\text{extraction}} E_{\text{ph}}}{2V_{\text{active}} B [q(2N_0 + N)]^2} \cdot \frac{1}{j \frac{\omega_1}{B(2N_0 + N)} + 1} \cdot \frac{1}{j \frac{\omega_2}{B(2N_0 + N)} + 1} \cdot \frac{1}{1 - j \frac{B(2N_0 + N)}{\omega_1 + \omega_2}}. \tag{A.29}
\end{aligned}$$

Comparing the linear and nonlinear frequency responses of Eqs. (A.15) and (A.29) with those of Eqs. (5.1) and (5.2) on page 93 shows that the introduction of a radiative recombination term caused by doping of the active region does not alter the frequency characteristics of $H_1(\omega_1)$ and $H_2(\omega_1, \omega_2)$. Both functions are still interconnected by a common cutoff frequency, which is now given by Eq. (A.16). In the absence of doping, the magnitude of H_2 scales with $1/N_{0,\text{no doping}}^2$. When doping is present, the magnitude of H_2 scales with

$$\frac{1}{(2N_{0,\text{doping}} + N)^2} = \frac{1}{\sqrt{(N/2)^2 + N_{0,\text{no doping}}^2}}. \tag{A.30}$$

That is, the analytic expression of H_2 predicts that the IM2 magnitude is lowered, compared to the undoped case. So, doping of the active region of the DH or QW device could, at least partly, be responsible for the observations of Fig. 3.15 on page 66, where it was found that the real devices suffer slightly lower magnitudes of the HD x than the simplified carrier density rate equation model predicts.

These trends are confirmed by numerical simulations of the two carrier density rate equation models, as shown in Figs. A.4 and A.5. The colors of the two results for H_2 shown in Fig. A.5 are scaled to the same magnitudes. It is seen that the presence of doping (right) slightly reduces the magnitudes; by roughly about 1.5 dB in the case of

$N = 5 \cdot 10^{17}/\text{cm}^3$. That is, the doping term tends to linearize the device. Further, the maxima (marked by circles) are shifted from $f_1 = f_2 = 9 \text{ MHz}$ to $f_1 = f_2 = 10.2 \text{ MHz}$, just as predicted by Eq. (A.17).

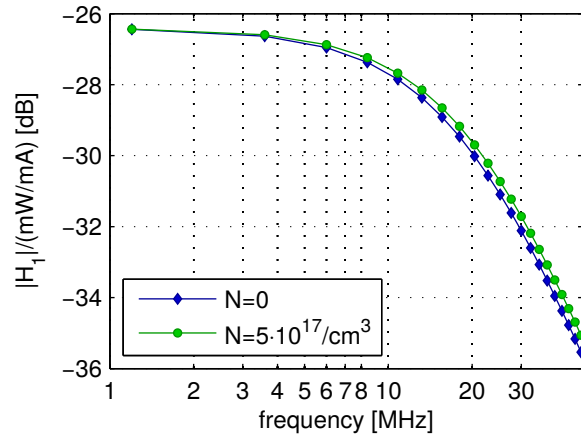


Figure A.4.: Frequency response with and without doping (numerical simulation).

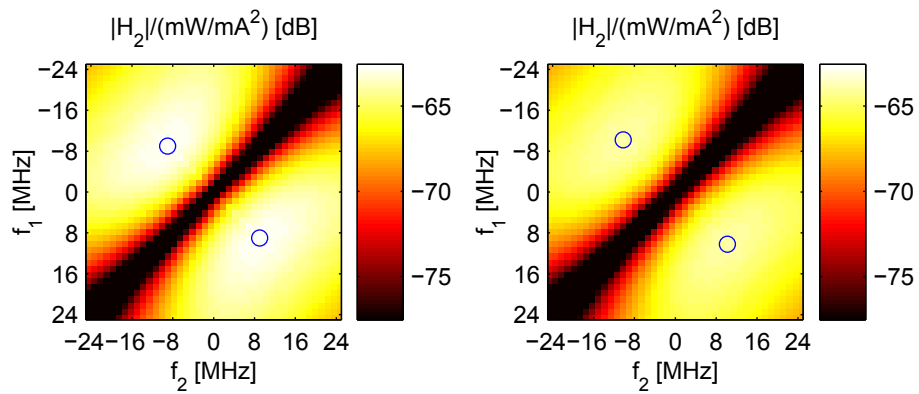


Figure A.5.: Frequency response of the IM2 without doping (left) and with doping (right) (numerical simulation).

B. Acronyms

ADC	Analog-to-Digital Converter
AlGaAs	Aluminium gallium arsenide
AlGaInP	Aluminium gallium indium phosphide
APD	Avalanche Photodiode
AWG	Arbitrary Waveform Generator
BER	Bit Error Ratio
DBR	Distributed Bragg Reflector
DFE	Decision Feedback Equalizer
DFT	Discrete Fourier Transform
DH	Double Heterostructure
DMT	Discrete Multitone
DOS	Density of States
DSO	Digital Sampling Oscilloscope
E/O	Electro-Optical
FFE	Feed-Forward Equalizer
FFT	Fast Fourier Transform
FIR	Finite Impulse Response
FSO	Free-Space Optical
FWHM	Full Width at Half Maximum
GaAs	Gallium-Arsenide
GaN	Gallium-Nitride
GaP	Gallium-Phosphide
Ge	Germanium
IM2	2 nd -order intermodulation product
InGaAs	Indium gallium arsenide
InGaAsP	Indium gallium arsenide phosphide
InP	Indium phosphide
IR	Infrared
LED	Light-Emitting Diode
LTI	Linear Time-Invariant
<i>M</i>²-CAP	Multilevel Carrierless Amplitude and Phase modulation
<i>M</i>-PAM	Multilevel Pulse Amplitude Modulation
MOST	Media Oriented Systems Transport
MQW	Multi Quantum Well
MSE	Mean Squared Error
ND	Neutral Density
OOK	On-Off Keying
OWC	Optical Wireless Communication
PAM	Pulse Amplitude Modulation
PD	Photo Detector
POF	Polymer Optical Fiber

B. Acronyms

PRBS	Pseudorandom Binary Sequence
QW	Quantum Well
RC-LED	Resonant-Cavity Light-Emitting Diode
RF	Radio Frequency
Rx	Receiver
SE	Spectral Efficiency
SH	Single Heterostructure
Si	Silicon
SI-POF	Step-Index Polymer Optical Fiber
SMF	Single-Mode Fiber
SNR	Signal-to-Noise Ratio
SRH	Shockley-Reed-Hall
TIA	Trans-Impedance Amplifier
TOSLINK	Toshiba-Link
VCSEL	Vertical-Cavity Surface-Emitting Laser
VLC	Visible Light Communication
WDM	Wavelength Division Multiplexing

C. Bibliography

- [1] Simon M. Sze. *Physics of Semiconductor Devices*. Wiley-Interscience, Hoboken, NJ, 3. ed. edition, 2007.
- [2] A. I. Onischenko, T. E. Sale, E. P. O'Reilly, A. R. Adams, S. M. Pinches, J. E. F. Frost, and J. Woodhead. Progress in the design and development of AlGaInP visible VCSELs. *IEE Proceedings - Optoelectronics*, 147(1):15–21, Feb 2000.
- [3] J. Vinogradov, R. Kruglov, K. Chi, J. Shi, M. Bloos, S. Loquai, and O. Ziemann. GaN Light-Emitting Diodes for up to 5.5-Gb/s Short-Reach Data Transmission Over SI-POF. *IEEE Photonics Technology Letters*, 26(24):2473–2475, Dec 2014.
- [4] J. . Shi, C. Lin, W. Chen, J. E. Bowers, J. . Sheu, C. Lin, Y. Li, J. Vinogradov, and O. Ziemann. Very high-speed GaN-based cyan light emitting diode on patterned sapphire substrate for 1 Gbps plastic optical fiber communication. In *OFC/NFOEC*, 2012.
- [5] J. Vucic, C. Kottke, S. Nerreter, K. Langer, and J. W. Walewski. 513 Mbit/s Visible Light Communications Link Based on DMT-Modulation of a White LED. *Journal of Lightwave Technology*, 28(24):3512–3518, Dec 2010.
- [6] A. Grzemba. *MOST: The Automotive Multimedia Network*. Electronics library. Franzis, 2011.
- [7] C.-A. Bunge, M. Beckers, and B. Lustermann. *Basic principles of optical fibres*, volume 89 of *Woodhead Publishing Series in Electronic and Optical Materials*, pages 47–118. Elsevier ; WP Woodhead Publishing, Amsterdam [u.a.], 2017.
- [8] S. Randel and C.-A. Bunge. Spectrally efficient polymer optical fiber transmission. In *SPIE Proceedings*, volume 7960, pages 1–9, 2011.
- [9] S.C.J. Lee, F. Breyer, S. Randel, O. Ziemann, H.P.A. van den Boom, and A.M.J. Koonen. Low-Cost and Robust 1-Gbit/s Plastic Optical Fiber Link Based on Light-Emitting Diode Technology. In *Optical Fiber Communication Conference/National Fiber Optic Engineers Conference*, page OWB3. Optical Society of America, 2008.
- [10] F. Breyer, S. C. J. Lee, D. Cardenas, S. Randel, and N. Hanik. Real-time Gigabit Ethernet Transmission over up to 25 m Step-Index Polymer Optical Fibre using LEDs and FPGA-Based Signal Processing. In *2009 35th European Conference on Optical Communication*, pages 1–2, Sep. 2009.
- [11] A. Nespola, S. Straullu, P. Savio, D. Zeolla, S. Abrate, D. Cárdenas, J. Ramirez, N. Campione, and R. Gaudino. First Demonstration of Real-Time LED-based Gigabit Ethernet Transmission on 50m of A4a.2 SI-POF with Significant System Margin. In *36th European Conference and Exhibition on Optical Communication*, pages 1–3, Sep. 2010.

C. Bibliography

- [12] M. Schüppert and C. A. Bunge. 5Gb/s Eye-Safe LED-Based SI-POF Transmission With Equalization of Transmitter Nonlinearities. *IEEE Photonics Technology Letters*, 28(23):2732–2735, Dec 2016.
- [13] J. Vučić, L. Fernández, C. Kottke, K. Habel, and K. . Langer. Implementation of a Real-Time DMT-based 100 mbit/s Visible-Light Link. In *36th European Conference and Exhibition on Optical Communication*, pages 1–5, Sep. 2010.
- [14] J. Vucic, C. Kottke, S. Nerreter, K. Langer, and J. W. Walewski. 513 Mbit/s Visible Light Communications Link Based on DMT-Modulation of a White LED. *Journal of Lightwave Technology*, 28(24):3512–3518, Dec 2010.
- [15] C. Kottke, K. Habel, L. Grobe, J. Hilt, L. F. del Rosal, A. Paraskevopoulos, and K. Langer. Single-Channel Wireless Transmission at 806 Mbit/s Using a White-Light LED and a PIN-based Receiver. In *2012 14th International Conference on Transparent Optical Networks (ICTON)*, pages 1–4, July 2012.
- [16] Fang-Ming Wu, Chun-Ting Lin, Chia-Chien Wei, Cheng-Wei Chen, Zhen-Yu Chen, and Hou-Tzu Huang. 3.22-Gb/s WDM Visible Light Communication of a Single RGB LED Employing Carrier-Less Amplitude and Phase Modulation. In *2013 Optical Fiber Communication Conference and Exposition and the National Fiber Optic Engineers Conference (OFC/NFOEC)*, pages 1–3, March 2013.
- [17] IEEE Standard for Local and metropolitan area networks—Part 15.7: Short-Range Optical Wireless Communications. *IEEE Std 802.15.7-2018 (Revision of IEEE Std 802.15.7-2011)*, pages 1–407, April 2019.
- [18] T. P. Lee. The Nonlinearity of Double-Heterostructure LED’s for Optical Communications. *Proceedings of the IEEE*, 65(9):1408–1410, Sep. 1977.
- [19] R. W. Dawson. Frequency and Bias Dependence of Video Distortion in Burrus-Type Homostructure and Heterostructure LED’s. *IEEE Transactions on Electron Devices*, 25(5):550–551, May 1978.
- [20] R. S. Tucker. Circuit model of double-heterojunction laser below threshold. *IEE Proceedings I - Solid-State and Electron Devices*, 128(3):101–106, June 1981.
- [21] A. Descombes and W. Guggenbuhl. Large Signal Circuit Model for LED’s Used in Optical Communication. *IEEE Transactions on Electron Devices*, 28(4):395–404, April 1981.
- [22] T. Kamalakis, J. W. Walewski, G. Ntogari, and G. Mileounis. Light-emitting diodes: The Unknown Entities. In *2010 12th International Conference on Transparent Optical Networks*, pages 1–9, June 2010.
- [23] T. Kamalakis, J. W. Walewski, G. Ntogari, and G. Mileounis. Empirical Volterra-Series Modeling of Commercial Light-Emitting Diodes. *Journal of Lightwave Technology*, 29(14):2146–2155, July 2011.
- [24] Haiyu Zhang, Peng Liu, Qianshuo Li, Jiang Liu, and Song Liu. LED Nonlinearity Impact on Frequency Modulation Signals over Visible Light Communication Systems. In *2015 IEEE International Conference on Communication Problem-Solving (ICCP)*, pages 369–372, Oct 2015.

- [25] B. Inan, S. C. Jeffrey Lee, S. Randel, I. Neokosmidis, A. M. J. Koonen, and J. W. Walewski. Impact of LED Nonlinearity on Discrete Multitone Modulation. *IEEE/OSA Journal of Optical Communications and Networking*, 1(5):439–451, Oct 2009.
- [26] I. Neokosmidis, T. Kamalakis, J. W. Walewski, B. Inan, and T. Spicopoulos. Impact of Nonlinear LED Transfer Function on Discrete Multitone Modulation: Analytical Approach. *Journal of Lightwave Technology*, 27(22):4970–4978, Nov 2009.
- [27] S. Zhao, S. Cai, K. Kang, and H. Qian. Optimal Transmission Power in a Non-linear VLC System. In *2015 IEEE Global Conference on Signal and Information Processing (GlobalSIP)*, pages 1180–1184, Dec 2015.
- [28] H. Qian, S. J. Yao, S. Z. Cai, and T. Zhou. Adaptive Postdistortion for Nonlinear LEDs in Visible Light Communications. *IEEE Photonics Journal*, 6(4):1–8, Aug 2014.
- [29] X. Li, H. Chen, S. Li, Q. Gao, C. Gong, and Z. Xu. Volterra-based Nonlinear Equalization for Nonlinearity Mitigation in Organic VLC. In *2017 13th International Wireless Communications and Mobile Computing Conference (IWCMC)*, pages 616–621, June 2017.
- [30] X. Deng, S. Mardanikorani, Y. Wu, K. Arulandu, B. Chen, A. M. Khalid, and J. M. G. Linnartz. Mitigating LED Nonlinearity to Enhance Visible Light Communications. *IEEE Transactions on Communications*, 66(11):5593–5607, 2018.
- [31] M. Schueppert and C. Bunge. LED Device Characterization with a Harmonic Balance Approach. In *Photonic Networks; 19th ITG-Symposium*, pages 1–7, June 2018.
- [32] M. Schüppert and C. Bunge. Characterization and Equalization of Nonlinearities in Directly Modulated Resonant Cavity Light-Emitting Diodes. In *2016 18th International Conference on Transparent Optical Networks (ICTON)*, pages 1–4, July 2016.
- [33] M. Grundmann. *The Physics of Semiconductors : An Introduction Including Nanophysics and Applications*. Graduate texts in physics. Springer, Cham ; Heidelberg, third edition edition, 2016.
- [34] E. F. Schubert. *Light-Emitting Diodes*. Cambridge University Press, 2006.
- [35] Paul Harrison. *Quantum Wells, Wires and Dots : Theoretical and Computational Physics of Semiconductor Nanostructures*. Fourth edition edition, 2016.
- [36] Shyh Wang. *Fundamentals of semiconductor theory and device physics*. Prentice Hall series in electrical and computer engineering. Prentice Hall, Englewood Cliffs, NJ, 1989.
- [37] Jean-Pierre Colinge and Cynthia A. Colinge. *Physics of semiconductor devices*. Kluwer Academic, Boston [u.a.], 2002.

C. Bibliography

- [38] Hideto Sugawara, Masayuki Ishikawa, Yoshihiro Kokubun, Yukie Nishikawa, Shigeya Naritsuka, Kazuhiko Itaya, Genichi Hatakoshi, and Mariko Suzuki. Semiconductor light emitting device, October 6 1992. US Patent 5,153,889.
- [39] S. J. Chang, L. W. Wu, Y. K. Su, C. H. Kuo, W. C. Lai, Y. P. Hsu, J. K. Sheu, J. F. Chen, and J. M. Tsai. Si and Zn Co-Doped InGa_N-Ga_N White Light-Emitting Diodes. *IEEE Transactions on Electron Devices*, 50(2):519–521, Feb 2003.
- [40] A. K. Dutta, A. Suzuki, K. Kurihara, F. Miyasaka, H. Hotta, and K. Sugita. High-Brightness, AlGaInP-Based, Visible Light-Emitting Diode for Efficient Coupling with POF. *IEEE Photonics Technology Letters*, 7(10):1134–1136, Oct 1995.
- [41] J. R. Chen, T. S. Ko, T. C. Lu, Y. A. Chang, H. C. Kuo, Y. K. Kuo, J. Y. Tsai, L. W. Laih, and S. C. Wang. Fabrication and Characterization of Temperature Insensitive 660-nm Resonant-Cavity LEDs. *Journal of Lightwave Technology*, 26(13):1891–1900, July 2008.
- [42] Michael J Kelly. *Low dimensional semiconductors : materials, physics, technology, devices*. Oxford science publications. 1995.
- [43] N. E. J. Hunt, E. F. Schubert, D. L. Sivco, A. Y. Cho, and G. J. Zydzik. Power and efficiency limits in single-mirror light emitting diodes with enhanced intensity. *Electronics Letters*, 28(23):2169–2171, Nov 1992.
- [44] W. Grieshaber, E. F. Schubert, I. D. Goepfert, R. F. Karlicek, M. J. Schurman, and C. Tran. Competition between band gap and yellow luminescence in Ga_N and its relevance for optoelectronic devices. *Journal of Applied Physics*, 80(8):4615–4620, 1996.
- [45] G. Winstel; C. Weyrich. *Optoelektronik. 1, Lumineszenz- und Laserdioden*. Springer, 1980.
- [46] Edgar Voges. *Optische Kommunikationstechnik : Handbuch für Wissenschaft und Industrie*. Engineering online library. Springer, Berlin u.a., 2002.
- [47] R. Olshansky, C. Su, J. Manning, and W. Powazinik. Measurement of Radiative and Nonradiative Recombination Rates in InGaAsP and AlGaAs Light Sources. *IEEE Journal of Quantum Electronics*, 20(8):838–854, Aug 1984.
- [48] C. B. Su, J. Schlafer, J. Manning, and R. Olshansky. Measurement of radiative recombination coefficient and carrier leakage in 1.3 μ m InGaAsP lasers with lightly doped active layers. *Electronics Letters*, 18(25):1108–1110, December 1982.
- [49] C. S. Xia, Z. M. Simon Li, Y. Sheng, L. W. Cheng, W. Da Hu, and W. Lu. Simulation of InGa_N/Ga_N light-emitting diodes with a non-local quantum well transport model. In *2012 12th International Conference on Numerical Simulation of Optoelectronic Devices (NUSOD)*, pages 21–22, Aug 2012.
- [50] S. Birner, T. Zibold, T. Andlauer, T. Kubis, M. Sabathil, A. Trellakis, and P. Vogl. nextnano: General Purpose 3-D Simulations. *IEEE Transactions on Electron Devices*, 54(9):2137–2142, Sep. 2007.

- [51] Hiroyuki Matsusue, Toshio; Sakaki. Radiative recombination coefficient of free carriers in GaAs-AlGaAs quantum wells and its dependence on temperature. *Applied Physics Letters*, 50(20):1429–1431, 1987.
- [52] R. N. Hall. Recombination processes in semiconductors. *Proceedings of the IEE - Part B: Electronic and Communication Engineering*, 106(17):923–931, May 1959.
- [53] F. Stern. Calculated spectral dependence of gain in excited GaAs. *Journal of Applied Physics*, 47(12):5382–5386, 1976.
- [54] G. P. Agrawal and N. K. Dutta. *Semiconductor lasers*. 2. ed. edition, 1993.
- [55] D. W. Snoke, W. W. Rühle, Y.-C. Lu, and E. Bauser. Evolution of a nonthermal electron energy distribution in GaAs. *Phys. Rev. B*, 45:10979–10989, May 1992.
- [56] Qifeng Shan, Qi Dai, Sameer Chhajed, Jaehee Cho, and E. Fred Schubert. Analysis of thermal properties of GaInN light-emitting diodes and laser diodes. *Journal of Applied Physics*, 108(8):–, 2010.
- [57] Gilbert Held. *Introduction to Light Emitting Diode Technology and Applications*. An Auerbach book. 2009.
- [58] C. Yen, Y. Liu, T. Chen, L. Chen, T. Tsai, and W. Liu. Study of an AlGaInP-Based Light-Emitting Diode With a Modulation-Doped Multiquantum-Well (MD-MQW) Structure. *IEEE Photonics Technology Letters*, 21(10):609–611, May 2009.
- [59] C. Huh, W. J. Schaff, L. F. Eastman, and Seong-Ju Park. Temperature Dependence of Performance of InGaN/GaN MQW LEDs With Different Indium Compositions. *IEEE Electron Device Letters*, 25(2):61–63, Feb 2004.
- [60] E. Hairer and G. Wanner S.P. Hø rstett. *Solving Ordinary Differential Equations. 1, Nonstiff Problems*. Springer, 2. rev. ed., 2., corr. printing edition, 2000.
- [61] W.H. Press, S.A. Teukolsky, W.T. Vetterling, and B.P. Flannery. *Numerical Recipes : The Art of Scientific Computing*. Cambridge University Press, 3 edition, 2007.
- [62] HAMAMATSU PHOTONICS K.K., Solid State Devison. *Red LED for optical link: L8045 Emitter for 50 Mbps optical link*, 10 2017.
- [63] Avago Technologies. *SFH757 and SFH757V Transmitter for Polymer Optical Fiber Applications Data Sheet*, 12 2011.
- [64] Martin. Schetzen. *The Volterra and Wiener theories of nonlinear systems*. Wiley New York, 1980.
- [65] W. C. Rideout, J. LaCourse, and R. B. Lauer. Radiative and Non-Radiative Recombination Mechanisms in 1.5 μ m MQW Lasers. In *12th IEEE International Conference on Semiconductor Laser*, pages 86–87, Sep. 1990.
- [66] Oliver Nelles. *Nonlinear System Identification : From Classical Approaches to Neural Networks and Fuzzy Models*. Engineering online library. 2001.

C. Bibliography

- [67] S. Egami. Nonlinear, Linear Analysis and Computer-Aided Design of Resistive Mixers. *IEEE Transactions on Microwave Theory and Techniques*, 22(3):270–275, Mar 1974.
- [68] B. Schüppert. Modified numerical method for solving the nonlinear mixer pumping problem. *Electronics Letters*, 19(2):50–52, January 1983.
- [69] S. Iezekiel, C. M. Snowden, and M. J. Howes. Harmonic balance model of laser diode. *Electronics Letters*, 25(8):529–530, April 1989.
- [70] M. Schetzen. Theory of p th-Order Inverses of Nonlinear Systems. *IEEE Transactions on Circuits and Systems*, 23(5):285–291, May 1976.
- [71] A. Amari, O. A. Dobre, and R. Venkatesan. Fifth-Order Volterra-Based Equalizer for Fiber Nonlinearity Compensation in Nyquist WDM Superchannel System. In *2017 19th International Conference on Transparent Optical Networks (ICTON)*, pages 1–4, July 2017.